PRECIPITATION BEHAVIOR AND MECHANICAL PROPERTIES OF INTERMETALLIC-STRENGTHENED HIGH-ENTROPY ALLOYS

GUO JIAMING

PhD

The Hong Kong Polytechnic University

2025

The Hong Kong Polytechnic University

Department of Mechanical Engineering

Precipitation Behavior and Mechanical Properties of Intermetallic-Strengthened High-Entropy Alloys

Guo Jiaming

A thesis submitted in partial fulfilment of the requirements for the degree of Doctor of Philosophy

Aug 2025

Certificate of Originality

I hereby declare that this thesis is my own work and that, to the best of my knowledge and belief, it reproduces no material previously published or written, nor material that has been accepted for the award of any other degree or diploma, except where due acknowledgement has been made in the text.

_____ (Signed)

____GUO Jiaming___ (Name of student)

Abstract

High-entropy alloys (HEAs) have attracted extensive attention due to their vast composition space and unique mechanical properties, offering new opportunities for the development of advanced structural materials. Among various HEAs, face-centered cubic (FCC) HEAs have spanned a wide range of scientific interest due to their excellent toughness and ductility at both ambient and cryogenic temperatures. However, a single-phase FCC structure generally results in a low yield strength, which is insufficient for many practical applications. Precipitation strengthening has proved to be one of the most effective methods for improving the strength of FCC HEAs. Especially, introducing a coherent $L1_2$-ordered phase by incorporating Al and Ti into FCC HEAs has been demonstrated to enhance strength without significantly compromising ductility. Some other hard precipitates, such as Laves and σ precipitates, are strong barriers for dislocation motion, which can provide a high work hardening rate in the early stages of deformation, having the potential to avoid the formation of Luders bands. In view of the advantages and limitations of sheared and bypassed precipitates, it is interesting to design advanced HEAs with multiple types of precipitates. It is hoped to maximize the advantages of the different types of precipitates while minimizing their disadvantages, thereby achieving superior mechanical properties. However, precipitation in multicomponent HEAs is extremely complicated, which involves complex elemental partitioning and solute interactions. There was a lack of in-depth understanding on the precipitation and mechanical behaviors of HEAs. The purpose of this thesis is to quantitatively understand the precipitation behavior of HEAs and correlate their precipitate microstructure with bulk mechanical properties.

First, the study explores the introduction of additional hard phases into continuous precipitation (CP) $L1_2$-strengthened HEAs to achieve dual precipitation, thereby further improving the strength-ductility trade-off of FCC-HEAs. Through the combined introduction of coherent $L1_2$ nanoparticles and incoherent Laves phases, dual precipitation allows the alloys to attain a yield strength exceeding 1400 MPa, an ultimate tensile strength above 1800 MPa, and a uniform elongation of 18%. This results in a remarkable balance between strength and ductility. This approach combines the advantages of shearing and bypass strengthening mechanisms, providing a significant enhancement in mechanical performance compared to single-precipitate systems. The research not only demonstrates the effectiveness of dual precipitation in overcoming the traditional strength-ductility challenge, but also offers a promising design strategy for developing high-performance structural materials with balanced and superior mechanical properties.

Second, discontinuous precipitation (DP) has emerged as an effective strategy for designing alloys that combine high strength and excellent ductility, highlighting the importance of understanding how microstructural changes influence mechanical properties. In this study, we systematically investigated the precipitate evolution, recrystallization, and mechanical properties of a DP strengthened high-entropy alloy (HEA) under various aging conditions from 500 to 800 °C. The results indicate that at low aging temperatures, limited atomic mobility results in sluggish recrystallization, causing DP to preferentially initiate and propagate along grain boundaries, ultimately forming a fine nanorod microstructure. As the aging temperature increases, the kinetics of both recrystallization and DP are accelerated, resulting in the rapid formation of nanorod precipitates and the development of fully recrystallized ultrafine-grained structures. Mechanical tests demonstrate that by optimizing the grain structure and

precipitate microstructure, an optimal combination of a yield strength exceeding 2000 MPa and a total elongation of approximately 18% can be achieved. Quantitative analysis reveals that precipitation strengthening and grain boundary strengthening are the primary factors contributing to the enhanced yield strength. These findings deepen our understanding of the structure–property relationships in DP-strengthened alloys and provide practical guidance for designing advanced alloys with tailored mechanical properties through controlled microstructural evolution.

In addition, inspired by the experience of dual precipitation strengthening in CP systems, this research introduced σ phases into DP nanorods strengthened HEAs to further improve the strength–ductility balance. Microstructural analyses reveal that this alloy forms a hierarchical structure composed of FCC/$L1_2$ architectures and ultrafine spherical σ phases after aging at 600 °C. The introduction of the σ phase not only further enhances the yield strength (2080 MPa) and ultimate tensile strength (2300 MPa), but also improves the work hardening capability, enabling excellent strength–ductility synergy with a total elongation of about 17%. Furthermore, strengthening mechanism analysis indicates that the FCC/$L1_2$ nanorod structure and ultrafine grains are the primary contributors, while the σ phase provides additional work hardening and strength enhancement.

In summary, this thesis elucidates the precipitation behavior and mechanical properties of $L1_2$-strengthened HEAs, demonstrating that synergistic strengthening mechanisms can achieve an outstanding balance of ultrahigh strength and good ductility. It provides comprehensive insight into the microstructural evolution of DP-HEAs, revealing the critical role of grain structure and precipitate morphology in tailoring mechanical properties. These findings not only deepen the understanding of the structure–property relationships in coherent nano-$L1_2$ strengthened HEAs, but also

offer practical guidance for designing advanced structural materials with excellent mechanical performance through controlled microstructural evolution.

Publications arising from my PhD research

Journal papers

[1] **J.M. Guo**, B.C. Zhou, S. Qiu, H.J. Kong, M.C. Niu, J.H. Luan, T.L. Zhang, H. Wu, Z.B. Jiao*, Achieving ultrahigh strength and ductility in high-entropy alloys via dual precipitation, ***Journal of Materials Science & Technology*** 166 (2023) 67-77. (DOI: 10.1016/j.jmst.2023.05.021, IF: 14.3).

[2] **J.M. Guo**, B.Y. Ni, Z.B. Jiao*, Research progress on nanoprecipitation-strengthened high-entropy alloys, ***Materials China*** (2025) 44, 31. (DOI: 10.7502/j.issn.1674-3962.202410004).

[3] **J.M. Guo**, J.Y.C. Fang, Y.B. Ke, Z.B. Jiao*, Precipitate evolution, recrystallization, and mechanical properties of an ultrastrong HEA strengthened by $L1_2$ discontinuous precipitates, under review in ***Journal of Alloys and Compounds***.

[4] **J.M. Guo**, Z.B. Jiao*, et al., Synergistic precipitation strengthening via $L1_2$ nanorods and σ nanoparticles in ultrahigh-strength alloys with high work hardening, ***in preparation***.

[5] M.C Niu, S. Qiu, Q. Yu, W. Li, S. Zhang, **J.M Guo**, J.H Luan, W. Wang, T. Yang, X.L Wang, Z.B. Jiao*, Achieving excellent elevated-temperature mechanical properties in dual-phase high-entropy alloys via nanoscale co-precipitation and heterostructure engineering, ***Acta Materialia*** 284 (2025) 120634. (DOI: 10.1016/j.actamat.2024.120634).

[6] B.C. Zhou, S. F. Liu, H. Wu, J.H. Luan, **J.M. Guo**, T. Yang, Z.B. Jiao*, Nanoscale precipitation, mechanical properties, and deformation behavior of NiAl-strengthened high-strength steels: Effects of Ni and Al contents and ratios. ***Materials & Design***, (2023) *234*, 112341. (DOI: 10.1016/j.matdes.2023.112341).

[7] Z. Tian, W. Chen, H. Wang, C. Chu, J. Liu, L. Hao, W. Xiong, **J.M. Guo**, Z.B. Jiao, Z. Fu*, Microstructural evolution, mechanical behavior, and deformation mechanisms of a lightweight Ti–Nb–Cr–V refractory high-entropy alloy at room and elevated temperatures, ***Materials Science and Engineering: A*** 910 (2024) 146883. (DOI: 10.1016/j.msea.2024.146883).

[8] W.T. Zhang, X.Q. Wang, F.Q. Zhang, X.Y. Cui, B.B. Fan, **J.M. Guo**, Z.B. Jiao*, *et al.* , Frontiers in high entropy alloys and high entropy functional materials, ***Rare Metals*** 43(10) (2024) 4639-4776. (DOI: 10.1007/s12598-024-02852-0).

Conference presentation

[1] **J.M Guo,** Z.B. Jiao, Precipitation mechanisms and mechanical properties of new high-entropy alloys strengthened by dual precipitation, Materials Science and Engineering MSE Congress, 2022.

[2] **J.M Guo,** Z.B. Jiao, Achieving ultrahigh strength and ductility in high-entropy alloys via dual precipitation, Chinese Materials Conference, Shenzhen China, 2023.

[3] **J.M Guo,** Z.B. Jiao, Achieving ultrahigh strength and ductility in high-entropy alloys via dual precipitation, The 2nd PolyU Research Student Conference (PRSC), PolyU, Hong Kong, 2024.

Award

[1] **Champion**, The 7th Mechanical Engineering Presentation Competition, PolyU, 2021.

[2] **Excellent academic presentation**, Chinese Materials Conference 2023, Shenzhen China, 2023.

[3] **Best paper runner-up**, The 2nd PolyU Research Student Conference (PRSC), PolyU, Hong Kong, 2024.

Acknowledgements

Since 2019, when I first arrived at The Hong Kong Polytechnic University to pursue my master's degree, to now, as I am about to complete my PhD in 2025, these 6 years have been a period of tremendous learning and personal growth.

First and foremost, I would like to express my deepest gratitude to my supervisor, Prof. Zengbao Jiao. When I was still unfamiliar with the field of metallurgy, he gave me the invaluable opportunity to join the Advanced Structural Materials group as a master student, opening the door to the world of academic research. Later, when I was uncertain about my future, he once again believed in me and offered me the chance to continue my journey as a PhD student, which was an immense affirmation for me. Throughout my studies, he has shared his experience and knowledge without reservation, always generously imparting his optimistic outlook on life and his rigorous scientific attitude, constantly encouraging me to move forward. Thank you once again for all your support, and I will continue to strive harder.

I would also like to sincerely thank Dr. Junhua Luan from CityU for his help with thermodynamic calculations and APT analysis. My heartfelt thanks go out to all the members of Prof. Jiao's research group, including Dr. Bingchen Zhou, Dr. Mengchao Niu, Dr. Jieyichen Fang, Dr. Shi Qiu, Dr. Bohan Chen, Mr. Bingyu Ni, Mr. Qiang Yu, Mr. Tongzhen Zhang, Mr. Pengyu Xu, Ms. Wenzhe Li, and Mr. Zheng Qu, for their tremendous support in experiments and for every spark of inspiration in our discussions.

It is also very important for me to thank my friends, especially the members of the Gentle Villain band: Dr. Yi Zhong, Mr. Deyou Li, Mr. Chuang Yi, Mr. Tian You, Mr. Weiran Chen, and Mr. Pengfei Wen. I will always cherish the days we rocked together, and I hope we will keep writing great songs and never forget the spirit of rock and roll.

My gratitude also extends to my friends in the “King of Crab Burger” guild of World of Warcraft: Mr. Jiacheng Jing, Mr. Shaolei Li, Mr. Guangxin Lu, Mr. Shengdazhi Chen, Mr. Peiliang Lu, Mr. Hao Zhang, Mr. Dong Zhao, Mr. GuaGua, Mr. Yuzhou Zhang, Mr. Yuanhao Liu, Mr. BeiBei, Mr. Yichao Xie, and Mr. Banana, for the memories we created adventuring in Azeroth, bringing relaxation and joy to my otherwise intense academic life. And to best friend in my life, my girlfriend, Ms. Jo—thank you for your selfless love and devotion. You have always been there to encourage and support me, meeting my every mood with patience and care. I have learned so much from you, and I look forward to a beautiful future together.

Most importantly, I owe everything to my family: my parents, Mr. Zhiwei Guo and Ms. Lixia Guo, my grandparents, Mr. Wairen Guo and Ms. Suxia Guo, and my maternal grandparents, Mr. Yiwen Guo and Ms. Xinping Qin. Thank you for your endless love and support throughout my life. Your encouragement is my greatest motivation, and home will always be my safe harbor. Without you, I would not be who I am today.

Finally, I want to thank myself, Mr. Guo Jiaming. Thank you for persevering—may everything go smoothly for you.

Table of Contents

Abstract I

Publications arising from my PhD research..... V

Acknowledgements..... VII

Table of contents.....IX

List of figures..... XII

List of tables..... XVIII

Chapter 1 Introduction.....1

1.1 Research background and motivation.....1

1.2 Research Objectives.....4

1.3 Organization of this thesis 5

Chapter 2 Literature review.....6

2.1 Introduction to M/HEAs 6

2.2 Unique features 8

2.3 Precipitate strengthened M/HEAs.....13

2.3.1. Background of the precipitation-strengthened M/HEAs 13

2.3.2. Incoherent precipitation strengthened M/HEAs 16

2.3.3. Coherent precipitation strengthened M/HEAs.....18

2.3.4. Composite precipitation-strengthened HEAs 21

2.4 Precipitation modes of $L1_2$ precipitates 24

2.5 Summary.....26

Chapter 3 Methodology.....27

3.1 Material preparation.....27

3.2 Microstructure and nanostructure characterization 29
3.3 Mechanical properties testing 31
3.4 Thermodynamic calculations 32
Chapter 4 Achieving ultrahigh strength and ductility in HEAs via dual precipitation 33
4.1 Introduction 33
4.2 Thermodynamics-aided alloy design 36
4.3 Results 37
4.3.1. Mechanical properties 37
4.3.2. Microstructure 43
4.3.3. Nanoscale precipitation 46
4.3.4. First-principles calculation 48
4.4 Discussion 50
4.4.1. Strengthening mechanism 50
4.4.2. Deformation mechanism 54
4.5 Conclusions 59
Chapter 5 Precipitate evolution, recrystallization, and mechanical properties of an ultrastrong HEA strengthened by $L1_2$ discontinuous precipitates 62
5.1 Introduction 62
5.2 Results 64
5.2.1. Microstructure 64
5.2.2. SANS measurements 77
5.2.3. Mechanical properties 80
5.3 Discussion 83
5.3.1. Mechanisms of microstructural evolution 83
5.3.2. Kinetics of DP coarsening and recrystallization 85

5.3.3. Strengthening mechanism 90
5.4 Conclusions 94
Chapter 6 Synergistic precipitation strengthening via $L1_2$ nanorods and σ nanoparticles in ultrahigh-strength alloys with high work hardening 96
6.1 Introduction 96
6.2 Results 99
6.2.1. Thermodynamic calculation 99
6.2.2. Mechanical properties 100
6.2.3. Micro/nano-structural Characterization 103
6.3 Discussion 108
6.3.1. Formation of synergistic precipitation 108
6.3.2. Strengthening mechanisms 110
6.4 Conclusions 114
Chapter 7 Conclusions and future work 116
7.1 Conclusions 116
7.2 Suggestions for future work 117
References 119

List of figures

Fig. 2.1. A schematic diagram illustrating HEAs: the relationship between the number of principal elements and the corresponding number of equiatomic compositions [38]. 7

Fig. 2.2. The change curve of configuration entropy (mixing entropy) in a disordered equal atomic ratio alloy with the increase in the number of alloying elements [4]. 7

Fig. 2.3. Phase diagram illustrating the $Al_xCoCrCuFeNi$ system across different levels of aluminum content [44].....9

Fig. 2. 4. (a) Crystal lattice with identical atoms; (b) lattice distortion resulting from a solid solution of differently sized atoms, which are statistically distributed at random throughout the crystal structure [45]. 10

Fig. 2.5. (a) The composition distribution of the diffusion couple at the interface of the FeCoNiCrMn HEAs system (in the Cr-Mn couple), and (b) temperature dependence of the diffusion coefficients of Cr, Mn, Fe, Co, and Ni in various matrices [49]. 11

Fig. 2.6. Lattice constants of $Al_xCoCrCuFeNi$ alloy system with different Al contents, □ FCC phase and ● BCC phase [44]. 12

Fig. 2.7. Every possible subset—including quaternary, ternary, binary, and pure elements—of the quinary FeNiCoCrMn HEAs. Upon completion of casting and homogenization, single-phase FCC HEAs are denoted in red, in contrast to multi-phase or differently structured alloys, which are marked in black [53]. 13

Fig. 2.8. (a) Mechanical properties of the FeNiCoCrMn HEA measured at 293 K, 200 K, and 77 K; (b) the alloy's superior damage tolerance, reflected in its combination of strength and toughness, exceeds that of most pure metals and alloys [3].....14

Fig. 2.9. (a) Compressive engineering stress–strain curves of $FeCoCrNiNb_x$ alloys at room temperature; (b) Compressive engineering stress–strain curves of $FeCoNiCrMo_x$ alloys at room temperature [16, 61]. 17

Fig. 2.10. (a) Room temperature tensile properties of the alloys: CoCrFeNi (A), $(CoCrFeNi)_{94}Ti_2Al_4$ (B), $(CoCrFeNi)_{94}Ti_2Al_4$ processed by 30% rolling, followed by annealing at 1273 K for 2 hours and aging at 1073 K for 18 hours (P1), and $(CoCrFeNi)_{94}Ti_2Al_4$ processed by 70% rolling and subsequent aging at 923 K for 4 hours (P2). (b) and (c) display the microstructures of P1 and P2, respectively. [65]. . 19

Fig. 2.11. Tensile properties and deformation microstructure of the $(FeCoNi)_{86}Al_7Ti_7$ alloy: (a) engineering stress–strain curves, and (b) dynamic evolution of deformation substructures [19]. 20

Fig. 2.12. Schematic diagram depicting the precipitation mechanisms of $L1_2$ and BCC nanoprecipitates in the FCC and $L2_1$ phases of a eutectic HEA [68]. 22

Fig. 2.13. Schematic diagram depicting the microstructural evolution of $L1_2$-strengthened HEAs [71]. 25

Figure 2.14 Mechanical performance and microstructural features of the coherent nano-lamellar alloy: (a) Engineering stress–strain responses; (b) Interfacial coherency and elemental distribution within FCC/$L1_2$ nano-lamellae [21]. 25

Fig. 4.1. Calculated phase diagram of the $(Ni_2Co_2FeCr)_{96-x}Al_4Nb_x$ system. 37

Fig. 4.2. Vickers microhardness of the 3Nb, 5Nb, and 7Nb alloys as a function of aging time at 700 ℃. 38

Fig. 4.3. Tensile engineering stress–strain curves of the 3Nb, 5Nb, and 7Nb alloys after aging for 24 h at 700 ℃. 39

Fig. 4.4. Work hardening rate and true stress–strain curves of the 3–7Nb alloys. 40

Fig. 4.5. Fracture surfaces of the (a) 3Nb, (b) 5Nb, and (c) 7Nb alloys. 41

Fig. 4.6. Yield strength vs total elongation of the 5Nb alloy compared with various types of precipitation-strengthened HEAs. 42

Fig. 4.7. SEM microstructures of the (a) 3Nb, (b) 5Nb, and (c) 7Nb alloys after aging for 24 h at 700 ℃. 43

Fig. 4.8. Microstructures of the 5Nb alloy after aging for 24 h at 700 ℃: (a) Dark-field TEM image and SAED pattern, (b) XRD patterns, (c) EDS spectrum for the region with the bright contrast in the inset, and (d) and (e) are EBSD IPF and phase maps, respectively. The inset of (b) is the deconvolution of the (311) diffraction peak. 45

Fig. 4.9. APT characterization of the 5Nb alloy after aging for 24 h at 700 ℃: (a) atom maps and (b) proximity histogram concentration profiles. The inset of (b) is the calculation of the volume fraction of the $L1_2$ phase using the lever rule. 47

Fig. 4.10. First-principles calculations: (a) supercell models, (b) calculated formation energies, and (c) ELF maps of the structures with Nb in the FCC and $L1_2$ lattices. ... 49

Fig. 4.11. Calculated contributions of solid solution strengthening ($\Delta\sigma_s$), grain boundary strengthening ($\Delta\sigma_g$), precipitation strengthening ($\Delta\sigma_p$) from the $L1_2$ and Laves precipitates, and total yield strength (σ_{Total}) of the 5Nb HEA in the 24-h aged condition. The red dot represents the experimental yield strength of the alloy. 54

Fig. 4.12. Deformation microstructures of the 5Nb alloy: TEM images at the (a) 10% and (b) 20% tensile strains, (c) HRTEM image showing SFs in two directions and LC locks, (d) corresponding FFT image showing the intersecting SFs, (e) an enlarged view of a representative SF, (f) HR-TEM image showing the shearing of $L1_2$ precipitates by an SF and corresponding FFT patterns, and (g) TEM image showing the interaction of dislocations with Laves precipitates. 58

Fig. 4.13. (a) TEM image (enlarged view of Fig. 9(b)) and (b) HRTEM image (a clean version of Fig. 9(c)) of the 5Nb alloy at the 20% strain condition. 59

Fig. 5.1. SEM images of the alloy under different heat-treatment conditions: (a–d) 500 °C aged for 0.5, 2, 8, and 32 h, respectively; (e–h) 600 °C aged for 0.5, 2, 8, and 32 h, respectively; (i–l) 700 °C aged for 0.5, 2, 8, and 32 h, respectively; (m–p) 800 °C aged for 0.5, 2, 8, and 32 h, respectively. 67

Fig. 5.2. High-magnification SEM images of the alloy under different heat-treatment conditions: (a–d) 500 °C aged for 0.5, 2, 8, and 32 h, respectively; (e–h) 600 °C aged for 0.5, 2, 8, and 32 h, respectively; (i–l) 700 °C aged for 0.5, 2, 8, and 32 h, respectively; (m–p) 800 °C aged for 0.5, 2, 8, and 32 h, respectively. 69

Fig. 5.3. EBSD IPF maps of the alloy under different heat-treatment conditions: (a–d) 500 °C aged for 0.5, 2, 8, and 32 h, respectively; (e–h) 600 °C aged for 0.5, 2, 8, and 32 h, respectively; (i–l) 700 °C aged for 0.5, 2, 8, and 32 h, respectively; (m–p) 800 °C aged for 0.5, 2, 8, and 32 h, respectively. 71

Fig. 5.4. EBSD GOS maps of the alloy under different heat-treatment conditions: (a–d) 500 °C aged for 0.5, 2, 8, and 32 h, respectively; (e–h) 600 °C aged for 0.5, 2, 8, and 32 h, respectively; (i–l) 700 °C aged for 0.5, 2, 8, and 32 h, respectively; (m–p) 800 °C aged for 0.5, 2, 8, and 32 h, respectively. 74

Fig. 5.5. (a) Area fractions of recrystallized regions and (b) grain sizes within these regions of the alloy under different heat-treatment conditions. 75

Fig. 5.6. SANS profiles and corresponding fitting curves of the samples aged at 600 °C for 0.5, 2, 8, and 32 h. The inset displays the evolution of the precipitate size distribution. 79

Fig. 5.7. Tensile engineering stress–strain curves of the $(CoCr_{0.5}FeNi_{1.5})_{87.5}Al_{7.5}Ti_5$ at different aging conditions: (a) aged at 600 °C for virous times, and (b) aged for 8 h at different temperatures. 81

Fig. 5.8. The yield strength versus total elongation of the coherent nano-rod $L1_2$ HEAs in comparison with various types of precipitation-strengthened HEAs. 83

Fig. 5.10. Recrystallization kinetics of the alloy under different heat-treatment conditions: (a) JMAK plot; (b) Recrystallized fraction versus aging time plot; (c) Arrhenius plot for determining the recrystallization activation energy (Q_r). 89

Fig. 5.11. GND density distribution maps of the samples aged at 600 °C for (a) 0.5 h, (b) 2 h, (c) 8 h, and (d) 32 h.....91

Fig. 5.12. Comparison of the contributions from grain boundary strengthening ($\Delta\sigma_g$), dislocation strengthening ($\Delta\sigma_d$), and precipitation strengthening ($\Delta\sigma_p$) to the yield strength under various aging conditions at 600 °C, along with the corresponding experimental yield strength values (σ_e).....93

Fig. 6.1. The mole fraction of equilibrium phases as a function of temperature of 0.75Cr alloy.....100

Fig. 6.2. Vickers microhardness of the 0.75Cr alloy as a function of aging time at 600°C. 101

Fig. 6.3. Tensile engineering stress–strain curves of the 0.75Cr and TPA alloy aged at 600 °C for 24 h.....102

Fig. 6.4. SEM images of the 0.75Cr alloy aged at 600 °C for 24h: (a) Low-magnification overview of the microstructure; (b) High-magnification image showing a region with dense precipitates; (c) High-magnification image showing the elliptical-shaped precipitate clusters. 104

Fig. 6.5. (a) XRD patterns of the 0.75Cr alloy aged at 600 °C for 24h; (b) the deconvolution of the (311) diffraction.....105

Fig. 6.6. 3D-APT characterization of the 0.75Cr alloy aged at 600 °C for 24 h: (a, c) The enlarged view of elliptical-shaped clusters and atom maps, respectively; (b, d) Proximity histograms of the $L1_2$ and σ phases, respectively. 106

Fig. 6.7. Schematics of the microstructures: (a) TPA alloy; (b) 0.75Cr alloy. 110

Fig. 6.8. Calculated contributions of solid solution strengthening ($\Delta\sigma_s$), dislocation strengthening ($\Delta\sigma_d$), grain boundary strengthening ($\Delta\sigma_g$), precipitation strengthening ($\Delta\sigma_p$), and total yield strength (σ_{Total}) of the 0.75Cr alloy aged at 600 °C for 24 h. The red dot represents the experimental yield strength. 113

List of tables

Table 3.1. Chemical compositions of the $(Ni_2Co_2FeCr)_{96-x}Al_4Nb_x$ (x = 3, 5, and 7), $(CoCr_{0.5}FeNi_{1.5})_{87.5}Al_{7.5}Ti_5$,and $(Ni_{1.75}FeCoCr_{0.75})_{86}Al_{10}Ti_4$ (at.%) alloys.....28

Table 3.2. Heat-treatments of $(CoCr_{0.5}FeNi_{1.5})_{87.5}Al_{7.5}Ti_5$ alloy.....29

Table 4.1. Yield strength (YS), ultimate tensile strength (UTS), total elongation (TE), and uniform elongation (UE) of the alloys after aging for 24 h at 700 ℃. 40

Table 4.2. Matrix and precipitate compositions of the 5Nb HEA in the 24-aged condition determined by APT (at.%).....48

Table 5.1. Average radii (*r*), lengths (*l*), and volume fractions (*f*) of the nano precipitates in the samples under different aging times at 600 °C.....79

Table 5.2. Yield strengths (YS), ultimate tensile strengths (UTS), elongations-to-failure (EF), and uniform elongations (UE) of the samples under different heat-treatment conditions.....82

Table 6.1. Yield strengths (YS), ultimate tensile strengths (UTS), elongations-to-failure (EF), and uniform elongations (UE) of the 0.75 Cr and TPA alloys aged at 600 °C for 24 h.....103

Table 6.2. Matrix and precipitates compositions (at.%) of the 0.75 Cr alloy aged at 600 °C for 24 h.....107

Chapter 1 Introduction

1.1 Research background and motivation

The continuous innovation of advanced structural materials is crucial to promoting technological progress and sustainable development of society, and a wide variety of industrial applications require materials with high strength and ductility. However, improving strength of materials usually results in a decrease in ductility, which is known as the strength-ductility trade-off [1, 2]. Recently, the design concept of medium/high-entropy alloys (M/HEAs) has attracted growing interest due to their distinctive microstructures. These unique features offer new possibilities for achieving outstanding mechanical properties [3-7]. Contrary to conventional physical metallurgy principles, which predict the formation of numerous intermetallic compounds, these compositionally complex alloys are often able to form microstructurally simple solid solutions—such as FCC, body-centered cubic (BCC), or hexagonal close-packed (HCP) structures. This is primarily attributed to their high mixing entropy, which enhances the stability of these phases [8]. FCC HEAs have attracted significant scientific attention because they exhibit outstanding toughness and ductility at both room temperature and cryogenic conditions [3, 4, 9-12]. However, a single-phase FCC structure generally results in a low yield strength, which is insufficient for many practical applications. As such, extensive efforts have been devoted to improving the strength of FCC HEAs through various strengthening methods, including solid solution strengthening, grain size refinement, strain hardening, and precipitation strengthening [13-15].

Among these strengthening strategies, precipitation strengthening is widely used in structural materials at both room and elevated temperatures. This approach involves

the formation of micron- or nano-sized second-phase precipitates within the matrix [16, 17]. These intermetallic compounds play a crucial role in impeding dislocation motion inside the material. The strengthening effect primarily arises from factors such as lattice mismatch, modulus difference, and interfacial characteristics between the matrix and the precipitates. By carefully controlling alloy composition and heat treatment processes, researchers have successfully introduced various types of intermetallics into HEAs to achieve effective strengthening. The effectiveness of precipitation strengthening depends on factors such as the lattice misfit, modulus difference, and interfacial characteristics between the matrix and precipitates. Through alloying design and precise heat treatment, researchers have introduced various types of intermetallics—such as B2-type (NiAl), $L2_1$-type (Ni2AlTi), η phase, Laves phases, σ phase, μ phase, and $L1_2$-type Ni_3Al—into HEAs to achieve tailored strengthening effects.

Coherent $L1_2$ nanoparticles are a classical type of shearable precipitates in FCC alloys and have been widely used in 3d transition-metal HEAs [18-21]. For example, He *et al.* added 2 at.% Al and 4 at.% Ti to a FeCoNiCr alloy, which results in the formation of coherent $L1_2$-Ni_3(Al,Ti) nanoparticles in the FCC matrix, improving the yield strength to more than 1000 MPa at room temperature [22]. Yang *et al.* developed a $(FeCoNi)_{86}Al_7Ti_7$ alloy with a high density of $L1_2$ nanoparticles, which exhibits a yield strength of 1000 MPa and an excellent ductility of ~ 50% [19]. On the other hand, some hard precipitates, such as σ, μ, and Laves phases, are also used for strengthening FCC-HEAs. It should be pointed out that although bypassed precipitates can drastically increase the yield strength of HEAs, excessive amounts of these phases can lead to a significant decrease in ductility due to the brittle nature of the hard precipitates. Given the respective advantages and limitations of coherent and incoherent precipitates,

designing advanced HEAs that incorporate both types of precipitates through dual precipitation has become an intriguing approach. By leveraging the strengths of each precipitate type and offsetting their weaknesses, this strategy aims to optimize mechanical properties and achieve exceptional performance in HEAs.

The microstructural parameters of precipitates—namely, size, number density, and volume fraction—play a crucial role in determining the effectiveness of precipitation strengthening. $L1_2$-ordered precipitates are produced via two distinct mechanisms: continuous precipitation (CP) and discontinuous precipitation (DP). CP leads to the even formation of $L1_2$ nanoparticles inside grains, accompanied by a gradual solute redistribution in the matrix [23, 24]. Conversely, DP generally begins at grain boundaries and propagates into the grain interiors via a cellular growth mechanism [25-27]. The morphological evolution and spatial distribution of strengthening phases—especially those formed via DP—have emerged as key factors influencing mechanical performance. DP-formed $L1_2$ precipitates, which often appear as nanoscale rods or lamellae aligned along grain boundaries, can simultaneously refine the grain size and introduce a high density of obstacles to dislocation motion. This microstructural architecture not only enhances strength through both grain boundary and precipitation strengthening but also offers pathways for improving ductility via controlled work-hardening mechanisms. Understanding how such microstructures form, coarsen, and interact with deformation processes is thus essential for the rational design of next-generation HEAs.

In addition, there remains significant potential for further optimization by synergistically combining the advantages of coherent and incoherent precipitates at multiple length scales. For instance, integrating DP-formed $L1_2$ nanorods with a secondary population of fine, incoherent σ nanoparticles could introduce hierarchical

obstacles to dislocation motion, thereby activating additional work-hardening mechanisms and further tuning the strength-ductility synergy. The development of such complex, multiphase architecture requires a deep understanding of the underlying thermodynamic and kinetic pathways, as well as advanced processing and characterization techniques.

Therefore, this thesis primarily addresses the following key scientific challenges: First, to resolve the strength–ductility trade-off in FCC HEAs, it is essential to design innovative dual-phase precipitation architectures that exploit the synergistic effects arising from the interaction between coherent and incoherent precipitates. Second, a comprehensive understanding of the core mechanisms governing the formation, kinetics, and thermal stability of DP-derived nanostructures—such as nanorods and lamellae—as well as their interplay with recrystallization processes, is critical. Finally, by developing hierarchical synergistic precipitation strategies that combine DP-generated coherent nanostructures with deliberately distributed incoherent nanoparticles, it is possible to achieve ultra-high strength while simultaneously enhancing both work-hardening capability and ductility.

1.2 Research Objectives

- To design and optimize synergistic strengthening effects in both CP and DP-FCC HEAs, thereby further advancing the strength-ductility trade-off.
- To understand the mechanisms controlling the formation, coarsening, and coupling with recrystallization of coherent DP-nanorods in HEAs.
- To mechanistically establish the relationship between DP-nanorods microstructure and mechanical properties of FCC HEAs at room temperatures.

1.3 Organization of this thesis

The thesis comprises seven chapters. In Chapter 1, the research background is introduced, and the primary research questions and objectives are outlined. Chapter 2 delivers a thorough summary of the latest developments in the field of M/HEAs. Chapter 3 details the methodologies employed, including material preparation, thermomechanical processing, microstructural characterization, and thermodynamic modeling. Chapter 4 investigates the dual-precipitation strategy in FCC HEAs, focusing on the synergistic strengthening effects of coherent $L1_2$ nanoparticles and incoherent Laves phases, and highlights their contribution to overcoming the strength–ductility trade-off. Chapter 5 systematically explores the formation mechanisms, coarsening kinetics, and mechanical consequences of DP-formed coherent $L1_2$ nanorods in FCC HEAs, emphasizing the coupling between DP and recrystallization as well as the resulting ultrafine-grained microstructures. Chapter 6 examines synergistic precipitation strengthening by integrating DP-formed $L1_2$ nanorods with σ-phase nanoparticles, revealing how hierarchical multiphase architectures further enhance strength, ductility, and work-hardening capacity in advanced HEAs. In Chapter 7, the key results of the study are summarized, the implications of these findings are examined, and potential directions for future research in intermetallic-strengthened HEAs are suggested.

Chapter 2 Literature review

2.1 Introduction to M/HEAs

Metallurgy and the resulting metallic materials play a pivotal role in the human civilization in the past century [28]. As societies continue to advance, the urgent need for improved energy efficiency and reduced greenhouse gas emissions has driven the search for new structural materials with superior performance. The rapid progress in materials science has highlighted the limitations of conventional single-element-based material design, which has now reached a bottleneck. In the 1990s, two pioneering research teams—led by Cantor B. and J.W. Yeh—broke away from traditional approaches by introducing the concept of multi-principal element alloys (MPEAs), opening up new possibilities for innovative alloy design. The so-called MPEAs [29], later known as HEAs [4], refer to emerging alloy systems that contain 5 or more components and the content of each component is between 5% and 35%. Unlike conventional alloys, this class of alloys lacks a primary element and instead exhibits the collective influence of multiple constituent elements. Owing to the high configurational entropy, the components are arranged in a highly disordered manner, which often leads to the formation of simple solid solution phases [4, 10, 30-35]. Various alternative terms are also used, such as multi-principal element alloys, equiatomic and near-equiatomic alloys, substitutional alloys, and multicomponent alloys. HEAs display a range of distinctive properties, including high entropy from a thermodynamic perspective, pronounced lattice distortion, slow diffusion kinetics, and enhanced phase stability [36, 37]. These structural features suggest that HEAs possess distinctive mechanical properties, particularly in terms of high-temperature rheological behavior and creep

resistance, making them highly promising candidates for high-temperature structural applications. This innovative alloy design concept also opens up new opportunities to explore the vast, previously untapped compositional space [38]. As shown in Fig. 2.1, the design strategies for conventional alloys and HEAs differ significantly on a ternary plot.

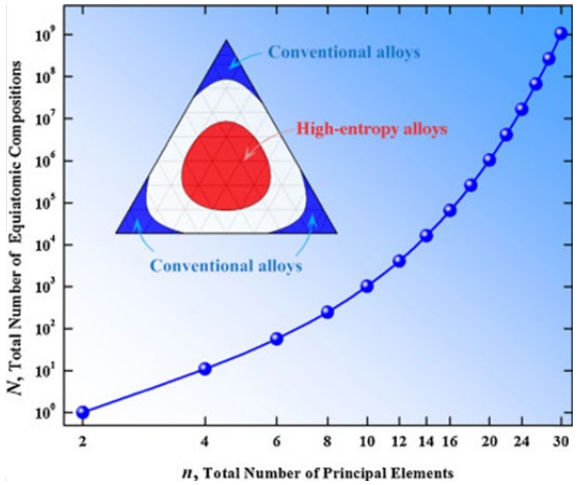

Fig. 2.1. A schematic diagram illustrating HEAs: the relationship between the number of principal elements and the corresponding number of equiatomic compositions [38].

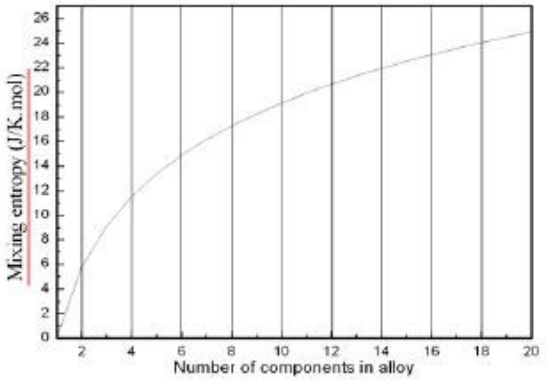

Fig. 2.2. The change curve of configuration entropy (mixing entropy) in a disordered equal atomic ratio alloy with the increase in the number of alloying elements [4].

Figure 2.2 the trend of mixing entropy in alloys as the number of constituent elements increases. It is evident that when an alloy contains five or more elements, its mixing entropy reaches a relatively high value. However, as the number of elements

exceeds thirteen, further increases in mixing entropy become much less significant. Therefore, HEAs are typically designed to contain between five and thirteen principal elements. Additionally, these elements do not necessarily need to be present in equal atomic ratios; instead, their concentrations generally range from 5 at.% to 35 at.%. This design approach enables the formation of alloy systems characterized by a random, miscible state and the presence of multiple principal elements [4, 8, 30-32]. According to this widely accepted but not rigorous definition standard, a considerable number of alloys currently belong to the HEAs system.

2.2 Unique features

HEAs are distinguished by several key features, including the high entropy effect, lattice distortion, sluggish diffusion, and the cocktail effect [39]. According to widely accepted definitions, HEAs are composed of multiple elements in relatively balanced molar proportions, a feature that gives rise to their distinctive properties.

The high entropy effect represents a fundamental concept in HEAs. According to the classical Gibbs phase rule, an alloy composed of n elements can theoretically reach up to $p = n + 1$ equilibrium phases. In contrast, during non-equilibrium solidification, the number of phases may exceed this limit ($p > n + 1$) [34, 40-43]. Traditional alloy theory suggests that alloys with multiple components are prone to forming various intermetallic compounds, which can compromise their mechanical properties. However, research has shown that HEAs often form simple solid solution phases, such as FCC, BCC, or even some amorphous structures, rather than brittle intermetallic compounds, thereby avoiding the deterioration of mechanical performance. From the Gibbs free energy expression $\Delta G_{mix} = \Delta H_{mix} - T\Delta S_{mix}$, The competition between mixing entropy

and mixing enthalpy is evident, and at higher temperatures, entropy becomes the prevailing factor affecting the system's free energy. This elevated mixing entropy in HEAs lowers the system's free energy in a disordered configuration, extends the solubility limits for intermetallic compounds, and encourages the creation of simple multi-component solid solutions. For example, the phase diagram of $Al_xCrFeCoNiCu$ HEAs measured by thermodynamic analysis method is shown in Fig. 2.3 [44]. Within a specific compositional range, the phase constitution of HEA systems is less complex than one might expect, and their microstructures remain as clearly distinguishable as those of conventional alloys, greatly facilitating HEA research.

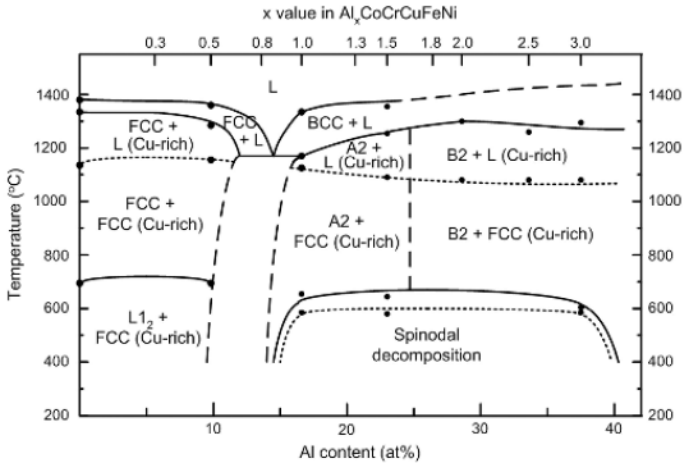

Fig. 2.3. Phase diagram illustrating the $Al_xCoCrCuFeNi$ system across different levels of aluminum content [44].

The lattice distortion effect refers to pronounced distortions in the crystal lattice, which occur due to the incorporation of atoms with varying atomic radii in complex, multi-element phases [45]. The atomic displacement at each lattice site in HEAs is affected by both the identity of the atom at that site and the types of adjacent atoms, resulting in lattice distortions that are typically more severe than in conventional alloys. HEAs readily form solid solution phases containing multiple principal elements, making it challenging to distinguish between solute and solvent atoms using traditional

crystal structure concepts. The considerable mismatch in atomic sizes and bonding characteristics of different elements gives rise to significant lattice distortion in high-entropy alloys [4, 46]. Such a distorted lattice would alter the defect behaviors and result in a unique phase segregation that is different from those in the conventional alloys, resulting in lattice distortion as shown in the Fig. 2.4 [45]. When the differences in atomic sizes are substantial and the associated distortion energy is high, the initially stable simple crystal lattice can become destabilized, potentially resulting in the emergence of alternative, more stable crystal structures, such as intermetallic compound phases.

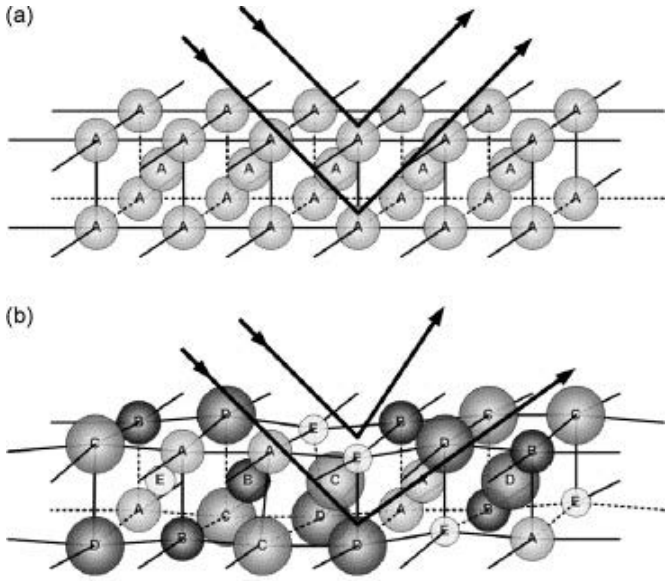

Fig. 2. 4. (a) Crystal lattice with identical atoms; (b) lattice distortion resulting from a solid solution of differently sized atoms, which are statistically distributed at random throughout the crystal structure [45].

The sluggish diffusion observed in HEAs is an inherent consequence of the distorted lattice stress fields impeding atomic movement, combined with the challenge of coordinating the diffusion of numerous different elements [47, 48]. Tsai *et al.* provided the first accurate experimental evidence confirming this key feature in 2013.

[49]. Compared to that in conventional alloy matric es, the individual diffusion coefficients in this HEAs are indeed relatively smaller. As shown in Fig. 2.5, by conducting various high-temperature diffusion experiments on the FeCoNiCrMn system, researchers have successfully determined the self-diffusion rates of each element within the HEA matrix, as well as the corresponding activation energies for lattice diffusion. Compared to conventional alloys, the individual diffusion coefficients in these M/HEAs are noticeably lower.

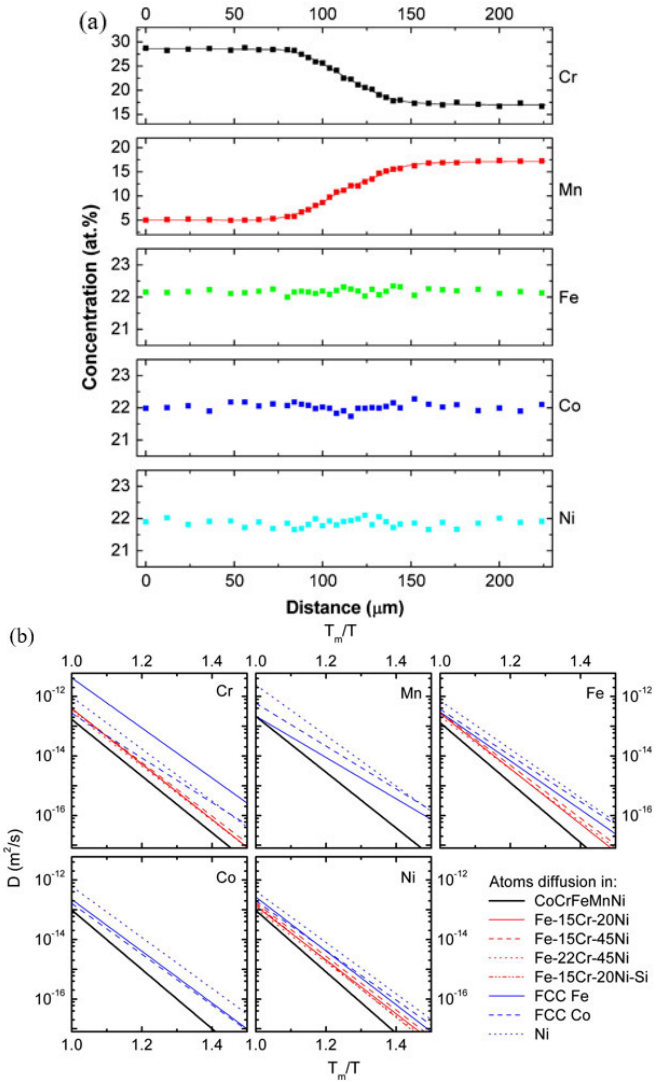

Fig. 2.5. (a) The composition distribution of the diffusion couple at the interface of the FeCoNiCrMn HEAs system (in the Cr-Mn couple), and (b) temperature dependence of the diffusion coefficients of Cr, Mn, Fe, Co, and Ni in various matrices [49].

The "cocktail effect," a term first introduced by Prof. Ranganathan, effectively illustrates how the complex interplay among different alloying elements can result in properties that greatly exceed those anticipated by straightforward mixture rules [50]. Originally, this term was coined to refer to three unique types of alloys: bulk metallic glasses, super-elastic and super-plastic metals, and HEAs [51]. All of these alloy types are defined by their complex and concentrated chemical compositions [52]. The "cocktail" effect explains the extraordinary properties found in fully amorphous bulk metallic glasses and the exceptional structural and functional characteristics of “gum” metals. For instance, adding light elements leads to a reduction in the overall density of the alloy, and introducing elements with excellent oxidation resistance, such as Al, Cr, and Si, enhances its resistance to oxidation at elevated temperatures. Figure 2. 6 shows the hardness and lattice constant of the $Al_xCrFeCoNiCu$ HEAs system [44]. Similar to how carbon enhances the properties of steel, incorporating Al into the HEA system significantly increases its strength and hardness.

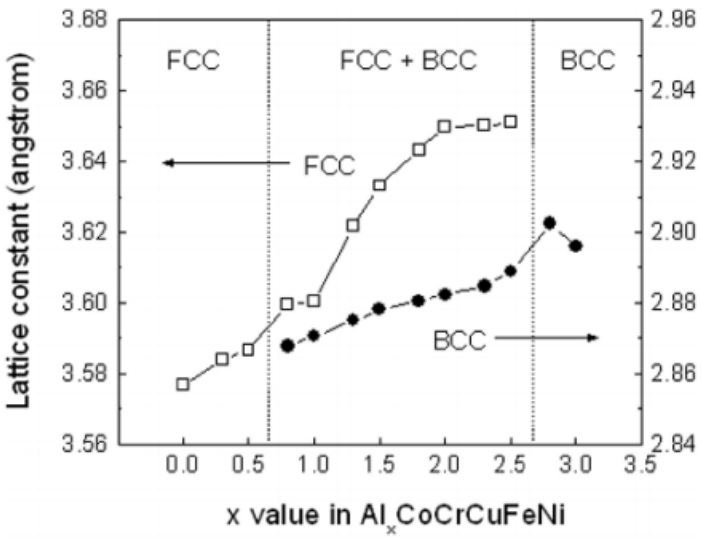

Fig. 2.6. Lattice constants of $Al_xCoCrCuFeNi$ alloy system with different Al contents, □ FCC phase and ● BCC phase [44].

2.3 Precipitate strengthened M/HEAs

2.3.1. Background of the precipitation-strengthened M/HEAs

Among their notable characteristics, the most fascinating feature of HEAs lies in their tendency to form single-phase solid solutions. Considerable research has focused on identifying the physical principles that govern this unique metallurgical behavior. Figure 2.7 shows all alloy subsets of the quinary HEAs FeNiCoCrMn [53]. Single-phase HEAs with an FCC structure have received significant attention from the materials community, as they exhibit outstanding mechanical properties and excellent resistance to fracture.

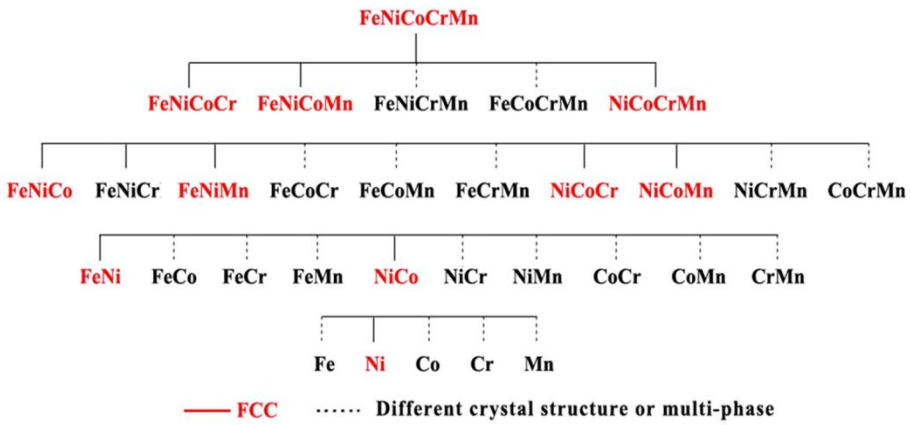

Fig. 2.7. Every possible subset—including quaternary, ternary, binary, and pure elements—of the quinary FeNiCoCrMn HEAs. Upon completion of casting and homogenization, single-phase FCC HEAs are denoted in red, in contrast to multi-phase or differently structured alloys, which are marked in black [53].

Figure 2.8(a) demonstrates that FeNiCoCrMn exhibits a yield strength of 759 MPa and a ductility of approximately 55% [3]. Interestingly, both the strength and ductility of this alloy increase simultaneously as the testing temperature drops to 77 K. Even more notably, the HEA demonstrates exceptional toughness, exceeding 300 MPa/m^2

for stable crack growth at 77 K, which rivals that of the best cryogenic steels (Fig. 2.8b) [3]. As illustrated in Fig. 2.8b, the toughness of this alloy significantly surpasses that of conventional materials, including low-alloy steels, nickel- and cobalt-based superalloys, and most metallic glasses.

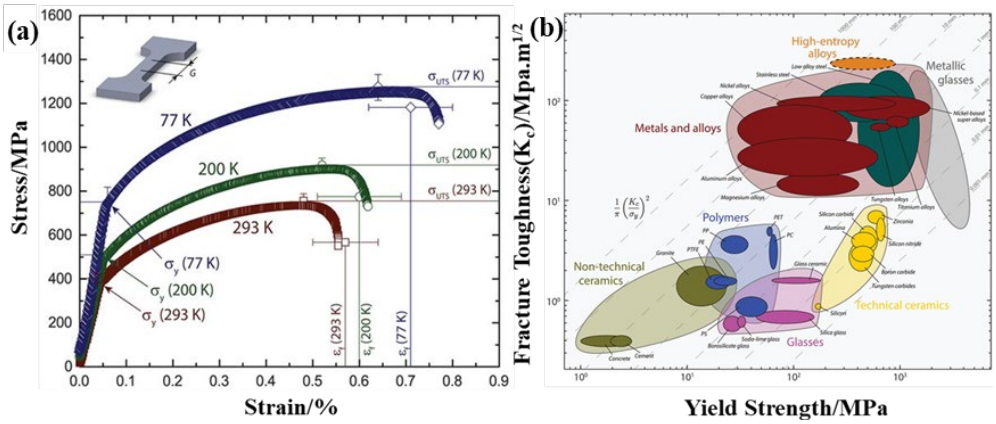

Fig. 2.8. (a) Mechanical properties of the FeNiCoCrMn HEA measured at 293 K, 200 K, and 77 K; (b) the alloy's superior damage tolerance, reflected in its combination of strength and toughness, exceeds that of most pure metals and alloys [3].

Although a single-phase FCC M/HEAs matrix alone does not offer sufficient strength, its exceptional ductility and excellent strain-hardening capability make it an ideal base alloy for subsequent precipitation hardening. This strategy has been demonstrated to be among the most effective methods for strengthening metallic materials intended for structural applications at both ambient and elevated temperatures. [18, 54-56]. Alloying to induce precipitation of a secondary phase is widely regarded as the most efficient and successful method for enhancing strength of HEAs [55, 57-59]. The introduction of second-phase particles via the precipitation of unstable solutes from solution can significantly affect material properties. The interaction between dislocations and these particles is largely governed by factors like the size, volume fraction, and intrinsic nature of the precipitates. These factors collectively influence the

extent of particle-dislocation interactions. During precipitation, solutes are first dissolved in the molten metal and subsequently form fine particles upon cooling. Among various metallurgical techniques, alloying to induce second-phase precipitation remains one of the most effective and widely used methods for strengthening materials.

The primary factors contributing to strengthening are differences in modulus, antiphase boundary energy, and stacking fault energy, while misfit strains play a comparatively minor role. Conversely, the contributions from interface step energy and core energy differences are generally negligible. Although lattice mismatch can significantly enhance strength, it often reduces ductility and can also accelerate precipitate coarsening at high temperatures. Consequently, many alloy systems strive to minimize lattice mismatch, despite its strengthening potential. A noteworthy aspect of precipitation-hardened alloys is how their strength varies with precipitate size. With increasing particle size, the strength of the alloy first increases and then gradually diminishes, even if the volume fraction of particles—and consequently antiphase boundary energy, stacking fault energy, or misfit strain energy—remains constant. In the regime where dislocations cut through particles, larger particles intensify the dislocation-particle interaction, necessitating greater dislocation curvature and raising the average number of obstacles per unit length of dislocation, which leads to enhanced strength. However, as particles grow larger and their spacing becomes more random, a point is reached where dislocations can no longer cut through particles and must bypass them by looping, resulting in a change in the strengthening mechanism.

Precipitation hardening provides a much more substantial strengthening effect than other mechanisms. Based on the nature of the precipitates, precipitation-strengthened HEAs can be divided into two types: those containing incoherent

intermetallic precipitates (such as σ, η, μ, and Laves phases) and those incorporating coherent precipitates (such as the $L1_2$ phase).

2.3.2. Incoherent precipitation strengthened M/HEAs

Many studies have established that minor additions of elements like Al, Nb, Mo, or Ti promote the formation of incoherent intermetallic phases, such as B2-NiAl, δ, η, σ, and Laves. These elements exhibit a strong affinity for forming covalent bonds with transition metals with partially filled d shells, including Ni, Fe, Co, and Cr. [60-63].

The Nb-modified eutectic HEA system developed by Liu *et al*. displayed notable mechanical performance [61]. The substantial size difference between Nb atoms and the other principal elements results in pronounced lattice distortion when Nb is added to the CoCrFeNi alloy. This addition facilitates the formation of a fine lamellar eutectic structure, composed of a ductile FCC phase and a hard, Nb-rich Laves phase. As the Nb content increases, so does the volume fraction of the Laves phase, thereby enhancing both hardness and strength. However, an excessively high Nb content gives rise to interconnected, brittle regions of the Laves phase. This, in turn, causes a marked reduction in ductility, as observed in the $CoCrFeNiNb_{0.2}$ alloy (see Fig. 2.9a). Cracks forming within the ordered, Nb-rich Laves phase can quickly propagate through the interconnected brittle phase network, ultimately causing early and brittle failure.

The presence of discrete, hard topologically close-packed (TCP) phases was expected to deliver superior strengthening compared to the Nb-induced eutectic structure within the CoCrFeNi matrix. Building on this concept, Liu *et al*. designed a $FeCoCrNiMo_x$ alloy system, in which hard σ and μ phases serve as the primary strengthening agents [16]. The significant yield stress increment with a decent ductility

of 19% can be achieved in FeCoNiCrMo$_x$ HEAs decorated with finely dispersed hard σ and μ phases with average size of 50~100 nm (Fig. 2.9b). These outstanding mechanical properties are believed to result from the alloy's remarkable work hardening capability—a work hardening exponent of 0.75 in the HEA base alloy. This high work hardening ability helps suppress the propagation of microcracks originating at the precipitate-matrix interface and enables extensive plastic deformation.

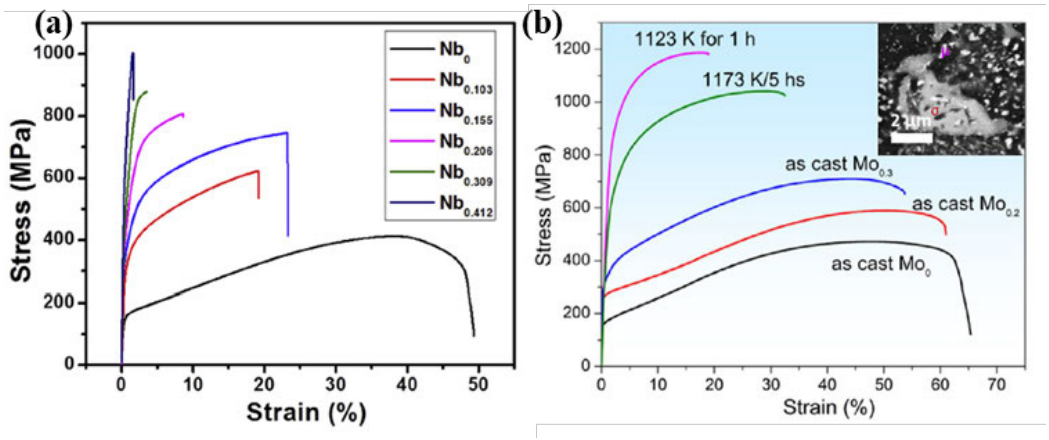

Fig. 2.9. (a) Compressive engineering stress–strain curves of FeCoCrNiNb$_x$ alloys at room temperature; (b) Compressive engineering stress–strain curves of FeCoNiCrMo$_x$ alloys at room temperature [16, 61].

The excellent mechanical performance of the precipitation-hardened CoCrFeNiMo$_{0.3}$ alloy can be attributed to several key factors. Firstly, the hard precipitates are discretely distributed throughout the FCC matrix, eliminating the risk of brittle failure that often arises from interconnected brittle phases. Secondly, these fine, hard precipitates—formed during annealing at 850–900 °C—significantly enhance the hardness of the ductile FCC matrix. Crucially, the FCC matrix possesses an exceptionally high work hardening exponent, allowing for substantial plastic deformation and effectively inhibiting the propagation of microcracks initiated by these precipitates [16]. Collectively, these metallurgical factors result in elevated fracture

strength and satisfactory ductility in the $CoCrFeNiMo_{0.3}$ alloy, strengthened by both σ and μ particles. However, the inherent brittleness of these hard intermetallic precipitates, together with the substantial lattice mismatch between the precipitates and the matrix, typically causes a significant reduction in ductility, particularly in alloys containing a high density of precipitates as strength is increased.

2.3.3. Coherent precipitation strengthened M/HEAs

Drawing inspiration from the design principles of commercial superalloys, researchers have incorporated the $L1_2$ phase into FCC HEAs [64]. By carefully adding appropriate amounts of Al and Ti to the FCC matrix, researchers have achieved a supersaturated solid solution at high temperatures, which then yields nanoscale $L1_2$ precipitates upon annealing at intermediate temperatures. Notably, the coherent precipitation of $L1_2$-type phases offers exceptional strengthening, enabling an impressive balance between ductility and strength. Compared to conventional steels and superalloys, these innovative $L1_2$-strengthened HEAs uniquely combine the ductility of the HEA matrix with the robust strengthening provided by the $L1_2$ phase. As a result, they exhibit outstanding physical and mechanical property combinations, making them increasingly attractive for research and advanced engineering applications. He *et al.* developed a series of $L1_2$ strengthened FeCoCrNi based HEAs with different additions of Ti and Al [65]. By carefully adjusting the alloy composition and microstructure through aging treatment, a mixture of nanoscale $L1_2$-Ni_3(Al, Ti)-type γ′ precipitates with two distinct morphologies was achieved. The optimized $(FeCoCrNi)_{96}Al_4Ti_2$ HEA demonstrates exceptional tensile properties at room temperature, combining a high

tensile strength of 1273 MPa with impressive ductility of approximately 17%. (Fig. 2.10).

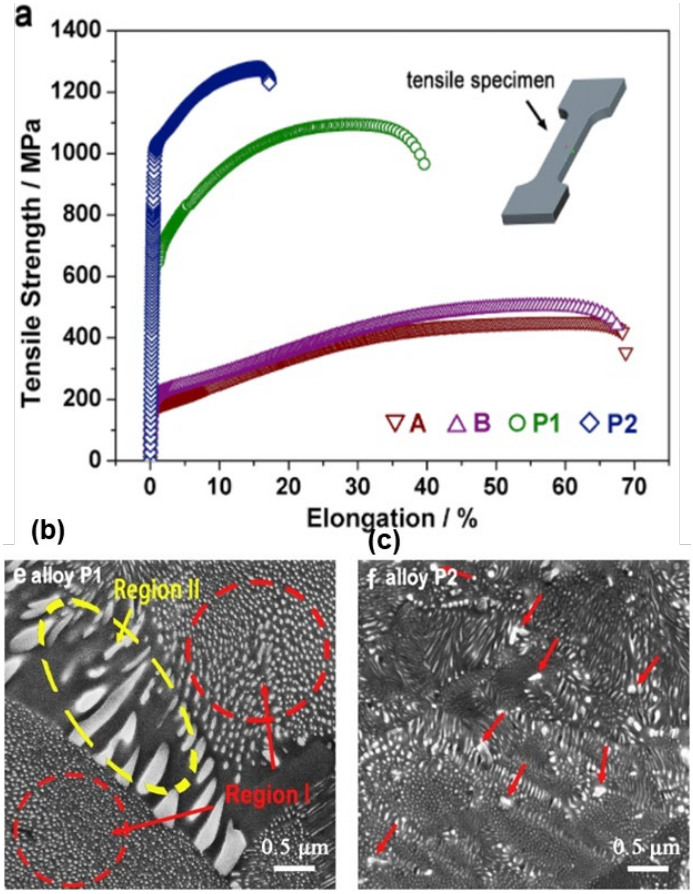

Fig. 2.10. (a) Room temperature tensile properties of the alloys: CoCrFeNi (A), $(CoCrFeNi)_{94}Ti_2Al_4$ (B), $(CoCrFeNi)_{94}Ti_2Al_4$ processed by 30% rolling, followed by annealing at 1273 K for 2 hours and aging at 1073 K for 18 hours (P1), and $(CoCrFeNi)_{94}Ti_2Al_4$ processed by 70% rolling and subsequent aging at 923 K for 4 hours (P2). (b) and (c) display the microstructures of P1 and P2, respectively. [65].

In addition, Yang *et al*. introduced a new precipitation-strengthened HEA featuring a pure "$L1_2$ + FCC" dual-phase structure, in which no brittle phases are present [19]. As shown in Fig. 2.11a, the $L1_2$ nanoprecipitate-strengthened high-entropy alloy exhibits an exceptional combination of strength and ductility at room temperature, with a yield strength exceeding 1000 MPa, an ultimate tensile strength reaching 1500 MPa, and a uniform elongation as high as 50%. These strength levels are 3–5

times higher than those of single-phase FCC-based high-entropy alloys, while still maintaining excellent work-hardening capability. This outstanding mechanical performance is closely related to its unique deformation mechanisms (Fig. 2.11b). At the initial stage of plastic deformation (10% strain), dislocation planar slip is the predominant deformation mechanism. As the strain increases to 20%, the development of high-density dislocation walls and the occurrence of cross-slip contribute significantly to both short-range effective stress hardening and long-range back-stress hardening. In the later stage of plastic deformation (38% strain), the formation of deformation-induced microbands further enhances the stability of plastic deformation.

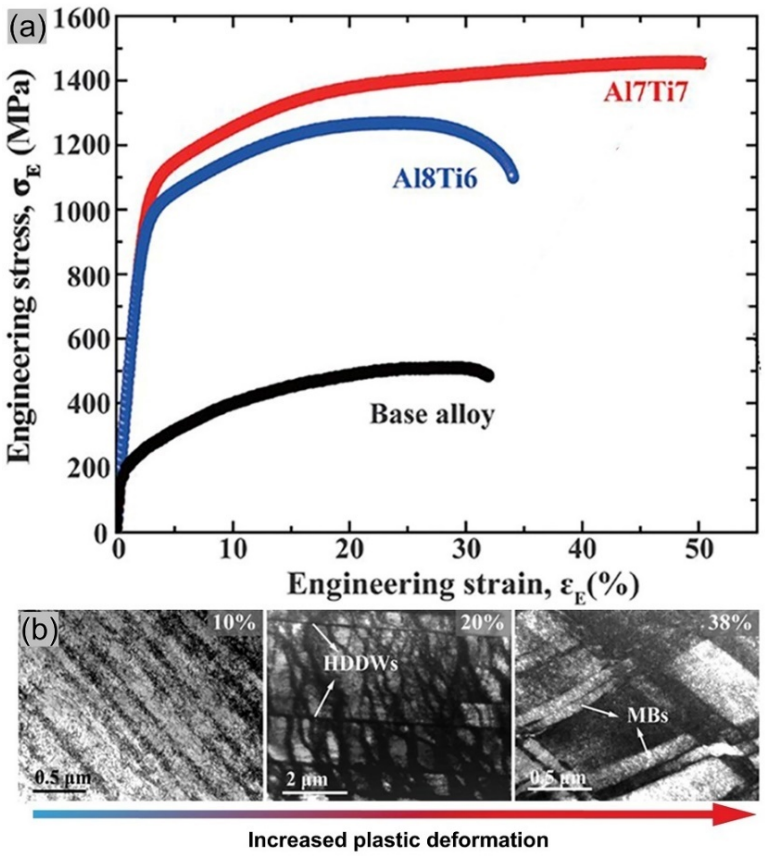

Fig. 2.11. Tensile properties and deformation microstructure of the $(FeCoNi)_{86}Al_7Ti_7$ alloy: (a) engineering stress–strain curves, and (b) dynamic evolution of deformation substructures [19].

All of this evidence suggests that precipitation strengthening in single-phase FCC HEAs can be precisely tailored through the judicious selection of alloying elements and compositions. Notably, the formation of secondary-phase precipitates induces a pronounced hardening effect, leading to significant enhancements in both the yield strength and ultimate tensile strength of FCC-type HEAs. Among the various strengthening strategies, the introduction of coherent $L1_2$ precipitates is particularly effective in achieving an optimal balance between strength and ductility. In these alloys, $L1_2$ precipitates can form uniformly and at a sufficiently fine scale within the FCC matrix. Owing to their coherency with the matrix and nanoscale dimensions, these $L1_2$ precipitates are typically sheared by moving dislocations. This precipitation shearing mechanism increases alloy strength while minimizing the reduction in ductility. However, it should be noted that the overall strengthening effect remains moderate, with the yield strength of most $L1_2$ precipitate-strengthened HEAs generally remaining below 1200 MPa.

2.3.4. Composite precipitation-strengthened HEAs

In recent years, researchers have sought to further enhance the mechanical properties of HEAs by employing composite precipitation strategies. The advantage of composite precipitation strengthening lies in the simultaneous introduction of multiple types of precipitates with distinct characteristics, such as the combination of coherent and incoherent precipitates, or the construction of hierarchical precipitation structures at different length scales. By leveraging the synergistic interactions between these precipitates, the overall mechanical performance of the alloy can be significantly improved [66, 67].

Li *et al*. [68] systematically investigated the nanoscale precipitation behavior, microstructural evolution, and mechanical properties of $(CoCrFeNi)_{87}Al_7Ti_6$ (at.%) FCC/$L2_1$ eutectic HEAs during aging. Their results demonstrated that aging treatment promotes the precipitation of coherent $L1_2$ nanoparticles within the FCC phase, as well as coherent BCC nanoparticles within the $L2_1$ phase, resulting in a unique hierarchical composite precipitation structure of FCC $L1_2$ + $L2_1$/BCC. This structural design significantly enhances the alloy's strength while maintaining good ductility. Microstructural characterization and thermodynamic analysis further revealed that nanoscale precipitation in both the FCC and $L2_1$ phases does not proceed via conventional one-step nucleation; instead, it involves a two-stage process: initial spinodal decomposition followed by a structural transformation. (Fig. 2.12).

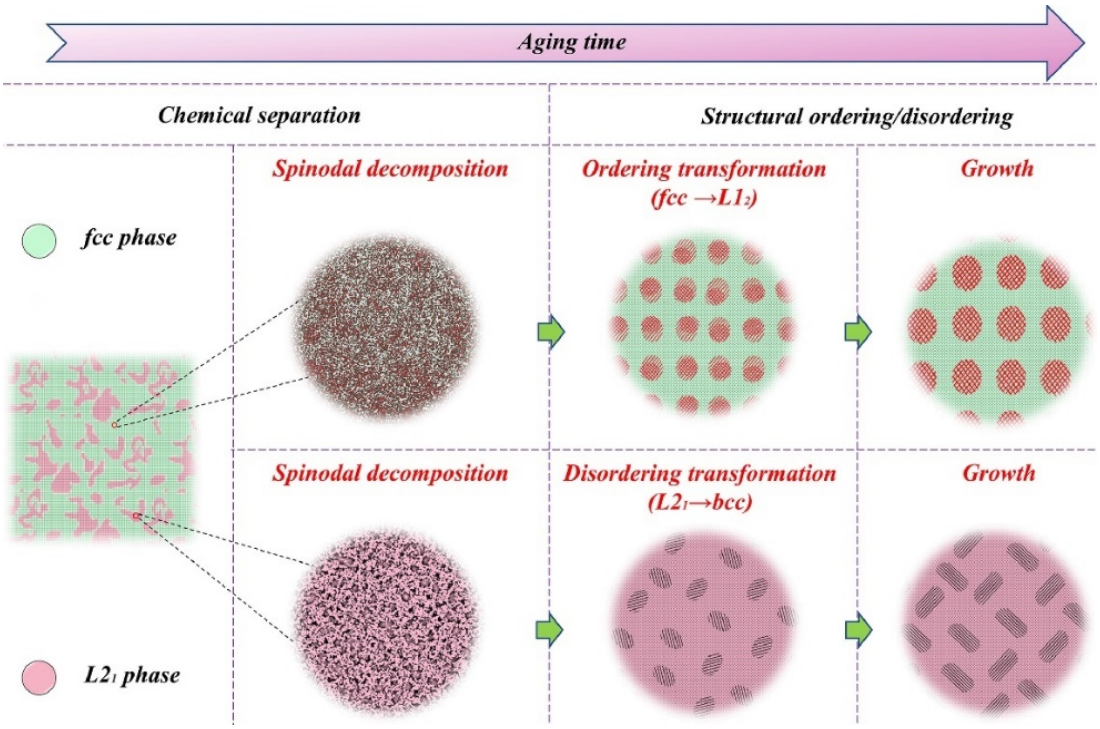

Fig. 2.12. Schematic diagram depicting the precipitation mechanisms of $L1_2$ and BCC nanoprecipitates in the FCC and $L2_1$ phases of a eutectic HEA [68].

Li *et al*. [69] proposed a novel stepwise and controllable coherent nanoprecipitation strategy to achieve composite precipitation strengthening in W-based refractory HEAs. By carefully designing the heat treatment process, two types of nanoscale precipitates with distinct morphologies and structures—δ lamellae and γ" particles—were introduced into the BCC and FCC dual-phase matrix. Mechanical property testing revealed that this alloy achieves a remarkable tensile strength of up to 2150 MPa, with a uniform elongation exceeding 15%, demonstrating an outstanding combination of strength and toughness. Compared to single-mode precipitation strengthening, this stepwise and controllable composite coherent nanoprecipitation approach enables the sequential formation of multiple precipitate types over different temperature ranges, thereby harnessing their respective roles in strengthening and ductility enhancement. Although the δ and γ" phases differ in morphology and structure, both maintain good coherency with their respective matrices, possess similar chemical compositions, and exhibit excellent thermal stability.

In summary, composite precipitation strengthening offers a new paradigm for tuning the mechanical properties of HEAs. Through the rational design and combination of various precipitate types, the synergistic effects of different precipitates on strengthening, plastic deformation, and work hardening can be fully exploited, overcoming the limitations of single-phase precipitation strengthening and achieving exceptional strength-ductility synergy at ultrahigh strength levels. Therefore, a deep understanding of the thermodynamic and kinetic fundamentals governing the roles of multiple principal elements, precipitation mechanisms, and structural evolution in composite precipitation-strengthened HEAs—as well as precise control over the composition, size, morphology, and distribution of precipitates—is key to unlocking the full potential of composite precipitation strengthening.

2.4 Precipitation modes of $L1_2$ precipitates

In supersaturated FCC HEAs, precipitation can proceed via either a continuous or discontinuous pathway. Here, “continuous” and “discontinuous” describe whether there is a gradual or abrupt change in chemical composition between the precipitates and the surrounding matrix [70]. CP is characterized by the uniform distribution of $L1_2$ nanoparticles throughout the grains, accompanied by a gradual and continuous change in solute concentration within the matrix. In contrast, DP originates at grain boundaries and propagates inward as a transformation front, resulting in a distinctive rod- or lamella-like microstructure consisting of alternating $L1_2$ precipitates and a solute-depleted matrix. The morphology formed by DP typically appears as lamellar, rod-like, or occasionally fibrous structures. These two precipitation mechanisms—CP and DP—are competitive and may coexist in $L1_2$-strengthened high-entropy alloys.

For instance, Fang et al. systematically investigated the influence of aging temperature, aging time, and grain size on the characteristics of CP and DP in $L1_2$-strengthened HEAs [71]. Their findings indicate that lower temperatures preferentially facilitate the DP reaction, whereas higher temperatures favor the CP reaction. At intermediate temperatures, CP and DP coexist and compete, with the solute concentration gradient between the two regions acting as the driving force for the advancement of DP. Moreover, grain refinement markedly enhances the DP reaction and results in a microstructure dominated by DP, due to the increased availability of nucleation sites and accelerated diffusion pathways (Fig. 2. 13). In addition to deepening the understanding of CP and DP mechanisms, this study offers important guidance for the microstructural design and optimization of advanced $L1_2$-strengthened HEAs.

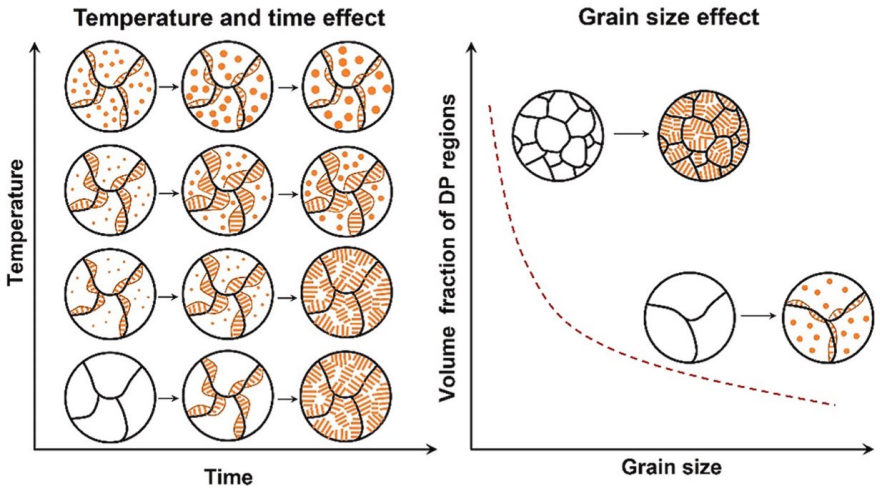

Fig. 2.13. Schematic diagram depicting the microstructural evolution of $L1_2$-strengthened HEAs [71].

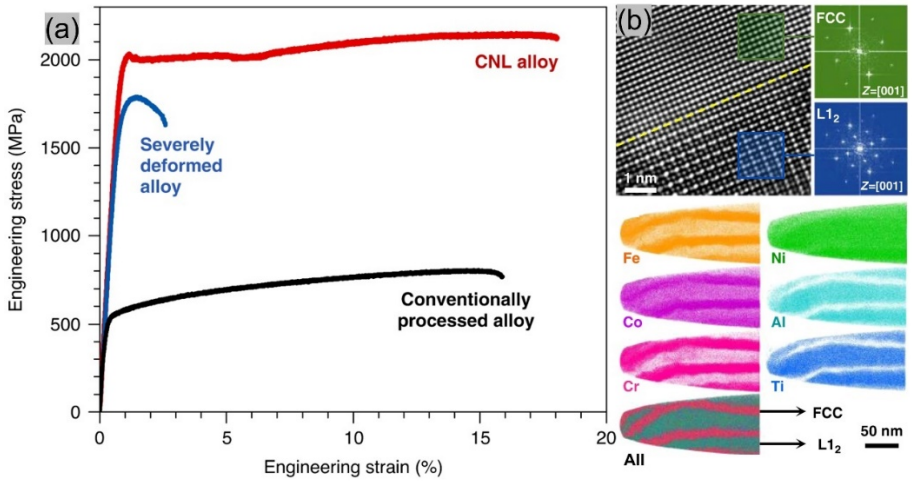

Figure 2.14 Mechanical performance and microstructural features of the coherent nano-lamellar alloy: (a) Engineering stress–strain responses; (b) Interfacial coherency and elemental distribution within FCC/$L1_2$ nano-lamellae [21].

Rather than simply promoting CP and suppressing DP, refining the morphology of DP rods has also been shown to effectively mitigate the adverse effects associated with coarse DP structures. For instance, Fan *et al*. [21] developed an advanced high-entropy alloy featuring a fully lamellar microstructure composed of alternating ultrafine $L1_2$ precipitates and FCC matrix, achieving outstanding mechanical properties with a yield strength exceeding 2000 MPa and uniform tensile ductility of 16% (Fig. 2.14).

The effectiveness of precipitation strengthening is strongly influenced by factors such as precipitate size, number density, and spatial distribution. Therefore, a comprehensive understanding of precipitation behavior and mechanisms in these complex alloy systems is crucial for the precise control of microstructure and mechanical properties in precipitation-strengthened HEAs.

2.5 Summary

Based on the abovementioned review of M/HEAs, the single-phase FCC M/HEAs can be significantly strengthened by introducing uniform nanoparticles, ultrafine DP nano-rods, and the synergistic addition of hard intermetallic compounds. In particular, the strategy of combining coherent and incoherent precipitates leverages their complementary advantages, enabling a remarkable enhancement in both strength and ductility compared to single-mode strengthening. The introduction of DP-formed nanorod structures not only provides effective precipitation and grain refinement strengthening, but also offers unique opportunities for tailoring microstructures towards ultrahigh performance. However, the formation and evolution of these DP nanorods involve complex thermodynamic and kinetic pathways, including interface migration, solute redistribution, and recrystallization coupling. Therefore, a deep understanding of the fundamental mechanisms and kinetics governing DP-formed nanorod precipitation is essential for precise microstructural control and the design of next-generation high-entropy alloys with exceptional mechanical properties. The synergistic strengthening effect, underpinned by both coherent and incoherent precipitates, together with advanced control over DP nanorod structures, represents a promising route for overcoming the traditional strength-ductility trade-off in advanced structural materials.

Chapter 3 Methodology

3.1 Material preparation

For the first research, The 3 alloys with compositions of $(Ni_2Co_2FeCr)_{96-x}Al_4Nb_x$ (x = 3, 5, and 7, at.%) were fabricated by arc-melting a mixture of high-purity raw elements (> 99.9% purity) in a Ti-gettered argon atmosphere. For simplicity, these alloys were hereafter referred to as the 3Nb, 5Nb, and 7Nb alloys, respectively. The melting was repeated five times, and electromagnetic stirring was used to ensure chemical homogeneity. The molten alloys were drop-cast into a copper mold with a cavity of 50 × 15 × 3 mm^3. The cast ingots were homogenized for 2 h at 1200 °C and then quenched to room temperature in water. After that, the ingots were cold-rolled along the longitudinal direction with a total thickness reduction of ~ 67% and subjected to recrystallization for 3 min at 1150 °C, followed by water quenching and isothermal annealing at 700 ℃ for various periods of time.

For the second research, an alloy with the nominal composition of $(CoCr_{0.5}FeNi_{1.5})_{87.5}Al_{7.5}Ti_5$ (at.%) was fabricated by arc-melting a mixture of high-purity elemental metals (>99.9% purity) in a Ti-gettered argon atmosphere. To ensure chemical homogeneity, the melting process was conducted five times with electromagnetic stirring. The molten alloy was then drop-cast into a copper mold with a cavity measuring 50 × 15 × 6 mm^3. The resulting ingots were homogenized at 1150 °C for 2 hours and subsequently water-quenched to room temperature. The ingots were then cold-rolled along the longitudinal direction to achieve a total thickness reduction of approximately 90%, followed by isothermal aging at 500–800 °C for various durations.

For the third research, with the nominal composition $(Ni_{1.75}FeCoCr_{0.75})_{86}Al_{10}Ti_4$ (at.%), ingots were fabricated by arc-melting high-purity raw metals (>99.9% purity) under a Ti-gettered argon atmosphere. To ensure chemical homogeneity, the melting process was repeated five times with electromagnetic stirring. The molten alloy was then drop-cast into a copper mold (cavity dimensions: 50 × 15 × 6 mm^3). The cast ingots underwent homogenization at 1150 °C for 2 h followed by water quenching. Subsequently, the ingots were cold-rolled to a 90% thickness reduction along the longitudinal direction and then isothermally aged at 600 °C for 24 h. Additionally, a counterpart alloy with identical composition was prepared using traditional processing (denoted TPA). Following 90% cold rolling, this TPA alloy was recrystallized at 1150 °C for 3 minutes prior to aging at 600 °C for 24 h. The chemical compositions of the $(Ni_2Co_2FeCr)_{96-x}Al_4Nb_x$ (x = 3, 5, and 7), $(CoCr_{0.5}FeNi_{1.5})_{87.5}Al_{7.5}Ti_5$, and $(Ni_{1.75}FeCoCr_{0.75})_{86}Al_{10}Ti_4$ (at.%) alloys are shown in Table 3.1. The specific heat-treatment parameters are presented in Table 3.2.

Table 3.1. Chemical compositions of the $(Ni_2Co_2FeCr)_{96-x}Al_4Nb_x$ (x = 3, 5, and 7), $(CoCr_{0.5}FeNi_{1.5})_{87.5}Al_{7.5}Ti_5$,and $(Ni_{1.75}FeCoCr_{0.75})_{86}Al_{10}Ti_4$ (at.%) alloys.

	Ni	Co	Fe	Cr	Al	Nb	Ti
$(Ni_2Co_2FeCr)_{93}Al_4Nb_3$	31.0	31.0	15.5	15.5	4.0	3.0	—
$(Ni_2Co_2FeCr)_{91}Al_4Nb_5$	30.3	30.3	15.2	15.2	4.0	5.0	—
$(Ni_2Co_2FeCr)_{89}Al_4Nb_7$	29.7	29.7	14.8	14.8	4.0	7.0	—
$(Ni_{1.5}CoFeCr_{0.5})_{87.5}Al_{7.5}Ti_5$	32.8	21.9	21.9	10.9	7.5	—	5
$(Ni_{1.75}CoFeCr_{0.75})_{86}Al_{10}Ti_4$	36.2	18.1	18.1	13.6	10.0	—	4.0

Table 3.2. Heat-treatments of $(CoCr_{0.5}FeNi_{1.5})_{87.5}Al_{7.5}Ti_5$ alloy.

Temperature	Aging time
500 °C	0.5 h
500 °C	2 h
500 °C	8 h
500 °C	32 h
600 °C	0.5 h
600 °C	2 h
600 °C	8 h
600 °C	32 h
700 °C	0.5 h
700 °C	2 h
700 °C	8 h
700 °C	32 h
800 °C	0.5 h
800 °C	2 h
800 °C	8 h
800 °C	32 h

3.2 Microstructure and nanostructure characterization

In this thesis, microstructural and nanostructural analyses were conducted using a range of characterization techniques, including X-ray diffraction (XRD), scanning electron microscopy (SEM) equipped with energy-dispersive X-ray spectroscopy (EDS), electron backscatter diffraction (EBSD), transmission electron microscopy

(TEM), three-dimensional atom probe tomography (APT), and small-angle neutron scattering (SANS).

The crystal structures were examined by Rigaku Smart Lab XRD system, and the specimens were prepared by grounding on silicon carbide paper from 240 to 7000 grit. XRD patterns were measured using Cu Ka radiation scanning from 35°-60° in 2θ with a scanning rate of 7 °/min. Microstructures of the alloys were characterized using Tescan MIRA field-emission scanning electron microscopy (FE-SEM) equipped with EDS. The samples were polished using standard mechanical procedures, followed by electrochemical etching in 40% aqua regia for durations ranging from 30 seconds to 2 minutes, depending on the alloy. To characterize the crystal orientation, phase distribution, recrystallization degree, and dislocation density in the alloys, the specimens were analyzed using electron backscatter diffraction (EBSD). EBSD samples were prepared by electrochemical polishing in a solution consisting of 20 vol.% HNO_3 and 80 vol.% C_2H_5OH. Precipitation and deformation microstructures were characterized using a JEM-2100F TEM equipped with a selected area electron diffraction (SAED) detector. TEM specimens were mechanically ground to a thickness of 40 μm and subsequently thinned by twin-jet electropolishing in a 10% perchloric acid–methanol solution at –30 °C. Precipitate sizes were determined using high-resolution FE-SEM/TEM, with the average size calculated from measurements of more than 200 individual precipitates. Precipitate microstructures were characterized by atom probe tomography (APT) using a local electrode atom probe (LEAP 5000 XR). Needle-shaped specimens were prepared via site-specific lift-out and annular milling using a FEI Scios focused ion beam/scanning electron microscope (FIB/SEM). APT analyses were conducted in voltage mode at a specimen temperature of 50 K, with a pulse repetition rate of 200 kHz, a pulse fraction of 0.2, and an ion collection rate of 0.5%

ions per field evaporation pulse. Three-dimensional reconstructions and compositional analyses were performed using Imago Visualization and Analysis Software (IVAS), version 3.8. SANS experiments were conducted at the China Spallation Neutron Source to investigate the size and distribution of nano-rod structures. A circular aperture with a diameter of 6 mm was used, and the sample-to-detector distance was set to 4 m. Scattering profiles were recorded as *I(q)* versus *q*, where $q = 4\pi \sin\theta / \lambda$, with θ being half of the scattering angle and λ the wavelength of the incident neutrons [72]. The accessible *q* range was approximately 0.0044 to 0.21 $Å^{-1}$. Experimental SANS data was analyzed and fitted using SasView 5.0 software [73].

3.3 Mechanical properties testing

For the first research, Dog-bone-shaped flat specimens with a gauge length of 12.5 mm and a cross-sectional area of 3 × 1 mm^2 were prepared using wire electrical discharge machining and carefully ground to 7000 grits using SiC paper. Uniaxial tensile tests were performed on a Material Testing System (MTS) machine at room temperature at a strain rate of 10^{-3} s^{-1}. Yield strength was determined with the 0.2% offset plastic strain method. Fracture surfaces were examined by SEM.

For the second and third research, Dog-bone-shaped flat specimens with a gauge length of 12.5 mm and a cross-sectional area of 3 × 0.65 mm^2 were prepared using wire electrical discharge machining and subsequently ground with SiC papers up to 7000 grit to achieve a smooth surface finish. Uniaxial tensile tests were performed at room temperature on a Material Testing System (MTS) machine at a constant strain rate of 10^{-3} s^{-1}. Yield strength was determined using the 0.2% offset method. For each condition, at least three tensile specimens were tested to ensure statistically reliable results.

Hardness measurements were conducted using a Future-Tech microhardness tester under a 1 kN applied load and a dwell time of 15 seconds. The average hardness was calculated from ten individual measurements.

3.4 Computational calculations

Thermodynamic calculations based on the CALPHAD method were employed to supplement and corroborate the experimental results in this study. By specifying variables such as temperature, pressure, and chemical composition, the phase constitution and transformations of the M/HEAs could be evaluated. In this thesis, equilibrium phase diagrams were assessed using Thermo-Calc 3.0.1 software with the Ni-based (TTNI8) database. The calculated results exhibited good agreement with the experimental findings.

First-principles calculations were performed with spin polarization by using the Vienna *ab initio* simulation package (VASP) within the generalized gradient approximation (GGA) by Perdew–Burke–Ernzerhof (PBE) for the exchange-correlation functional [74-78]. A cutoff energy of 400 eV and a 5 × 5 × 5 k-point mesh were used in the calculations. The atomic positions and volumes of supercells were optimized until the Hellmann-Feynman force was smaller than 0.02 eV $Å^{-1}$. The convergence criteria of self-consistent calculations was 10^{-5} eV.

Chapter 4 Achieving ultrahigh strength and ductility in HEAs via dual precipitation

4.1 Introduction

The continuous innovation of advanced structural materials is crucial to promoting technological progress and sustainable development of society, and a wide variety of industrial applications require materials with high strength and ductility. However, improving the strength of materials usually results in a decrease in ductility, which is known as the strength-ductility trade-off [1, 2]. Face-centered cubic (FCC) HEAs have spanned a wide range of scientific interest due to their excellent toughness and ductility at both ambient and cryogenic temperatures [3, 10, 12, 55]. However, a single-phase FCC structure generally results in a low yield strength, which is insufficient for many practical applications. As such, extensive efforts have been devoted to improving the strength of FCC HEAs through various strengthening methods, including solid solution strengthening, grain size refinement, strain hardening, and precipitation strengthening.

Precipitation strengthening has been proven an effective method to strengthen HEAs at both room and elevated temperatures. The degree of strengthening is dependent on the precipitate microstructure and the dislocation interaction with precipitates. From the dislocation interaction point of view, precipitates can be classified into sheared and bypassed precipitates. Coherent $L1_2$ nanoparticles are a classical type of shearable precipitate in FCC alloys and have been widely used in 3d transition-metal HEAs [18-20, 79]. For example, He *et al.* [22] added 2 at.% Al and 4 at.% Ti to a FeCoNiCr alloy, which results in the formation of coherent $L1_2$-Ni_3(Al, Ti) nanoparticles in the FCC matrix, improving the yield strength to more than 1000 MPa

at room temperature. Yang *et al.* [19] developed a $(FeCoNi)_{86}Al_7Ti_7$ alloy with a high density of $L1_2$ nanoparticles, which exhibits a yield strength of 1000 MPa and an excellent ductility of ~ 50%. Yang *et al.* [80] designed high-content $L1_2$-Ni_3(Al, Nb) nanoparticles in a CoCrNi matrix by adding Al and Nb additions, achieving a yield strength of 1150 MPa. In these alloys, the $L1_2$ nanoparticles can precipitate on a sufficiently fine scale in the FCC matrix with a uniform distribution. Because of their coherency with the FCC matrix and fine sizes, the $L1_2$ nanoparticles are typically sheared by moving dislocations. The precipitation shearing mechanism can strengthen alloys without causing a significant reduction in ductility, but the strengthening response is typically moderate; that is, the yield strength of most $L1_2$ nanoparticle-strengthened HEAs is less than 1200 MPa. For achieving an ultrahigh strength through single $L1_2$ precipitation strengthening, the fabrication of these HEAs usually requires a complicated processing involving server plastic deformation, which might limit their potential applications in some fields. Moreover, ultrahigh-strength HEAs strengthened by single $L1_2$ precipitates usually have a low work hardening rate at the early stage of plastic deformation due to the lack of strong dislocation interactions [81]. On the other hand, some hard precipitates, such as σ, μ, and Laves phases, are also used for strengthening FCC-HEAs. For instance, Liu *et al.* [16] developed $FeCoNiCrMo_x$ alloys strengthened by σ and μ phases. The two types of hard phases provide a very effective strengthening, making the materials reach a strength of 1187 MPa and a ductility of 19%. Sunkari *et al*. [82] designed $CoCrFeNi_{2.1}Nb_x$ eutectic HEAs composed of a ductile FCC matrix and hard Laves phases with a fine-layered structure, which exhibit a yield strength of 1219 MPa. Sunkari *et al.* [83] reported that a high volume fraction of Laves precipitates significantly elevates the strength of an alloy to 1680 MPa, which is accompanied by a rapid decrease in ductility to 3%. The introduction of hard Laves

precipitates to HEAs can provide additional hardening through the Orowan bypass mechanism, the fabrication of which can be done through conventional aging treatments without requiring complicated processing. Furthermore, Laves precipitates are strong barriers for dislocation motion, which can provide a high work hardening rate in the early stages of deformation, having the potential to avoid the formation of Luders bands. It should be pointed out that although bypassed precipitates can drastically increase the yield strength of HEAs, excessive amounts of these phases can lead to a significant decrease in ductility due to the brittle nature of the hard precipitates.

In view of the advantages and limitations of sheared and bypassed precipitates, it is interesting to design advanced HEAs with dual precipitation of the two types of precipitates. It is hoped to maximize the advantages of the two types of precipitates while minimizing their disadvantages, thereby achieving superior mechanical properties. The aim of this study is not to replace the $L1_2$ strengthening with the Laves strengthening but rather to combine the two strengthening mechanisms together for achieving balanced properties. It is worth pointing out that the dual precipitation in multicomponent HEAs is extremely complicated, which involves complex elemental partitioning and solute interactions. Currently, there is a lack of systematic investigations on the precipitation and mechanical behaviors of dual-precipitation-strengthened HEAs. The purpose of this chapter is to quantitatively understand the dual precipitation behavior of HEAs and correlate their precipitate microstructure with bulk mechanical properties. Specifically, $(Ni_2Co_2FeCr)_{96-x}Al_4Nb_x$ alloys strengthened by the dual precipitation of $L1_2$ and Laves phases were selected as a model for this study, and their precipitate microstructure, mechanical properties, and deformation behavior were thoroughly investigated through a combination of 3D-APT, TEM, first-principles calculations, and mechanical tests. Special attention was paid to the underlying

mechanisms that control the precipitation, strengthening, and deformation of dual-precipitation-strengthened HEAs.

4.2 Thermodynamics-aided alloy design

Thermodynamic calculations have been proved to be a powerful tool for a quantitative prediction of phase equilibria and transformations in multi-component systems, the results of which can serve as a guide for the alloy design of dual-precipitation-strengthened HEAs. Fe–Co–Ni–Cr is an extensively studied FCC HEA system because of its excellent toughness and ductility. Al is an essential $L1_2$ forming element in the Fe–Co–Ni–Cr system, whereas Nb can partition to both $L1_2$ and Laves phases [84, 85]. The precipitation of $L1_2$ and Laves phases consumes a large amount of both Ni and Co [86], and thus, we choose $(Ni_2Co_2FeCr)_{96-x}Al_4Nb_x$ as a model system. Mignanelli *et al.* [87] showed that Nb-containing $L1_2$ precipitates remain stable and maintain a high volume fraction after a long-term exposure at 700 °C. Stein *et al.* [88] found that the Nb-containing Laves phase has good thermal stability at 700 °C. Hence, we used 700 °C as the aging temperature in this study. The Thermo-Calc software together with the TTNI8 database was used to assess the effect of Nb addition on the phase relations of the $(Ni_2Co_2FeCr)_{96-x}Al_4Nb_x$ system. Figure 4.1 shows the calculated pseudo-binary $(Ni_2Co_2FeCr)_{96-x}Al_4Nb_x$ phase diagram. When the Nb content is less than 3 at.%, the alloys are in the FCC + $L1_2$ dual-phase region. When the Nb content increases to 3–7 at.%, the alloys enter the FCC + $L1_2$ + Laves triple-phase region, which meets our design criteria for the dual precipitation of $L1_2$ and Laves phases. Further increasing the Nb content results in the formation of δ phases, which have a composition of Ni_3Nb, similar to that of the $L1_2$ phase. The formation of δ phase consumes both Ni and Nb, thus inhibiting the $L1_2$ formation. Based on the above considerations, 3 alloys

with the compositions of $(Ni_2Co_2FeCr)_{96-x}Al_4Nb_x$ (x = 3, 5, and 7 at.%) were chosen as representative materials for experimental investigations. The reason for selecting these three compositions is that 3 at.% Nb represents the critical value for Laves phase precipitation, 5 at.% Nb may achieve the optimal balance between strength and plasticity, while 7 at.% Nb demonstrates the upper limit before embrittlement, clearly illustrating the dialectical relationship between performance trade-offs and synergistic effects in dual-phase precipitation design.

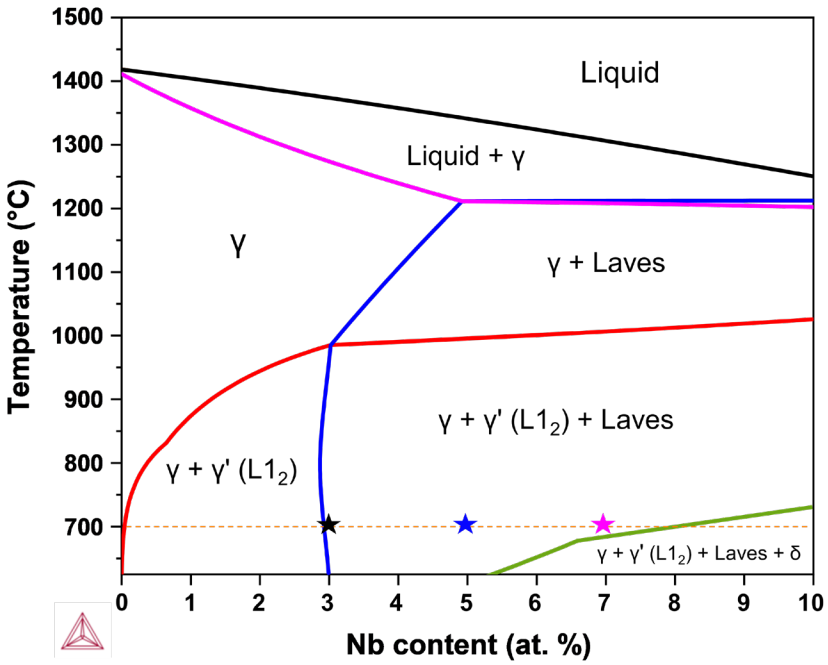

Fig. 4.1. Calculated phase diagram of the $(Ni_2Co_2FeCr)_{96-x}Al_4Nb_x$ system.

4.3 Results

4.3.1. Mechanical properties

The optimum condition for age hardening of the $(Ni_2Co_2FeCr)_{96-x}Al_4Nb_x$ alloys was determined by microhardness tests. Microhardness values of the alloys with

different Nb contents are shown in Fig. 4.2 as a function of aging time. It is evident that the age-hardening response increases with increasing Nb content. For all alloys, the microhardness generally reaches a peak after aging for 24 h and then decreases gradually due to an over-aging effect, suggesting that the aging for 24 h is an optimum condition for age hardening of the alloys. Room-temperature tensile tests were performed to further investigate the effect of Nb on the mechanical properties of the $(Ni_2Co_2FeCr)_{96-x}Al_4Nb_x$ alloys in the 24-h aged condition.

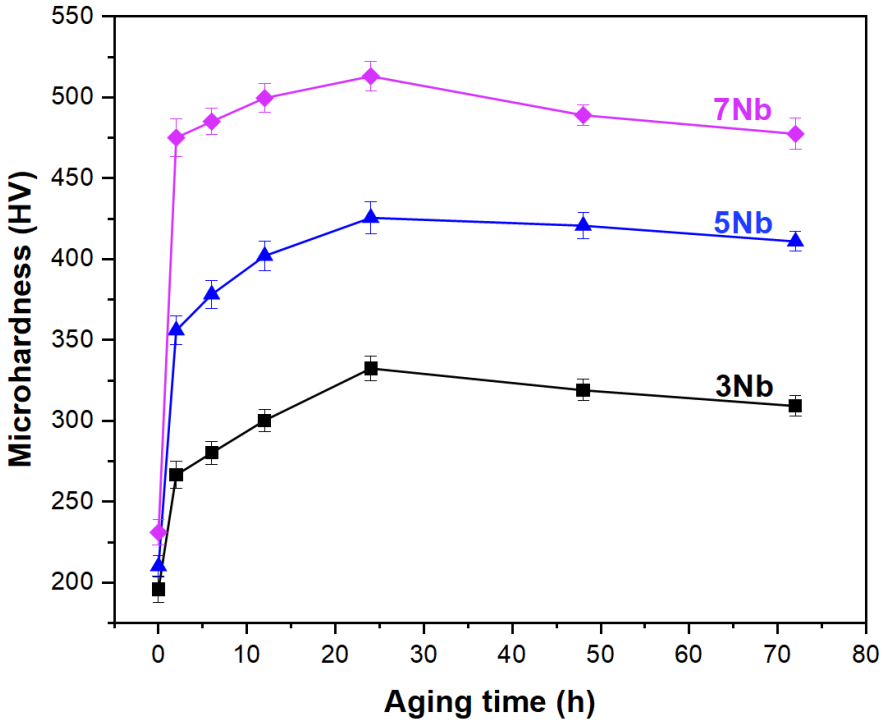

Fig. 4.2. Vickers microhardness of the 3Nb, 5Nb, and 7Nb alloys as a function of aging time at 700 °C.

Figure 4.3 displays the representative engineering stress–strain curves of the alloys with different Nb contents, and their yield strength, ultimate tensile strength, and total and uniform elongations are summarized in Table 4.1. The work hardening rate and true stress–strain curves of these alloys are displayed in Fig. 4.4 The 3Nb alloy exhibits a yield strength of 950 ± 12 MPa, an ultimate tensile strength of 1350 ± 16 MPa, and a

total elongation of 33% ± 3%; such mechanical properties are similar to those of $L1_2$-strengthened HEAs in the literature [19]. When the Nb content increases to 4 at.%, both the yield strength and ultimate tensile strength show a slight increment of approximately 150 MPa. As for the 5Nb alloy, the yield strength and ultimate tensile strength increase drastically to 1401 ± 11 and 1804 ± 15 MPa, respectively. Noticeably, this alloy is still very ductile, exhibiting a uniform elongation of 18% ± 2% and a total elongation of 21% ± 2%. As the Nb content further increases to 6 and 7 at.%, the yield strength increases to 1545 and 1630 MPa, respectively, but at the expense of a significant decrease in ductility; their total elongation decreases to 10% ± 2% and 6% ± 4%, respectively.

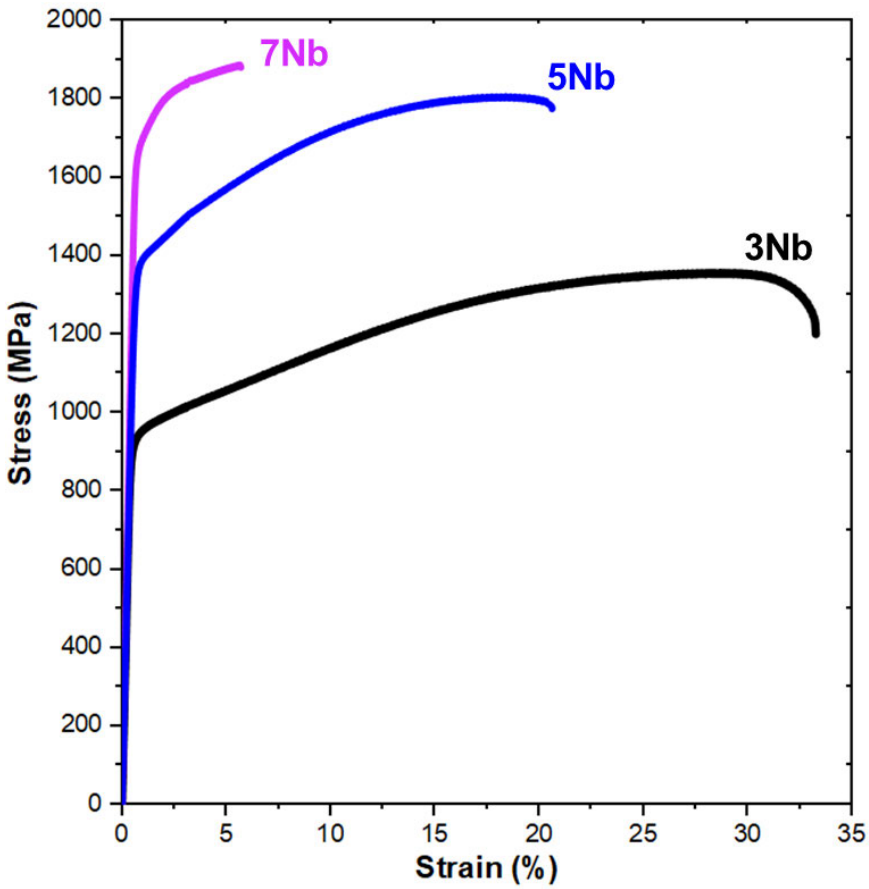

Fig. 4.3. Tensile engineering stress–strain curves of the 3Nb, 5Nb, and 7Nb alloys after aging for 24 h at 700 °C.

Table 4.1. Yield strength (YS), ultimate tensile strength (UTS), total elongation (TE), and uniform elongation (UE) of the alloys after aging for 24 h at 700 ℃.

Alloy	YS (MPa)	UTS (MPa)	TE (%)	UE (%)
3Nb	950 ± 12	1350 ± 16	33 ± 3	28 ± 3
5Nb	1401 ± 11	1804 ± 15	21 ± 2	18 ± 2
7Nb	1630 ± 19	1886 ± 12	6 ± 4	6 ± 4

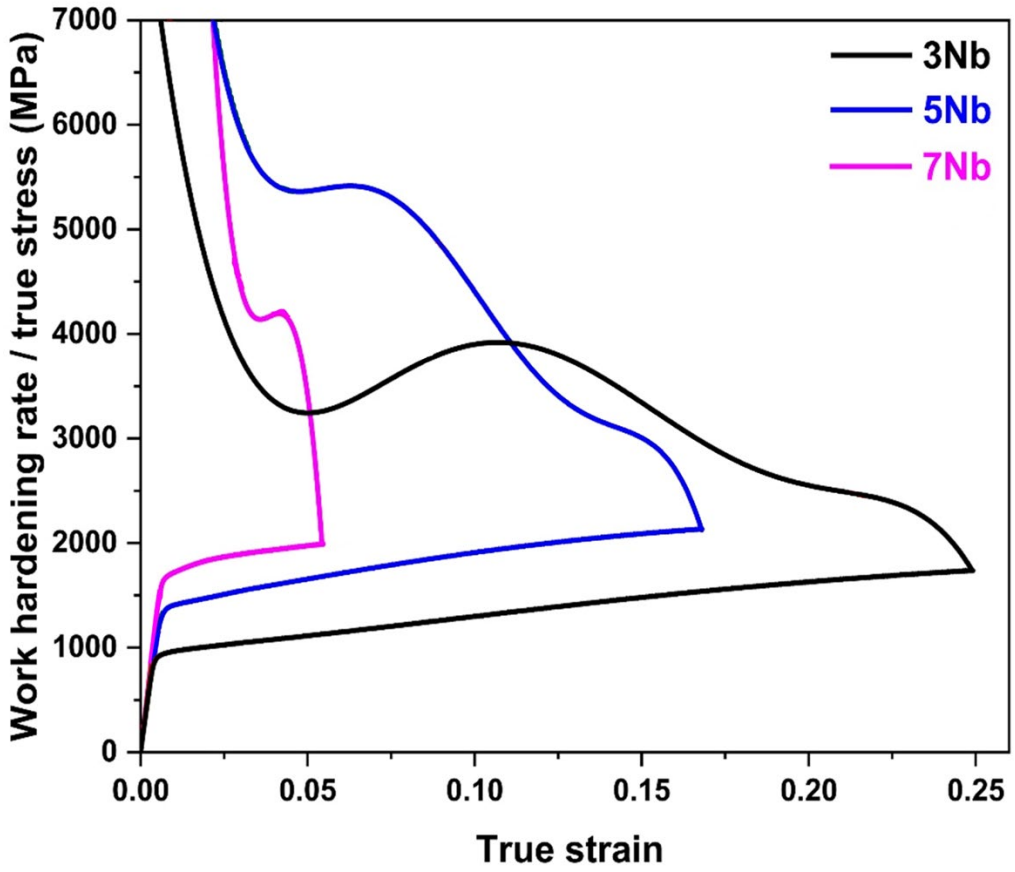

Fig. 4.4. Work hardening rate and true stress–strain curves of the 3–7Nb alloys.

From the work hardening rate curves, it is evident that the 4–7Nb alloys exhibit a higher work hardening rate than the 3Nb alloy at the early stage of plastic deformation. Fracture surfaces of the alloys with different Nb contents are displayed in Fig. 4.5 The fracture surface of the 3Nb alloy contains numerous dimples, indicating a characteristic

mode of a ductile fracture. As the Nb content increases to 5 at.%, the fracture surface shows fine dimples together with a considerable amount of cleavage facets. Further increasing the Nb content results in an increased area fraction of cleavage facets on the fracture surface.

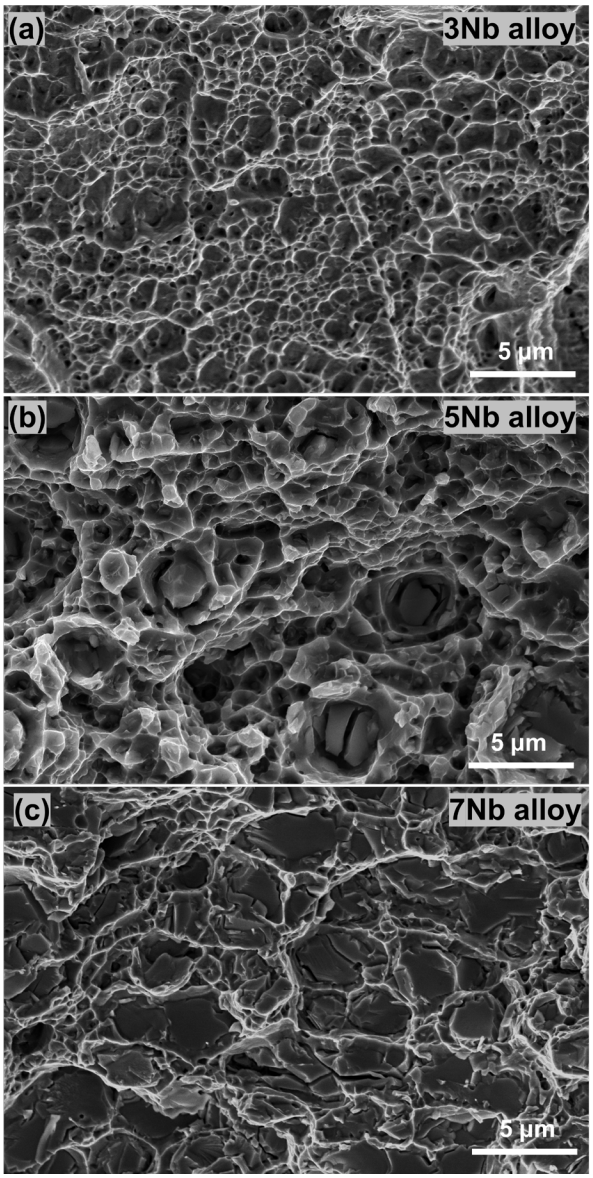

Fig. 4.5. Fracture surfaces of the (a) 3Nb, (b) 5Nb, and (c) 7Nb alloys.

From the above tensile results, it is apparent that the 5Nb alloy exhibits a good combination of an ultrahigh yield strength of more than 1400 MPa, an ultimate tensile strength of over 1800 MPa, and a total elongation of more than 20%. To demonstrate

the excellent mechanical properties of the 5Nb alloy, we compare it with various types of previously reported FCC-HEAs strengthened by a single type of precipitates, including $L1_2$-strengthened HEAs and Laves precipitates strengthened HEAs (Fig. 4.6) [22, 61, 79, 82, 83, 89-95]. The 5Nb alloy exhibits a doubled total elongation as compared with the Laves-strengthened HEAs while maintaining a comparable yield strength. When compared with the $L1_2$-strengthened HEAs, the 5Nb alloy shows a similar total elongation but a 50% increase in yield strength. The excellent combination of high yield strength and total elongation makes the presently developed 5Nb alloy as a promising candidate material for structural applications.

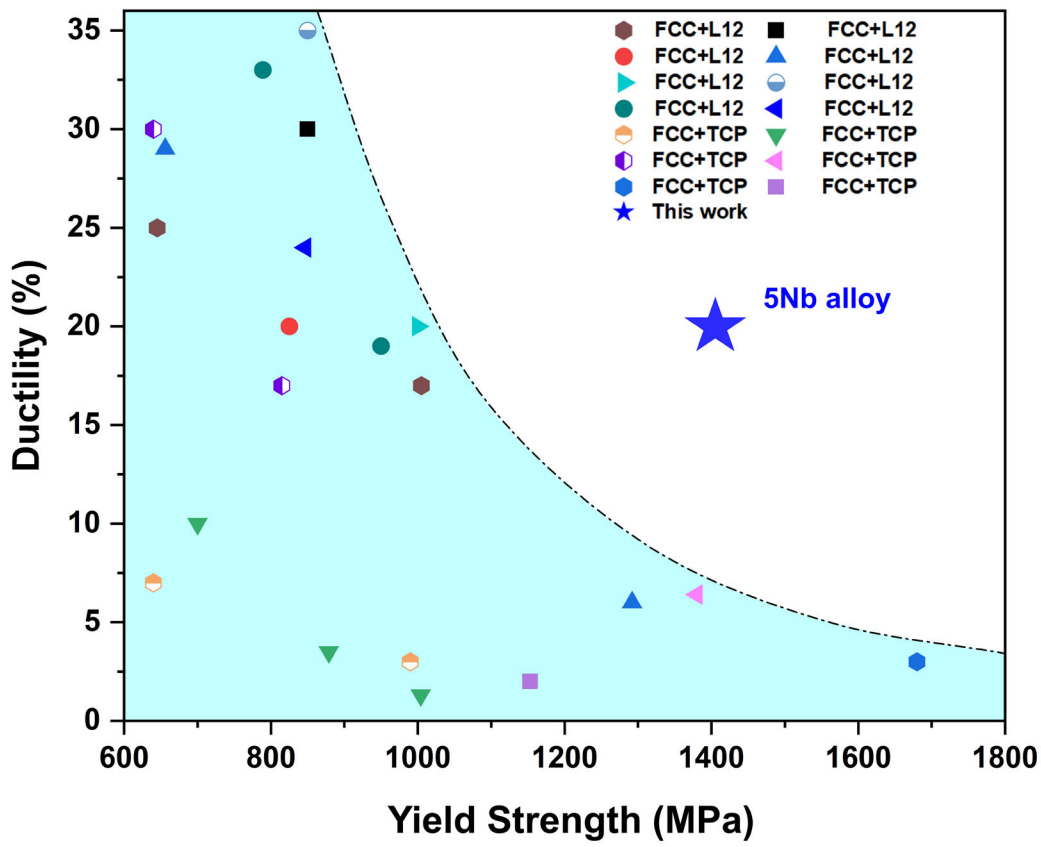

Fig. 4.6. Yield strength vs total elongation of the 5Nb alloy compared with various types of precipitation-strengthened HEAs.

4.3.2. Microstructure

The microstructure of the alloys with different Nb contents is shown in Fig. 4.7 The 3Nb alloy shows a recrystallized grain structure with an average grain size of 20 ± 3 μm, and spherical nanoparticles are uniformly distributed in the matrix. As the Nb content increases, the average grain size decreases gradually, reaching 3 ± 1 μm in the 7Nb alloy. Meanwhile, bright-contrasted block precipitates appear in 5 and 7 at.% Nb alloys, and their volume fraction increases from approximately 6% ± 3% in the 5Nb alloy to 16% ± 5% in the 7Nb alloy.

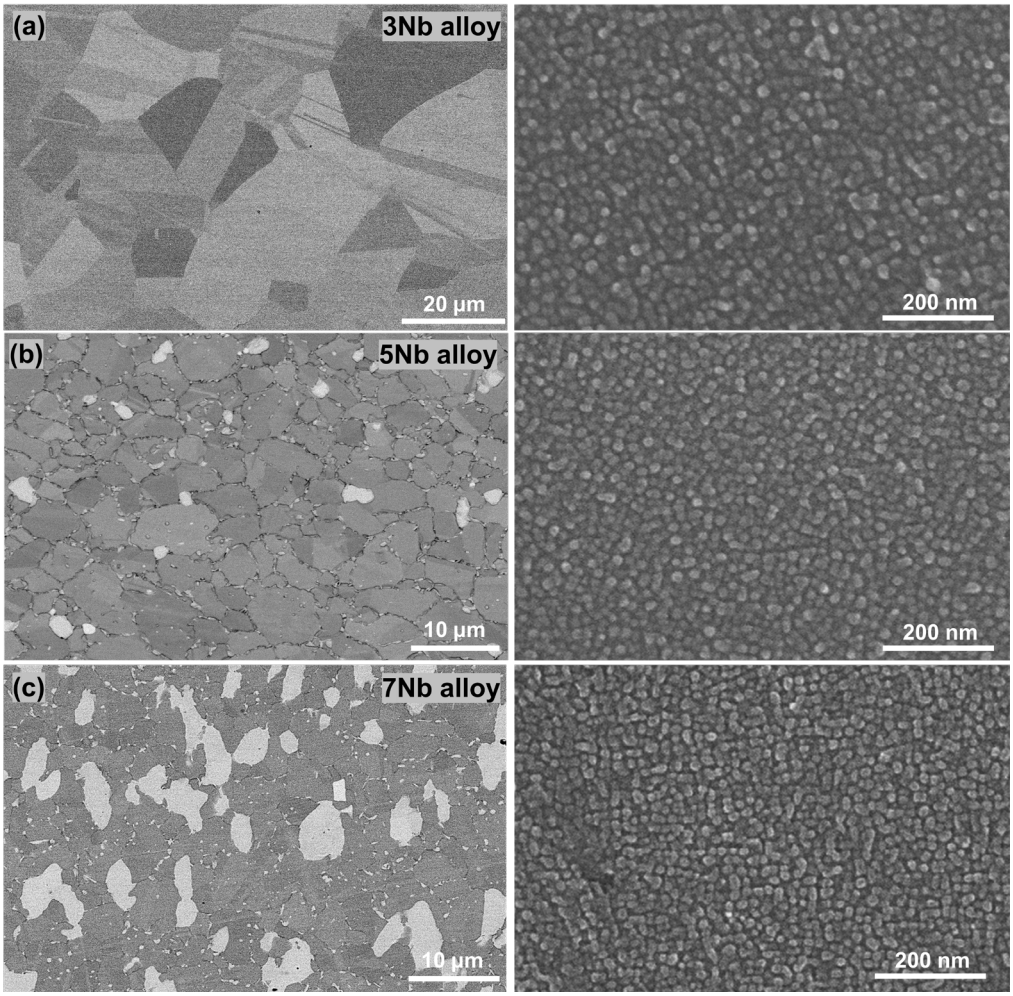

Fig. 4.7. SEM microstructures of the (a) 3Nb, (b) 5Nb, and (c) 7Nb alloys after aging for 24 h at 700 ℃.

Since the 5Nb alloy exhibits the best combination of high yield strength and total elongation, we systematically characterized the microstructure of this alloy by SEM, XRD, TEM, and EBSD. A representative SEM micrograph of the alloy is displayed in Fig. 4.7b. The alloy exhibits an equiaxed grain structure with an average grain size of approximately 5 μm. A high-resolution SEM image of the grain interior reveals that a high number density of spherical nanoparticles is uniformly distributed in the matrix. In addition, small amounts of bright-contrasted block-shaped phases are decorated at grain boundaries.

A representative dark-field TEM image and corresponding SAED pattern of the spherical nanoparticles are displayed in Fig. 4.8a, which reveal the uniform precipitation of $L1_2$ nanoprecipitates with an average size of 10.4 nm in the FCC matrix. A representative XRD pattern of the 5Nb alloy is presented in Fig. 4.8b. The alloy exhibits major peaks at 43° and 51°, which correspond respectively to the (111) and (200) planes of the FCC/$L1_2$ phases. The deconvolution of the (311) diffraction peak reveals that the lattice misfit between the two phases is approximately 0.252% (the inset of Fig. 4.8b). In addition, some small reflection peaks corresponding to the Laves phase appear at 38°, 41°, 44°, and 46°. Figure 4.8c presents an EDS spectrum of the block-shaped phase observed in Fig. 4.7b. The EDS result shows that these regions are enriched in Nb, Co, Cr, Fe, and Ni, and the atomic ratio of (Co + Cr + Fe + Ni):Nb is approximately 2:1. The EDS result, together with the XRD and SEM data, indicates that the bright-contrasted block-shaped phase is a $(Co, Cr, Fe, Ni)_2Nb$-type Laves phase. An EBSD inverse pole figure (IPF) map of the 5Nb alloy is illustrated in Fig. 4.8d, and the corresponding phase map is shown in Fig. 4.8e. Noted that due to the similar crystal structure of the FCC and $L1_2$ phases, EBSD cannot distinguish these two phases.

Therefore, the FCC and $L1_2$ phases are marked together in orange in Fig. 4.8e, whereas the Laves phase at grain boundaries is colored in blue. The volume fraction of the Laves phase was determined to be approximately 6%.

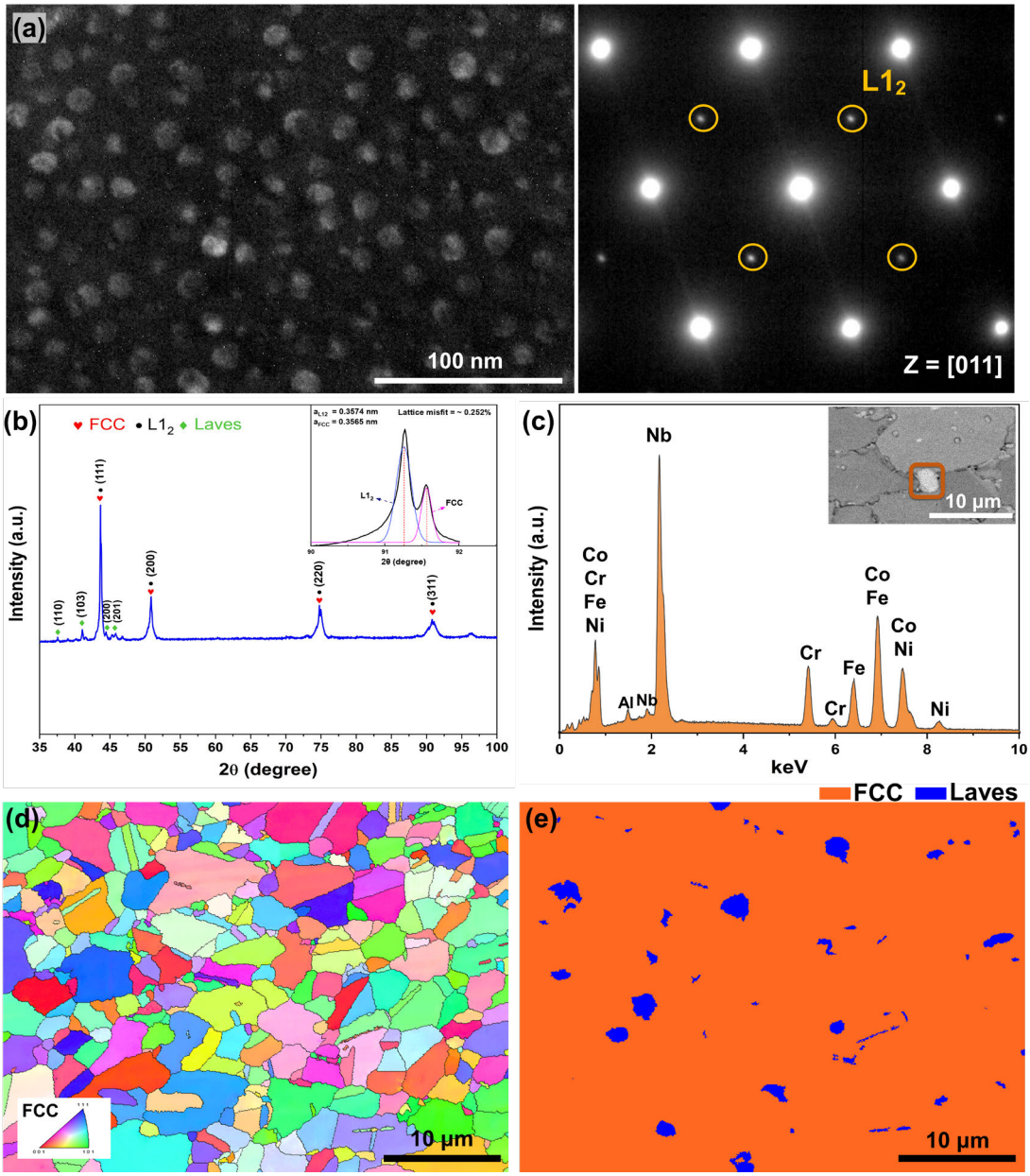

Fig. 4.8. Microstructures of the 5Nb alloy after aging for 24 h at 700 ℃: (a) Dark-field TEM image and SAED pattern, (b) XRD patterns, (c) EDS spectrum for the region with the bright contrast in the inset, and (d) and (e) are EBSD IPF and phase maps, respectively. The inset of (b) is the deconvolution of the (311) diffraction peak.

4.3.3. Nanoscale precipitation

The precipitate composition of $L1_2$ nanoparticles in the 5Nb alloy was further characterized by 3D-APT. The atom maps of Ni, Co, Fe, Cr, Al, and Nb are displayed in Fig. 4.9a. It is evident that Ni, Al, and Nb partition to the $L1_2$ nanoprecipitates and Co, Fe, and Cr partition to the FCC matrix. The 40 at.% Ni iso-concentration surfaces were used to delineate the $L1_2$ nanoparticles. The proximity histogram of the nanoparticles is displayed in Fig. 4.9b, and the compositions of the nanoparticles and matrix obtained from the flat region of the proximate histogram are summarized in Table 4.2.

It can be seen that the nanoparticles contain approximately 59.4 ± 0.5 at.% Ni, 15.2 ± 0.2 at.% Co, 15. 6 ± 0.1 at.% Al, and 8.1 ± 0.1 at.% Nb, together with a small amount of Fe (2.81 ± 0.4 at.%) and Cr (1.07 ± 0.3 at.%). The atomic ratio of (Ni + Co):(Al + Nb) is approximately 3:1, suggesting the formation of $(Ni, Co)_3(Al, Nb)$-type $L1_2$ nanoparticles. The matrix composition can be regarded as 20.6Ni–33.4Co–22.1Fe–20.7Cr–2.2Al–1.1Nb (at.%). Based on the precipitate and matrix compositions, the volume fraction of the $L1_2$ phase was evaluated by using the lever rule, as shown in the inset of Fig. 4.9b. The volume fraction of the $L1_2$-type precipitates was calculated to be 27%. The partitioning ratio of Nb, k_{Nb}, defined as the concentration of Nb in the $L1_2$ phase divided by its concentration in the FCC phase, was calculated to be approximately 7.4, suggesting a strong partitioning to the $L1_2$ precipitates with respect to the FCC matrix.

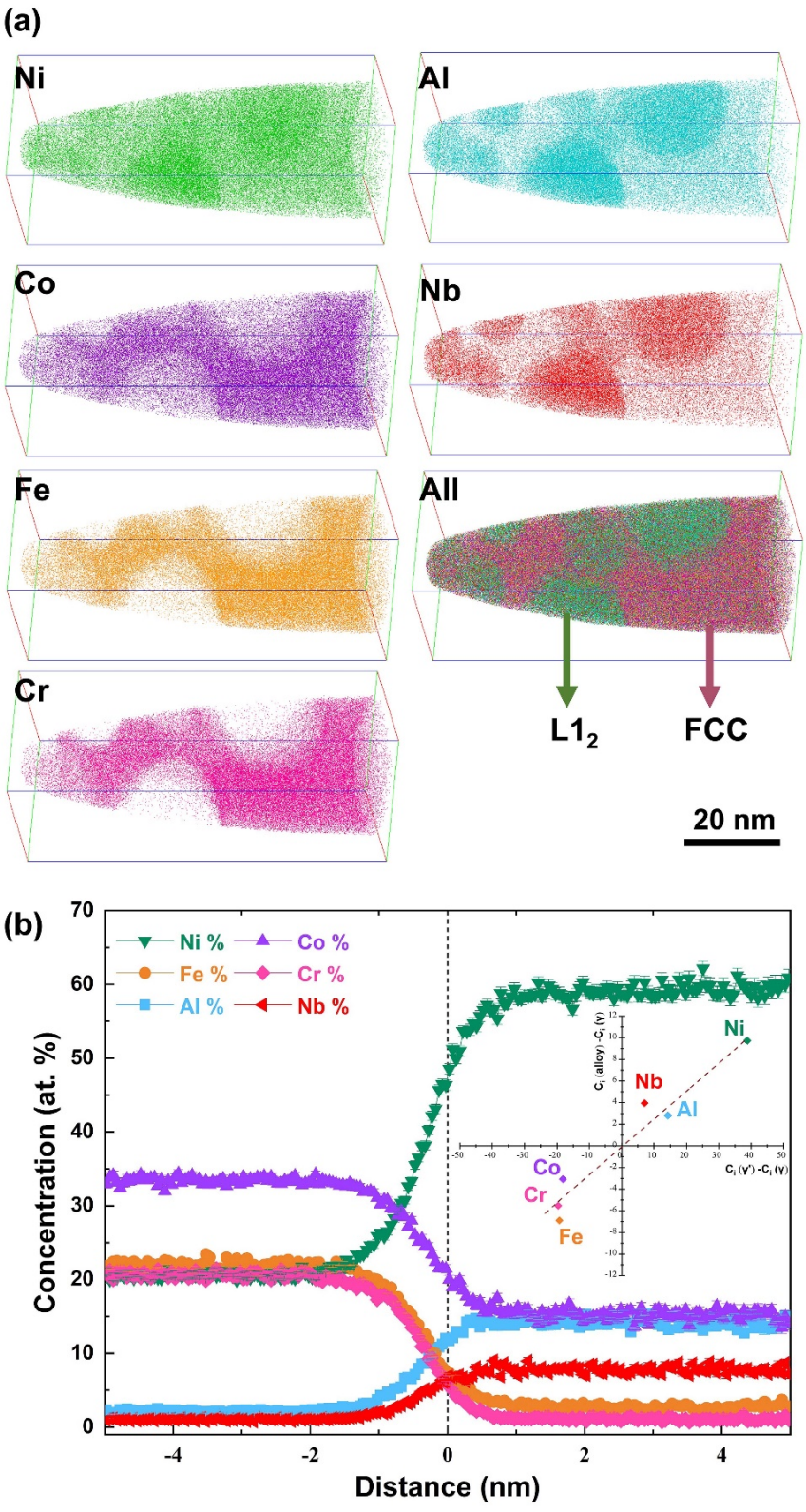

Fig. 4.9. APT characterization of the 5Nb alloy after aging for 24 h at 700 °C: (a) atom maps and (b) proximity histogram concentration profiles. The inset of (b) is the calculation of the volume fraction of the $L1_2$ phase using the lever rule.

Table 4.2. Matrix and precipitate compositions of the 5Nb HEA in the 24-aged condition determined by APT (at.%).

	Ni	Co	Fe	Cr	Al	Nb
Matrix	20.6 ± 1.1	33.4 ± 0.8	22.1 ± 0.3	20.7 ± 0.2	2.2 ± 0.1	1.1 ± 0.2
Precipitate	59.4 ± 0.5	15.2 ± 0.2	2.8 ± 0.4	1.1 ± 0.3	15.6 ± 0.1	8.1 ± 0.1

4.3.4. First-principles calculation

To understand the atomistic mechanism of the preferential partitioning of Nb to the $L1_2$ phase, we performed first-principles calculations to study the substitutional energy of Nb in the $L1_2$ and FCC phases. We constructed a 108-atom supercell, which consists of a 14-atom $L1_2$-$(Ni_{0.5}Co_{0.5})_3Al$ lattice and a 94-atom FCC lattice. The compositions of the $L1_2$ and FCC lattices were based on the $L1_2$ and FCC compositions determined by APT. The supercell models of the $L1_2$-$(Ni_{0.5}Co_{0.5})_3Al$ and FCC structures are shown in Fig. 4.10a. When Nb is in the $L1_2$-$(Ni_{0.5}Co_{0.5})_3Al$ lattice, the formation energy, $\Delta E_{Nb\_in\_L12}$, can be given by:

$$\Delta E_{Nb\_in\_L1_2} = E_{L1_2} - 34E_{Co} - 20E_{Cr} - E_{Nb} - 21E_{Fe} - 24E_{Ni} - 8E_{Al}. \quad (4.1)$$

where E_{L12} is the total energy of the supercells with Nb in the $L1_2$-$(Ni_{0.5}Co_{0.5})_3Al$ lattice, and E_{Co}, E_{Cr}, E_{Nb}, E_{Fe}, E_{Ni}, and E_{Al} are the potential of Co, Cr, Nb, Fe, Ni, and Al, respectively. The coefficients represent the number of atoms in the supercell. Similarly, when Nb is in the FCC lattice, the corresponding formation energy, $\Delta E_{Nb\_in\_FCC}$, is described as:

$$\Delta E_{Nb\_in\_FCC} = E_{FCC} - 34E_{Co} - 20E_{Cr} - E_{Nb} - 21E_{Fe} - 24E_{Ni} - 8E_{Al} \quad (4.2)$$

where E_{FCC} is the total energy of the supercells with Nb in the FCC lattice. Based on the formation energies obtained from Eqs. 4.1 and 4.2, the substitution energy, $E_{substitutional}$, can be expressed by:

$$E_{substitutional} = \Delta E_{Nb\_in\_L1_2} - \Delta E_{Nb\_in\_FCC} \quad (4.3)$$

The substitution energy of Nb was calculated to be –0.699 eV; this negative value indicates that Nb prefers to partition to the $L1_2$ phase (Fig. 4.10b). To further understand the chemical bonding of Nb in the FCC and $L1_2$ phases, the electron localization function (ELF) of the two phases was calculated, and the results are shown in Fig. 4.10c.

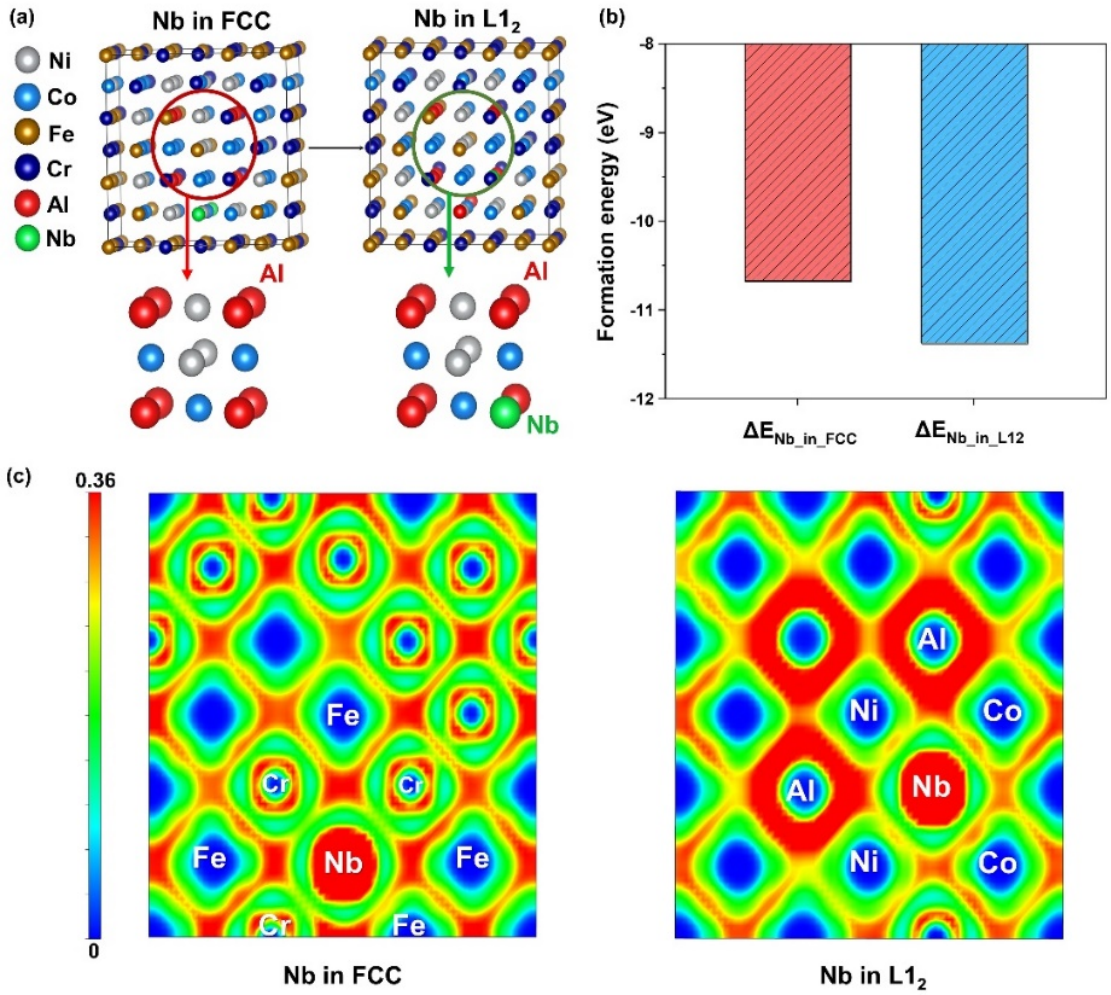

Fig. 4.10. First-principles calculations: (a) supercell models, (b) calculated formation energies, and (c) ELF maps of the structures with Nb in the FCC and $L1_2$ lattices.

It is evident that the ELF intensities around Nb in the $L1_2$ lattice are higher than those in the FCC lattice. The electrons around Nb appear localized in the $L1_2$ lattice, suggesting a strong bonding interaction of Nb in the $L1_2$ structure. In addition, we also calculated the Bader charges of Nb in the FCC and $L1_2$ structures to analyze the charge transfer. The Bader charge of Nb was calculated to be –0.82 in the FCC structure and –1.06 in the $L1_2$ structure. The negative value means that Nb loses electrons in both the $L1_2$ and FCC structures. The more negative value in the $L1_2$ structure indicates that more electrons transfer from Nb to its surrounding neighbors, which contributes to the stability of the $L1_2$ phase. Therefore, the first-principles calculation results prove that Nb has a promoting effect on the $L1_2$ precipitation.

4.4 Discussion

4.4.1. Strengthening mechanism

The effect of Nb on the strengthening of the dual-precipitation-strengthened HEAs can be ascribed to the four strengthening mechanisms: solid solution strengthening ($\Delta\sigma_s$), grain boundary strengthening ($\Delta\sigma_g$), and precipitation strengthening ($\Delta\sigma_p$) from the $L1_2$ and Laves precipitates. The yield strength of the 5Nb alloy (σ_y) can be expressed by the following equation:

$$\sigma_y = \sigma_0 + \Delta\sigma_s + \Delta\sigma_g + \Delta\sigma_p \tag{4.4}$$

where σ_0 = 390 MPa is the yield strength of the base alloy (0Nb) in the as-quenched condition, which was measured by experiments.

Since there is no conventional separation of solvent and solute in HEAs, it is difficult to assess the strengthening effect of solute atoms. Following the commonly used approach [22, 96], we approximate the overall 0Nb composition as the composite solvent and take Nb as the solute, such that the traditional solid solution strengthening model can be applied, which is expressed by [97]:

$$\Delta\sigma_s = M \cdot \frac{G_m \cdot \varepsilon_s^{3/2} \cdot c^{1/2}}{700} \tag{4.5}$$

where M = 3.06 is the Taylor factor, G_m = 81 GPa is the shear modulus of the matrix, ε_s represents the atomic size mismatch, and c is the atomic fraction of Nb in the FCC matrix. The strength increment introduced by the solid solution strengthening of Nb was calculated to be approximately 53 MPa.

Grain boundaries are known to be strong barriers to hinder the movement of dislocations, thus providing grain boundary strengthening. According to the classical Hall–Petch relation, the strength increment by grain boundary strengthening can be calculated by:

$$\Delta\sigma_g = k_y(d_1^{-1/2} - d_2^{-1/2}) \tag{4.6}$$

where d_1 = 6 μm and d_2 = 24 μm are the average grain sizes of the 5Nb alloy in the aged condition and the 0Nb base alloy in the as-quenched state, respectively, and k_y = 677 MPa $\mu m^{1/2}$ is the coefficient of grain size strengthening borrowed from similar FCC-HEAs [98]. The contribution of grain boundary strengthening was calculated to be about 148 MPa.

Precipitates generally hinder the movement of dislocations by forcing them to shear weak obstacles or bypass (Orowan looping) strong obstacles [99, 100] depending on the precipitate size (inter-precipitate spacing). Typically, when the precipitates are

sufficiently small and coherent with the matrix, the precipitate shearing mechanism dominates; when the particle radius exceeds a certain critical value or their interface is incoherent with the matrix, the Orowan looping mechanism is operative [100]. Considering that the average size of $L1_2$ particles in the 5Nb alloy (10.4 nm) is smaller than the critical value (~20 nm) [101], the particle shearing mechanism is considered to be operative for $L1_2$ particles. The particle shearing mechanism is attributed mainly to coherency strengthening ($\Delta\sigma_{CS}$), modulus strengthening ($\Delta\sigma_{MS}$), and ordering strengthening ($\Delta\sigma_{OS}$). The equations for these contributions are expressed by [100, 102]:

$$\Delta\sigma_{CS} = M \cdot \alpha_{\varepsilon}(G \cdot \varepsilon)^{3/2}\left(\frac{rf}{0.5Gb}\right)^{1/2} \tag{4.7}$$

$$\Delta\sigma_{MS} = M \cdot 0.0055(\Delta G)^{3/2}\left(\frac{2f}{G}\right)^{1/2}\left(\frac{r}{b}\right)^{(3m/2)-1} \tag{4.8}$$

$$\Delta\sigma_{OS} = M \cdot 0.81\frac{\gamma_{APB}}{2b}\left(\frac{3\pi f}{8}\right)^{1/2} \tag{4.9}$$

where r = 5.2 nm is the precipitate radius, α_{ε} = 2.6 is the lattice constant of the FCC matrix, f = 27% is the volume fraction of the $L1_2$ precipitates (Fig. 4.9b), ΔG = 4 GPa is the difference in shear modulus between the matrix (G_m = 81 GPa) and $L1_2$ phase (G_p = 77 GPa) [103], γ_{APB} = 0.2 J/m^{-2} is the average value of anti-phase boundary energy of the $L1_2$ phases [104, 105], and ε is the matrix-precipitate misfit, which is defined as $\varepsilon \approx 2/3 \cdot (\Delta\alpha/\alpha)$ [106]. As suggested in Ref. [107], order strengthening generally occurs during the shearing process, whereas coherency and modulus strengthening are activated before the shearing. The larger value of $\Delta\sigma_{OS}$ and ($\Delta\sigma_{CS}$ + $\Delta\sigma_{MS}$) contribute to the $L1_2$ precipitation strengthening ($\Delta\sigma_{L12}$). In this study, the order strengthening (560 MPa) is larger than the sum of coherency and modulus strengthening (170 MPa). Thus, order strengthening appears to be operative in the $L1_2$ precipitation strengthening,

contributing 560 MPa to the yield strength. In addition, the microstructural results reveal that the 5Nb alloy contains about 6% Laves precipitates. In view of their large sizes, the Orowan bypass mechanism is considered to be operative [108]. The precipitation strengthening by Laves precipitates ($\Delta\sigma_{Laves}$) can be modeled by [99]:

$$\Delta\sigma_{Laves} = M \cdot \frac{0.4Gb}{\pi\lambda} \frac{\ln(2\bar{r}/b)}{\sqrt{1-\nu}} \tag{4.10}$$

where ν = 0.35 is the Poisson's ratio [109], $\bar{r} = \sqrt{2/3} \cdot r_{Laves}$ is the mean precipitate radius on the slip planes, where r_{Laves} is the radius of Laves precipitates (~750 nm), and λ_{p} is the equivalent interprecipitate spacing of the Laves precipitates [99]. The strength increment due to the Laves precipitates was calculated to be approximately 258 MPa. On the basis of the reasonable assumption that the contributions from the two types of precipitates are additive, the total precipitation strengthening, $\Delta\sigma_{\mathrm{p}}$, can be estimated using the superposition expression [110]:

$$\Delta\sigma_p^n = \sigma_{L1_2}^n + \sigma_{Laves}^n \tag{4.11}$$

where n = 1.4 is an exponent for a mixture of sheared and bypassed precipitates. Therefore, the precipitation strengthening by the $L1_2$ and Laves precipitates was estimated to be 690 MPa.

Figure 4.11 summarizes the calculated results of all the above contributions. The theoretical yield strength of the 5Nb alloy was calculated to be 1281 MPa, which is in reasonable agreement with the experimental value (1401 ± 11 MPa). It is noted that the high number densities of $L1_2$ nanoparticles make a major contribution to the strength of the 5Nb alloy, whereas the Laves phase plays a minor role in the strengthening. The collective strengthening contributions from the precipitation strengthening, grain size refinement, and solid solution strengthening pushes the yield strength of the alloy to more than 1400 MPa.

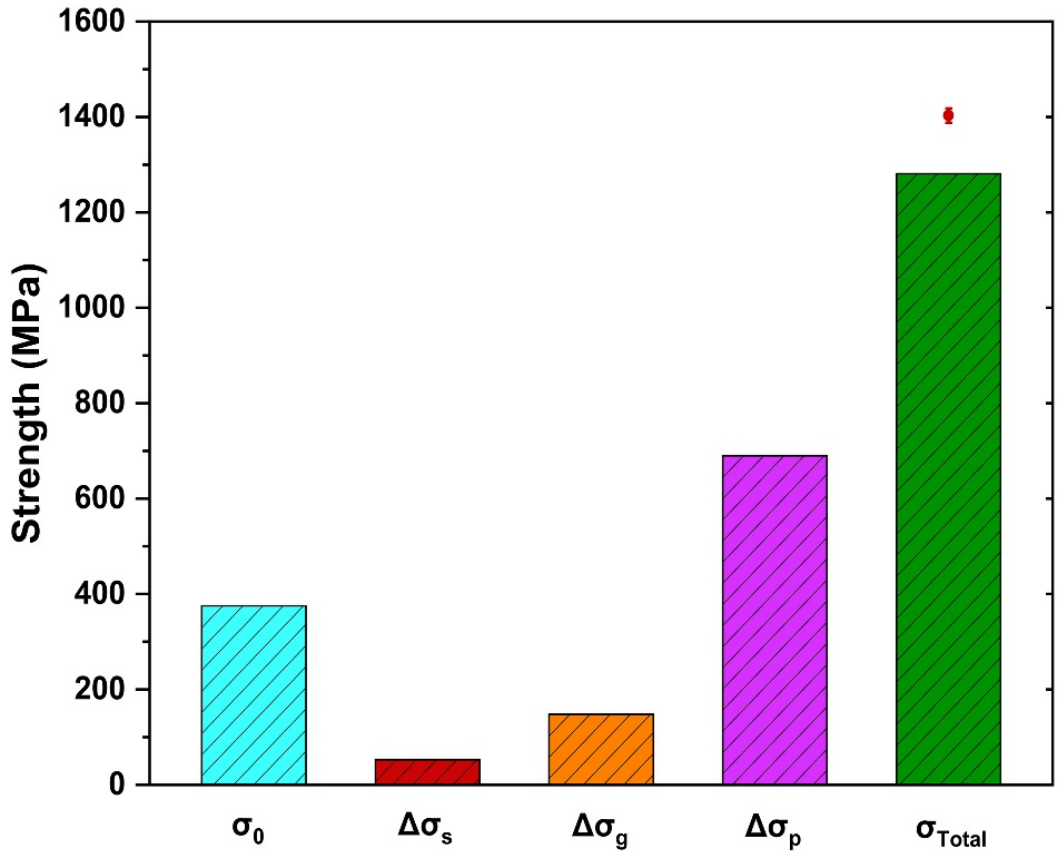

Fig. 4.11. Calculated contributions of solid solution strengthening ($\Delta\sigma_s$), grain boundary strengthening ($\Delta\sigma_g$), precipitation strengthening ($\Delta\sigma_p$) from the $L1_2$ and Laves precipitates, and total yield strength (σ_{Total}) of the 5Nb HEA in the 24-h aged condition. The red dot represents the experimental yield strength of the alloy.

4.4.2. Deformation mechanism

To understand the origins of the high ductility and excellent work-hardening behavior of the 5Nb alloy, the evolution of deformation microstructures was carefully investigated using TEM. Figure 4.12 exhibits the deformation microstructures of the 5Nb alloy under the 10% and 20% strains. In the 10% strain condition (Fig. 4.12a), parallel-aligned stacking faults (SFs, marked by blue arrows) along the (111) plane were clearly observed. As the strain increases to 20%, the dense and intersecting SFs

along different (111) planes (marked by blue and red arrows) are activated (Fig. 4.12b and Fig. 4.13a). An enlarged view of the 20%-strained sample is shown in Fig. 4.12c, which reveals that many intersecting SFs are distributed along two (111) glide planes. A clean version of Fig. 4.12c without any labeling is displayed in Fig. 4.13b. The fast Fourier transform (FFT) pattern of the intersected SFs is illustrated in Fig. 4.12d, and the stacking sequence of a representative SF is shown in Fig. 4.12e. It is evident that hierarchical SF networks are formed, in which the average spacing between adjacent SFs is approximately 15 nm. More intriguingly, the interaction of the two directions of SFs leads to the formation of V-type Lomer–Cottrell (LC) locks [111] on the non-slipping (100) planes (Fig. 4.12c). Figure 4.12f depicts the interaction of SFs with $L1_2$ nanoparticles, which reveals the shearing of $L1_2$ precipitates by moving SFs. In contrast, dislocations and SFs can not cut through the Laves precipitates due to their coarse sizes and hard nature, leading to the dislocation pile-ups (white arrows) at the interface between the Laves precipitates and FCC matrix (Fig. 4.12g).

On the basis of the above observations, the origins of the high ductility and work-hardening capability of the 5Nb alloy can be twofold. First, the formation of hierarchical SF networks in the system contributes to the enhancement of the work-hardening ability of the 5Nb alloy. The activation of extensive SFs should be attributed to the low SFE of the FCC matrix [95, 112]. For FCC-HEAs with a low SFE, the two ***a***/2 <110> perfect dislocations on different intersecting glide planes are dissociated into two ***a***/6 <112> Shockley partial dislocations. The APT results reveal that the FCC matrix has a composition of 20.6Ni–33.4Co–22.1Fe–20.7Cr–2.2Al–1.1Nb (at.%). We calculated the SF energy of the FCC matrix of the 5Nb alloy by using the empirical formula proposed by Xie *et al.* [113], which was estimated to be approximately 25 mJ/m^2. This value is in the range of 20–45 mJ/m^2, within which partial dislocations

separated with SF bonds are thermodynamically preferred, thereby making the activation of SFs easy under plastic deformation. Therefore, as the plastic deformation proceeds, the dislocations have a high tendency to dissociate into wide SFs, thereby triggering an SFs-dominated deformation mechanism, which hinders the cross-slip process. With the continuous activation of high densities of SFs in different directions, hierarchical SF networks emerge. This evolution is considered to be a dynamic Hall–Petch process [114, 115].

The high densities of hierarchical SF networks subdivide the grains into fine sub-grains under dynamic conditions during plastic deformation (Fig. 4.12c). This phenomenon can strongly confine the free paths of dislocation motion, thereby further enhancing the work-hardening capability. Second, the interaction between the two ***a***/6 <112> Shockley partial dislocations leads to the formation of V-type LC locks on the non-slipping (100) plane (Fig. 4.12c). Such immobile dislocation locks are additional obstacles to the motion of dislocations, thereby enhancing the work-hardening capability of the alloy. Wu *et al.* [116] reported that the LC locks can effectively pin dislocations and stabilize the SFs networks. When the SFs interact to form LC locks, twice the number of dislocation regions are pinned, thereby hindering the dislocation motion. In conclusion, the high density of nanoscale SFs networks and associated LC locks provide an efficient source of work-hardening capability for the 5Nb alloy, resulting in a prominent level of strength-ductility synergy.

The $L1_2$ and Laves precipitates also have an important impact on the plastic deformation and fracture behavior of the alloys. The $L1_2$ precipitates are sheared by moving SFs during plastic deformation. The precipitate shearing mechanism facilitates long-range dislocation gliding through the FCC/$L1_2$ microstructure, which is beneficial for the microscopic homogeneous plastic deformation of the materials. From the

deformation microstructure, we observed extensive SF interactions and high-density LC locks, which may serve as strong strain localized regions and initiate the formation of microvoids, thereby leading to the microvoid coalescence fracture mode with numerous fine dimples. In contrast, the Laves precipitates are coarse and hard phases that are bypassed by dislocations, leading to the dislocation pile-ups against the interface between the Laves precipitates and the FCC matrix. The dislocation pile-ups have two different effects on the deformation behavior. On the one hand, they can increase the work-hardening capability of the materials at the early stages of plastic deformation, but on the other hand, they could induce stress concentrations at the interface. In addition, the Laves phases are known to be brittle and tend to crack under tensile stress, leading to the formation of cleavage within the brittle Laves precipitates. Thus, the size and volume fraction of Laves precipitates should be controlled.

In this study, as the Nb content increases from 3 to 7 at.%, the volume fraction of Laves precipitates increases, which results in an increased area fraction of cleavage facets. As a result, we observed the change of fracture mode from the dimpled failure in the 3–4 at.% Nb alloys to a mixture of dimple and cleavage fracture in the 5–7 at.% Nb alloys. Furthermore, it is worth noting that the FCC matrix in HEAs usually has excellent damage tolerance, which can blunt cracks and/or retard the propagation of the cracks [16]. Therefore, the ductility reduction caused by Laves phases in FCC HEAs is usually not as server as that in conventional materials, such as steels and titanium alloys. Here we take advantage of the two types of strengthening precipitates and the ductile FCC matrix to optimize the mechanical properties of HEAs, thus achieving a balanced combination of high strength and tensile ductility.

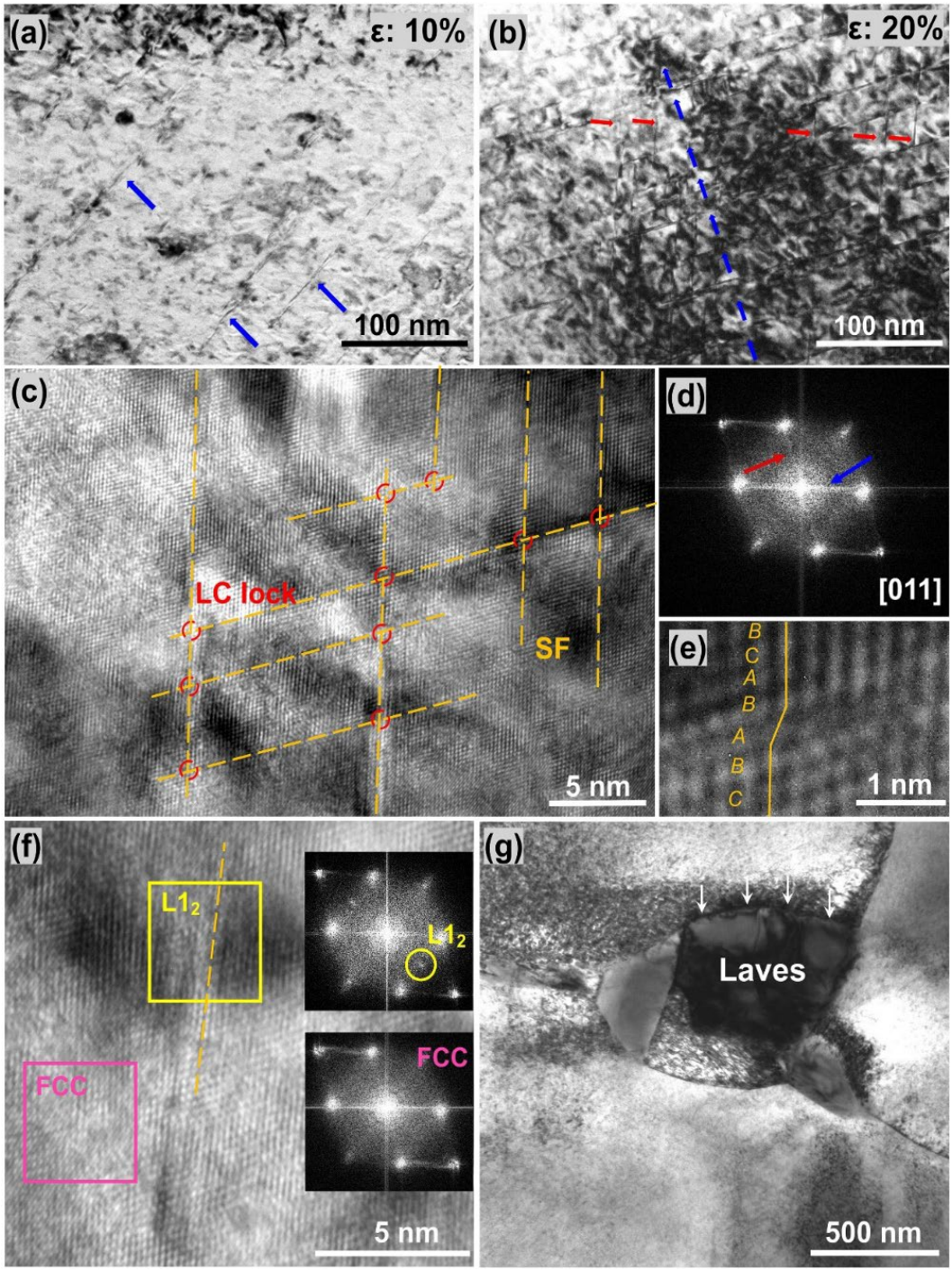

Fig. 4.12. Deformation microstructures of the 5Nb alloy: TEM images at the (a) 10% and (b) 20% tensile strains, (c) HRTEM image showing SFs in two directions and LC locks, (d) corresponding FFT image showing the intersecting SFs, (e) an enlarged view of a representative SF, (f) HR-TEM image showing the shearing of $L1_2$ precipitates by an SF and corresponding FFT patterns, and (g) TEM image showing the interaction of dislocations with Laves precipitates.

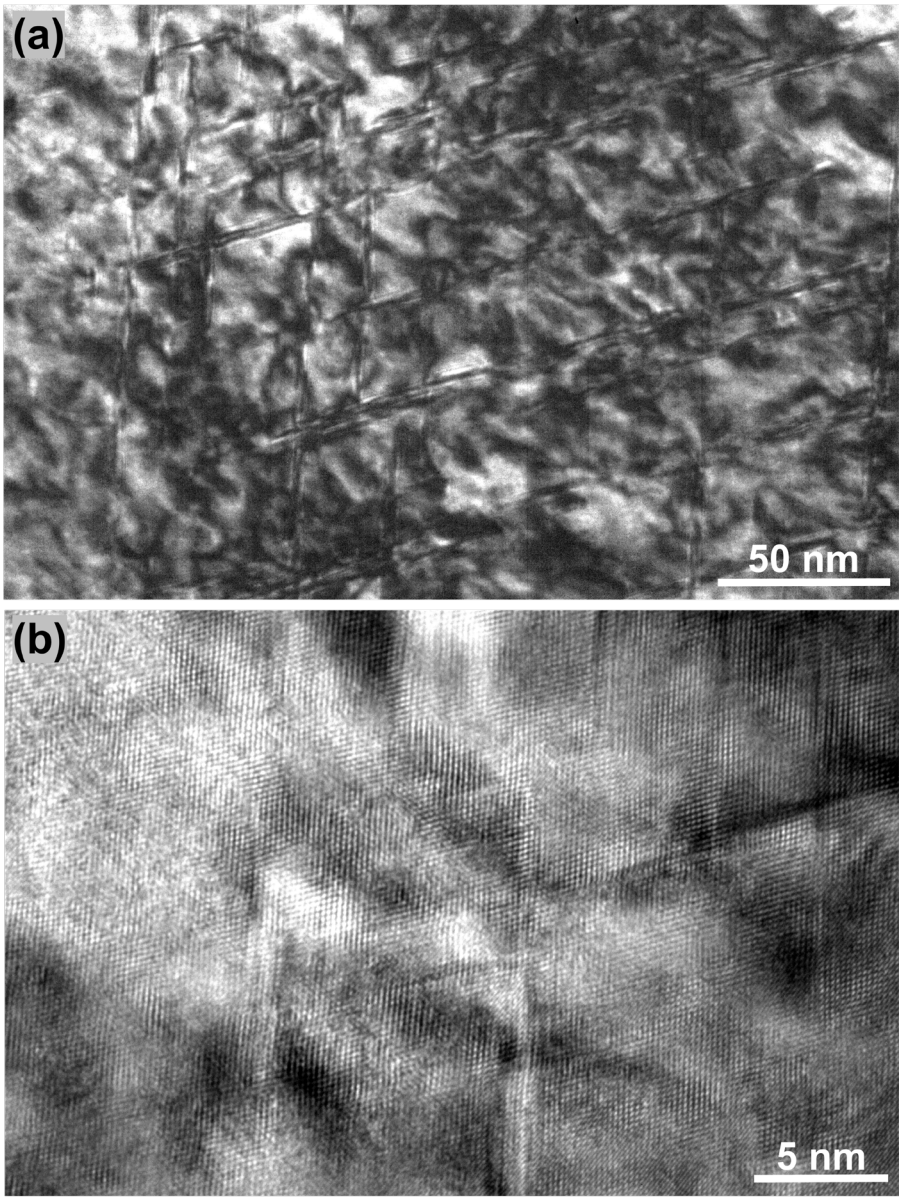

Fig. 4.13. (a) TEM image (enlarged view of Fig. 9(b)) and (b) HRTEM image (a clean version of Fig. 9(c)) of the 5Nb alloy at the 20% strain condition.

4.5 Conclusions

In this chapter, a new class of HEAs with a high strength-ductility synergy was developed via dual-precipitation of $L1_2$ and Laves phases, and the precipitate microstructures, mechanical properties, and deformation behavior of the alloys were thoroughly investigated. The following conclusions are drawn.

1. Adding 3–7 at.% Nb to the $(Ni_2Co_2FeCr)_{96-x}Al_4Nb_x$ system results in the dual precipitation of $L1_2$-$(Ni, Co)_3(Al, Nb)$ particles $(Co, Cr, Fe, Ni)_2Nb$-type Laves precipitates. The $L1_2$ nanoparticles have an average radius of 5.2 nm and a volume fraction of 27% and are uniformly distributed in the matrix, whereas the Laves precipitates have a block shape and form at grain boundaries. First-principles calculations reveal that Nb preferentially partitions to the $L1_2$ nanoparticles and enhances the stability of the $L1_2$ phase.
2. The 5Nb alloy strengthened by dual precipitation of $L1_2$ nanoparticles and Laves precipitates exhibits a yield strength of more than 1400 MPa, an ultimate tensile strength of over 1800 MPa, and a uniform elongation of 18%, achieving a good combination of high strength and ductility. The strengthening modelling indicates that the $L1_2$ precipitation strengthening provides the major contribution to the increase of yield strength, and the collective strengthening contributions from the $L1_2$ precipitation strengthening, Laves strengthening, together with grain boundary strengthening and solid solution strengthening, elevate the yield strength of the 5Nb alloy to more than 1400 MPa.
3. The good ductility of the 5Nb alloy is attributed to its high work hardening capability. Particularly, a high density of SFs in different directions is activated, which leads to the formation of hierarchical SF networks and immovable LC locks, which provide an efficient source of work hardening capability for the 5Nb alloy, resulting in a prominent level of strength-ductility synergy.
4. The $L1_2$ precipitates are sheared by SFs, which facilitates long-range dislocation gliding through the matrix. The extensive SF interactions may

serve as strong strain localized regions and initiate the formation of micro voids, thereby leading to the dimpled ductile fracture. In contrast, dislocations are piled-up against the interface between the Laves precipitates and matrix, which increases the work hardening capability at the early stages of plastic deformation but causes stress concentrations.

Chapter 5 Precipitate evolution, recrystallization, and mechanical properties of an ultrastrong HEA strengthened by $L1_2$ discontinuous precipitates

5.1 Introduction

Previous studies indicated that $L1_2$ precipitates can form through two distinct modes: CP and DP. In CP, $L1_2$ precipitates nucleate homogeneously and uniformly within the grain interiors, independent of grain boundaries or other lattice defects. Their growth is governed primarily by bulk diffusion of solute atoms through the matrix, driven by the chemical potential gradient between the supersaturated solid solution and the equilibrium precipitate phase. Due to the isotropic nature of diffusion-controlled growth, CP results in fine, spherical (or near-spherical) nanoprecipitates with sizes typically ranging from a few to several tens of nanometers. For instance, Yang *et al.* [19] developed a $(CoFeNi)_{86}Al_7Ti_7$ (at.%) alloy strengthened by a high density of multicomponent spherical $L1_2$ precipitates, which exhibits an excellent combination of high strength and ductility, with a yield strength exceeding 1000 MPa, an ultimate tensile strength of 1500 MPa, and a uniform elongation of 50%. In contrast, DP typically initiates heterogeneously at grain boundaries and proceeds predominantly through grain boundary diffusion, resulting in the formation of rod-like or lamellar microstructures [26, 117]. While CP-formed coherent nanoprecipitates are well recognized for their pronounced strengthening effect, recent studies have shown that DP can also be beneficial by providing precipitation strengthening and promoting grain refinement, thereby substantially enhancing mechanical properties. For instance, Xie *et*

al. [118] demonstrated that leveraging DP to form nanoscale rod-like $L1_2$ precipitates in a $(CoCrNi)_{94}Al_3Ti_3$ alloy can effectively induce a heterogeneous microstructure with a high density of fine grains. This DP-induced heterostructure significantly enhances both the strength and ductility of the alloy at cryogenic temperatures, achieving an ultimate tensile strength of 1750 MPa and a ductility of 34% at –173 °C. Given that the size and spatial distribution of precipitates are critical to strengthening, comprehensive research into the precise control and optimization of DP is essential.

Several studies have reported that high-density DP-formed nano-rods or nano-lamellae can be achieved through specific thermomechanical processing routes, providing new possibilities for tailoring the precipitation morphology and distribution. For example, Dasari *et al.* [119] demonstrated that a fully DP-formed nano-rod $L1_2$ microstructure in an $Co_{1.5}CrFeNi_{1.5}Al_{0.2}Ti_{0.3}$ HEA leads to a significant enhancement in mechanical performance, achieving a high yield strength of approximately 1.4 GPa and an ultimate tensile strength of approximately 1.6 GPa, while maintaining a tensile ductility of ~14% at room temperature. Gwalani *et al*. [120] reported that a $Co_{0.7}CrFeNi_{1.7}Al_{0.2}Ti_{0.2}$ HEA with a microstructure densely populated by DP-formed $L1_2$ nano-rods embedded in ultrafine FCC grains exhibits a yield strength of ~1.6 GPa, an ultimate tensile strength of ~1.7 GPa, and a ductility of around 15%. Notably, Fan *et al*. [21] developed a $(CoCr_{0.5}FeNi_{1.5})_{87.5}Al_{7.5}Ti_5$ HEA featuring a uniform nano-rod $L1_2$ architecture and ultrafine grains (400 nm in size), achieving a yield strength exceeding 2 GPa and a uniform tensile ductility of 16% at room temperature. This combination of high strength and good ductility highlights the excellent potential of DP-formed nano-rod $L1_2$ structures for achieving a favorable strength–ductility balance in ultrastrong HEAs. In view of the outstanding mechanical performance of HEAs strengthened by DP-formed precipitates, it is essential to understand the fundamental

mechanisms that govern microstructural formation and evolution. Particularly, since CP and DP are characterized by fundamentally different nucleation and growth behaviors, clarifying their competition and interplay in these alloys is crucial for the further optimizing microstructure and mechanical performance.

The aim of this chapter is to elucidate the mechanisms governing the formation and transformation of DP-formed coherent nanorod structures, to explore the interplay between precipitation and ultrafine grain formation, and to clarify the associated strengthening mechanisms. Specifically, we focused on the ultrastrong-yet-ductile $(CoCr_{0.5}FeNi_{1.5})_{87.5}Al_{7.5}Ti_5$ HEAs, systematically investigating its microstructural evolution and mechanical properties under various aging temperatures and durations. Advanced characterization techniques, including electron microscopy and SANS, were employed to analyze grain and precipitate microstructures. Particular attention was paid to the interaction between recrystallization and precipitation, as well as the evolution of DP-formed microstructures at different aging stages. Mechanical behavior was evaluated through tensile testing, and the relative contributions of different strengthening mechanisms were quantitatively assessed. These findings provide valuable insights into microstructural evolution and the structure–property relationships in precipitation-strengthened HEAs.

5.2 Results

5.2.1. Microstructure

Figure 5.1 presents the SEM morphologies of the alloy under various aging conditions, while Fig. 5.2 shows the corresponding microstructures at high magnification. After aging at 500 °C for 0.5 and 2 h, the samples consist predominantly

of residual deformed grains (Figs. 5.1a and b). In the corresponding high-magnification images, no distinct characteristic microstructures can be identified (Figs. 5.2a and b). With increasing aging time to 8 and 32 h, distinct strips wit h bright contrast emerge. As shown in the Figs. 5.2c and d, these regions reveal the formation of nano-rod structures, which correspond to DP-formed $L1_2$ phases, as revealed in our previous study [21]. Compared to 500 °C, aging at 600 °C results in a significantly higher fraction of DP regions, with obvious DP areas appearing at the initial aging stage (0.5 h). At this temperature, a nearly full DP structure is achieved after 8 h of aging, and the high-magnification image shown in Fig. 5.2g demonstrates a dense, discontinuously precipitated nano-rod $L1_2$ structures.

Figure 5.1i shows that, at 700 °C, the bright-contrasted DP regions occupy more than 50% of the microstructure after only 0.5 h of aging, indicating a dramatic acceleration of the DP process at this elevated temperature. Notably, at this stage, spherical nanoscale $L1_2$ precipitates formed via CP are observed within the dark-contrasted region (Fig. 5.2i), a phenomenon also reported by Gwalani *et al* [120]. As the aging time further increases, the nano-rod structures produced by DP gradually become the predominant feature in the microstructure (Figs. 5.2j-l), reflecting the competitive interplay between DP and CP mechanisms [71]. At 800 °C, precipitation proceeds even more rapidly. Although both DP and CP structures can be observed at shorter aging times, as shown in Fig. 5.2m, with prolonged aging time, the fully coarsened nano-rod structures formed by DP eventually dominate the microstructure.

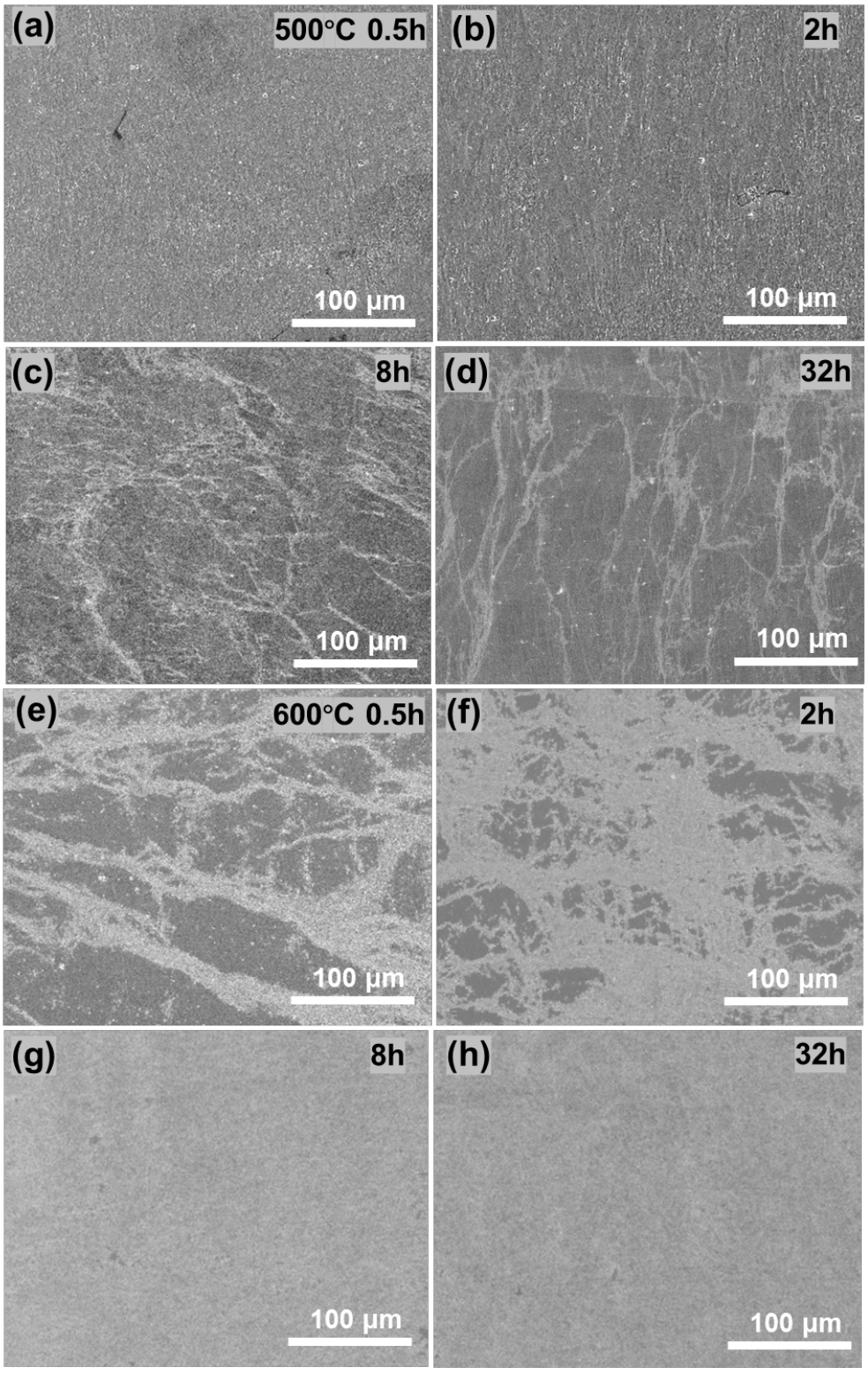
(a)
500°C 0.5h
100 μm
(b)
2h
100 μm
(c)
8h
100 μm
(d)
32h
100 μm
(e)
600°C 0.5h
100 μm
(f)
2h
100 μm
(g)
8h
100 μm
(h)
32h
100 μm

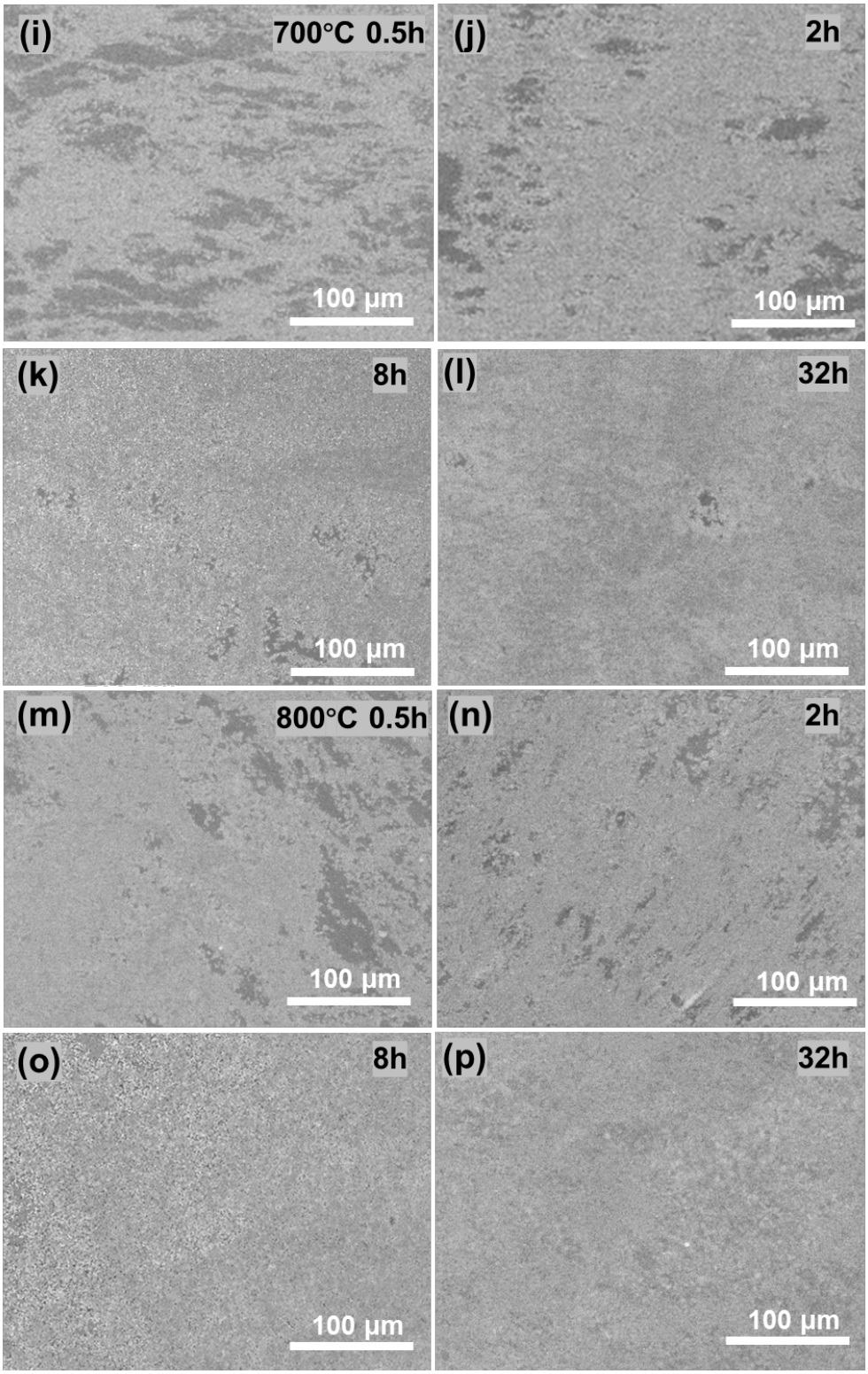

Fig. 5.1. SEM images of the alloy under different heat-treatment conditions: (a–d) 500 °C aged for 0.5, 2, 8, and 32 h, respectively; (e–h) 600 °C aged for 0.5, 2, 8, and 32 h, respectively; (i–l) 700 °C aged for 0.5, 2, 8, and 32 h, respectively; (m–p) 800 °C aged for 0.5, 2, 8, and 32 h, respectively.

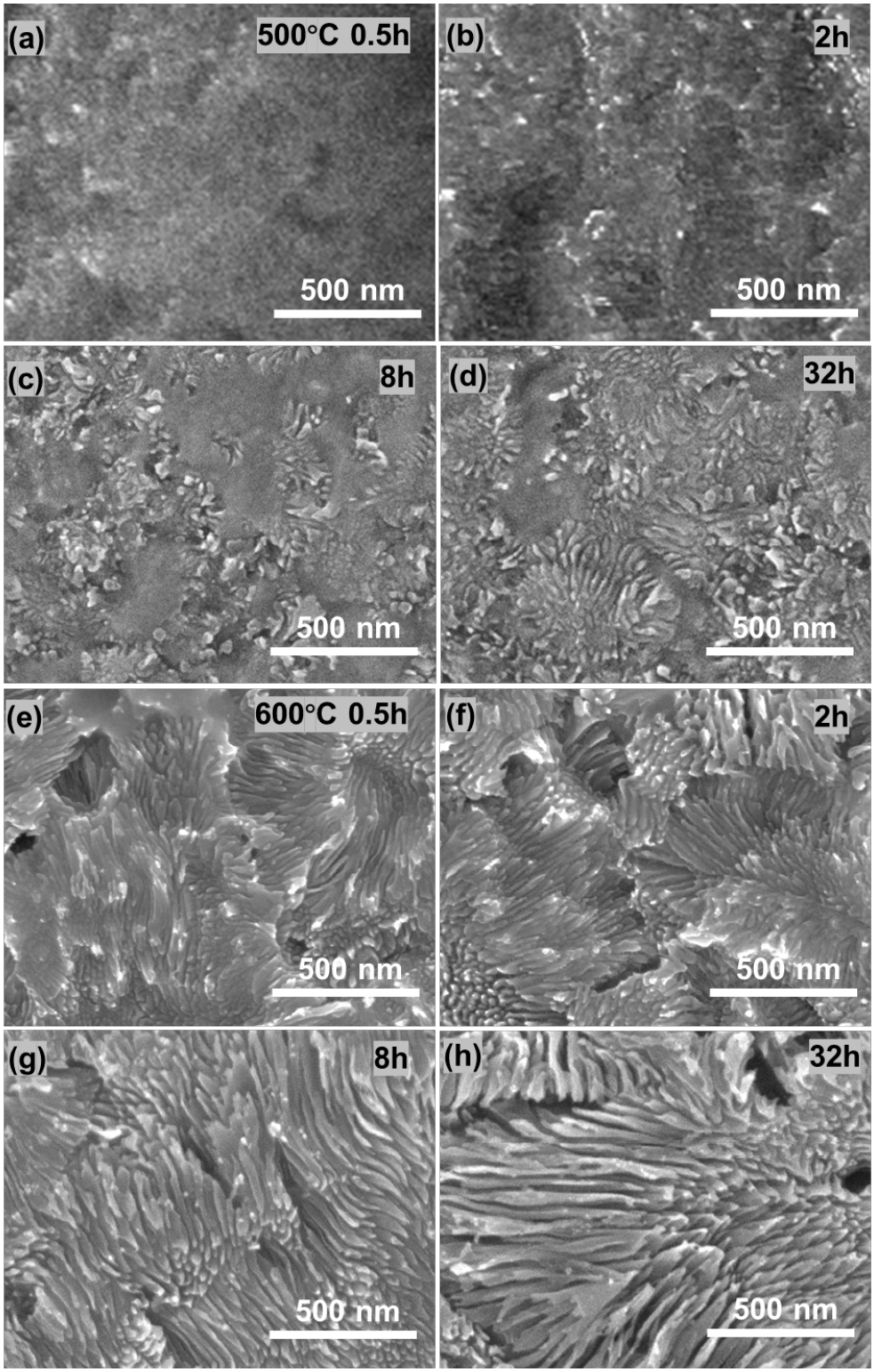
(a)
500°C 0.5h
500 nm
(b)
2h
500 nm
(c)
8h
500 nm
(d)
32h
500 nm
(e)
600°C 0.5h
500 nm
(f)
2h
500 nm
(g)
8h
500 nm
(h)
32h
500 nm

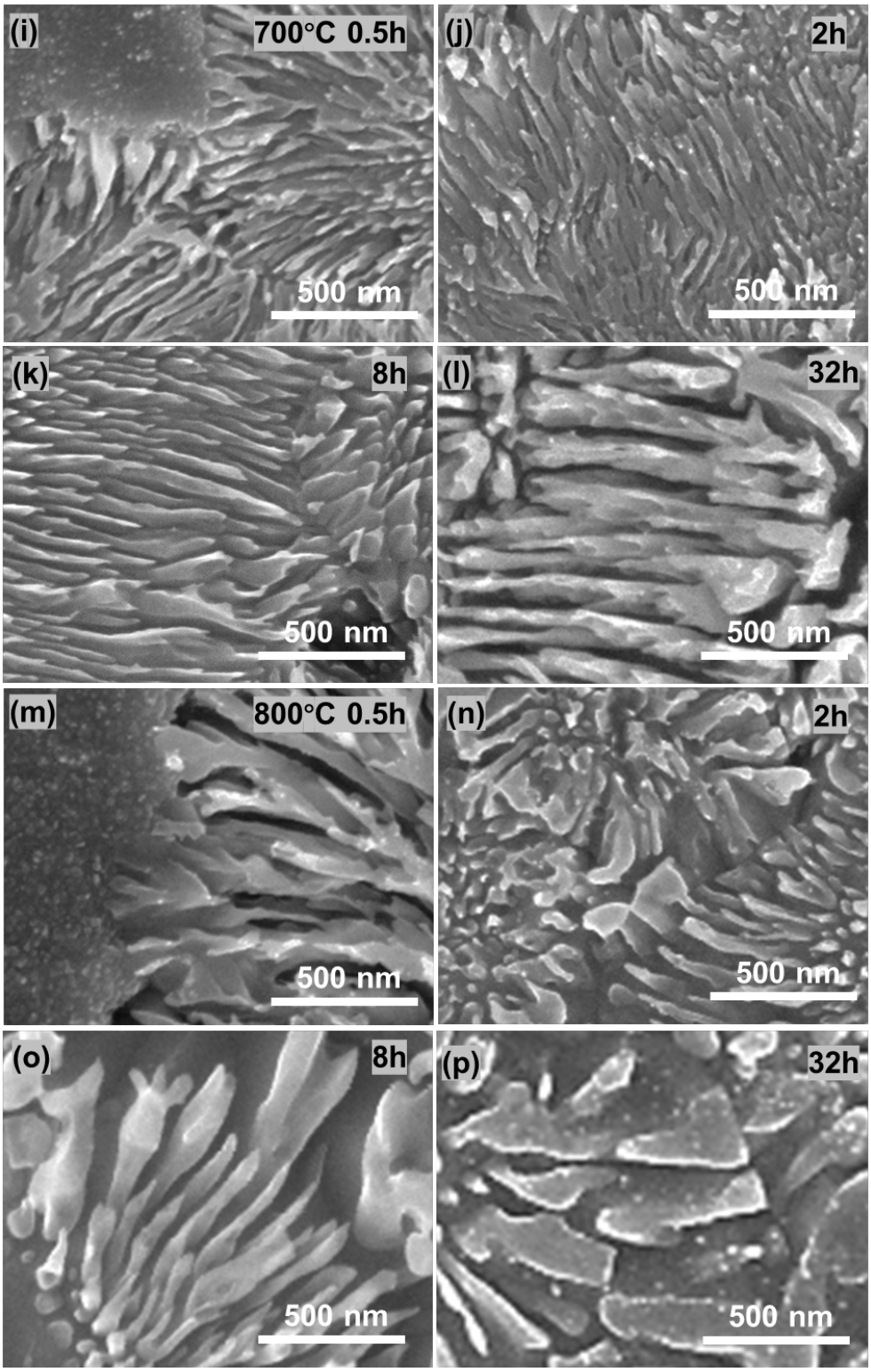

Fig. 5.2. High-magnification SEM images of the alloy under different heat-treatment conditions: (a–d) 500 °C aged for 0.5, 2, 8, and 32 h, respectively; (e–h) 600 °C aged for 0.5, 2, 8, and 32 h, respectively; (i–l) 700 °C aged for 0.5, 2, 8, and 32 h, respectively; (m–p) 800 °C aged for 0.5, 2, 8, and 32 h, respectively.

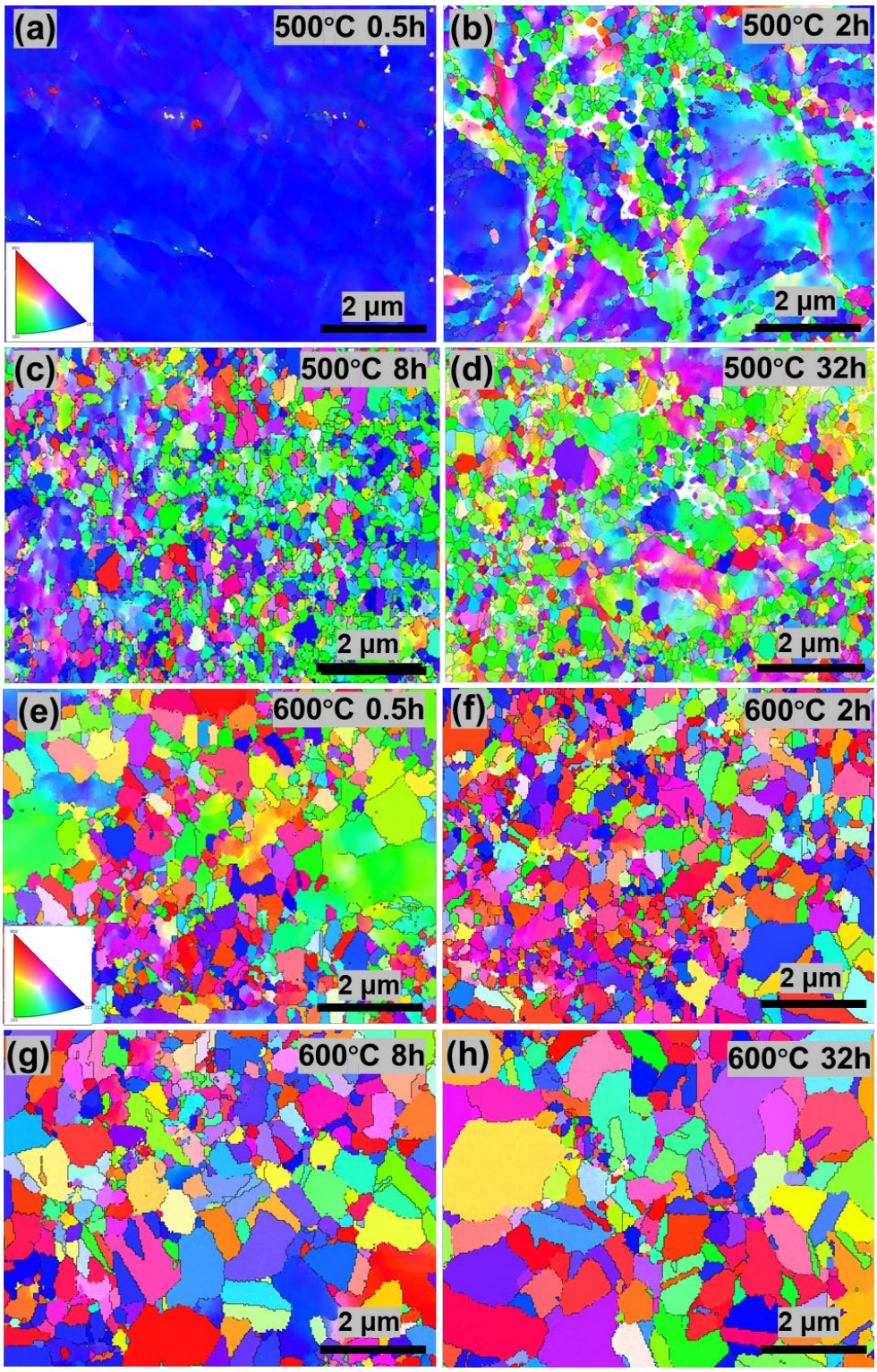
(a)
500°C 0.5h
2 μm
(b)
500°C 2h
2 μm
(c)
500°C 8h
2 μm
(d)
500°C 32h
2 μm
(e)
600°C 0.5h
2 μm
(f)
600°C 2h
2 μm
(g)
600°C 8h
2 μm
(h)
600°C 32h
2 μm

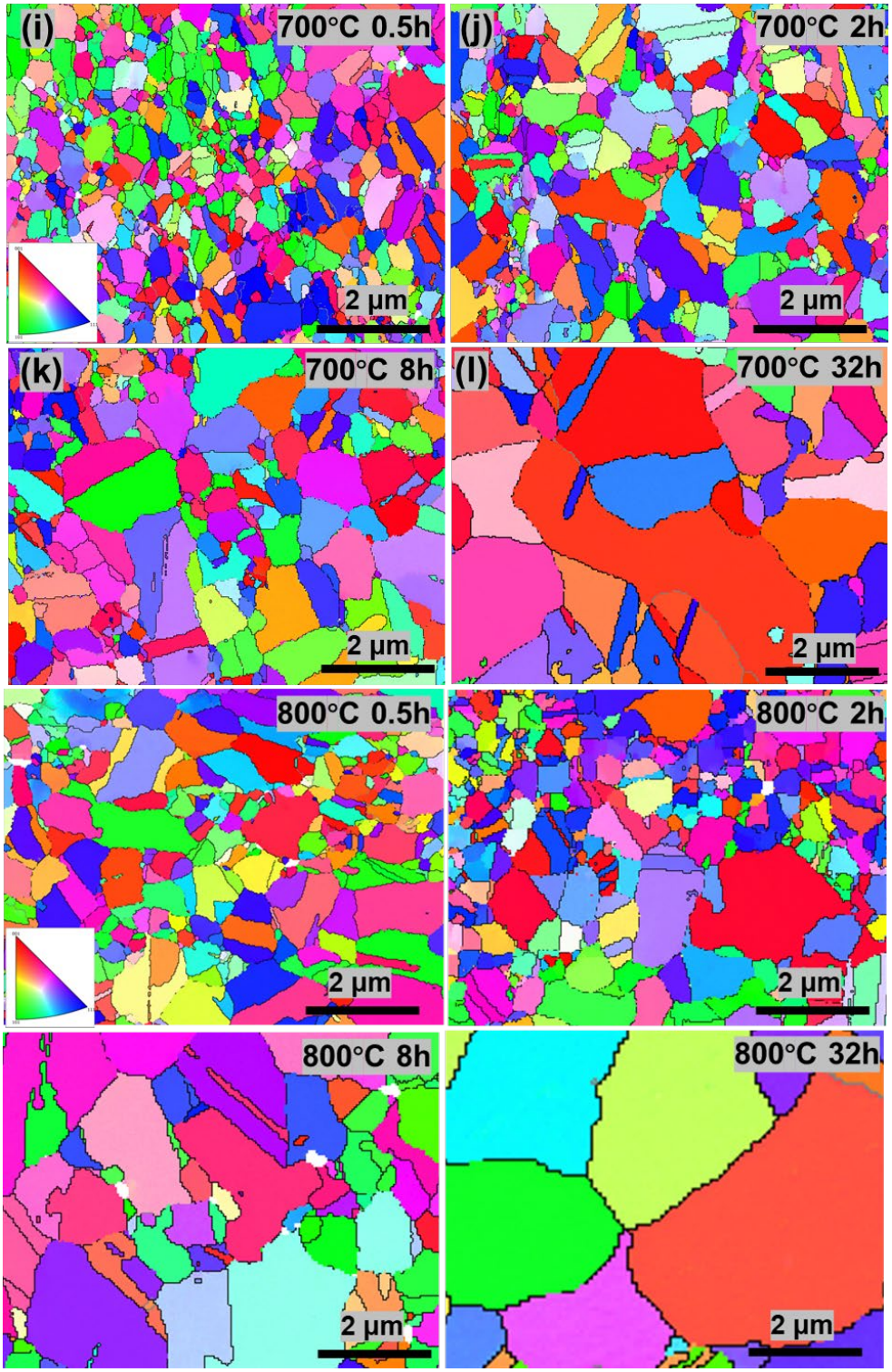

Fig. 5.3. EBSD IPF maps of the alloy under different heat-treatment conditions: (a–d) 500 °C aged for 0.5, 2, 8, and 32 h, respectively; (e–h) 600 °C aged for 0.5, 2, 8, and 32 h, respectively; (i–l) 700 °C aged for 0.5, 2, 8, and 32 h, respectively; (m–p) 800 °C aged for 0.5, 2, 8, and 32 h, respectively.

EBSD analysis was conducted to characterize the evolution of grain structures under various aging conditions. Figure 5.3 presents the EBSD inverse pole figure (IPF) maps of the alloy aged at 500-800 °C for different durations. At 500 °C, the microstructure shows no visible grain boundaries and exhibits strong texture after aging for 0.5 h, indicating that the sample retains a deformed structure with no evidence of recrystallization. As the aging time increases to 2 h, a noticeable number of ultrafine, distinguishable grains appear, suggesting the onset of recrystallization. With further aging at this temperature, the extent of recrystallization increases, while the grain size remains largely unchanged, eventually reaching approximately 190 ± 15 nm after aging for 32 h. At 600 °C, a considerable fraction (40%) of deformed regions is still present after aging for 0.5 h, while the average size of recrystallized grains measure approximately 210 ± 21 nm. After 2 h of aging, fully recrystallized equiaxed grains are observed. Continued aging leads to grain growth, with the grain size reaching 670 ± 25 nm after 32 h of aging. At 700 °C, fully recrystallized equiaxed grains can be observed after just 0.5 h of aging, and the subsequent grain growth follows a similar trend to that at 600 °C, reaching 800 ± 28 nm after 32 h of aging. At 800 °C, the rate of grain growth is significantly accelerated, with the grain size at each aging time being much larger than those observed at lower temperatures. The grains coarsen rapidly, ultimately reaching 2.3 ± 0.06 μm after 32 h of aging.

In addition, grain orientation spread (GOS) maps were used to quantify the volume fraction of recrystallized regions under different aging conditions. It is generally recognized that recrystallized grains are characterized by low GOS values (GOS $\leq$ 1°), whereas sub-grains and deformed grain regions exhibit higher GOS values (GOS $\geq$ 1°). Figure 5.4 displays the EBSD GOS maps of the alloy under different aging conditions.

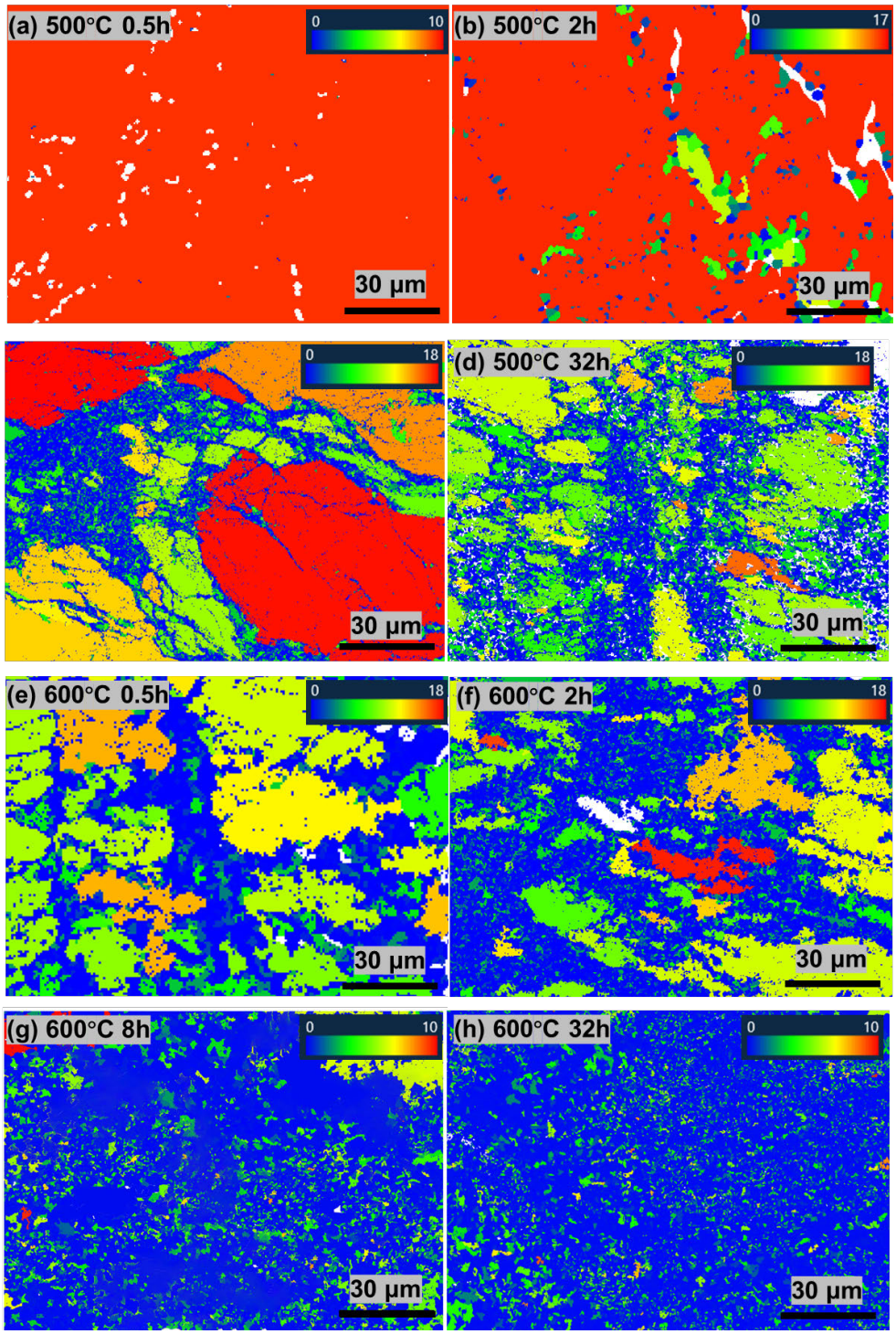
(a) 500°C 0.5h
0
10
30 μm
(b) 500°C 2h
0
17
30 μm
0
18
30 μm
(d) 500°C 32h
0
18
30 μm
(e) 600°C 0.5h
0
18
30 μm
(f) 600°C 2h
0
18
30 μm
(g) 600°C 8h
0
10
30 μm
(h) 600°C 32h
0
10
30 μm

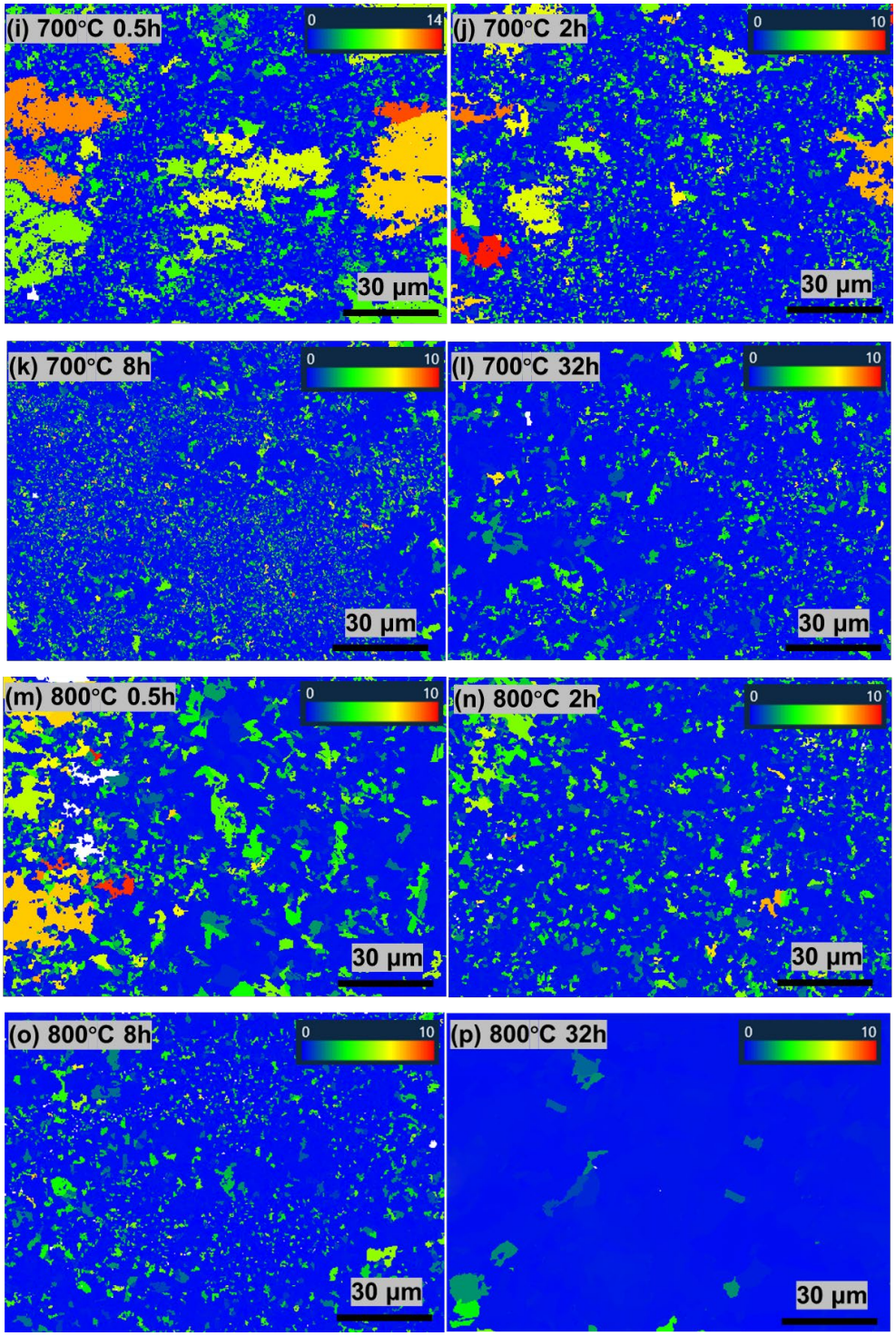

Fig. 5.4. EBSD GOS maps of the alloy under different heat-treatment conditions: (a–d) 500 °C aged for 0.5, 2, 8, and 32 h, respectively; (e–h) 600 °C aged for 0.5, 2, 8, and 32 h, respectively; (i–l) 700 °C aged for 0.5, 2, 8, and 32 h, respectively; (m–p) 800 °C aged for 0.5, 2, 8, and 32 h, respectively.

Figures 5.5a and b summarize the variations in the area fraction of recrystallized regions and the average grain size within these regions, respectively. At 500 °C, no fully recrystallized regions are observed after 0.5 h of aging; only a small fraction of recrystallized grains become visible after 2 h of aging. Even after prolonged aging for 32 h at this temperature, only about 28% of the sample is recrystallized, which is consistent with the SEM observations in Figs. 5.1a-d.

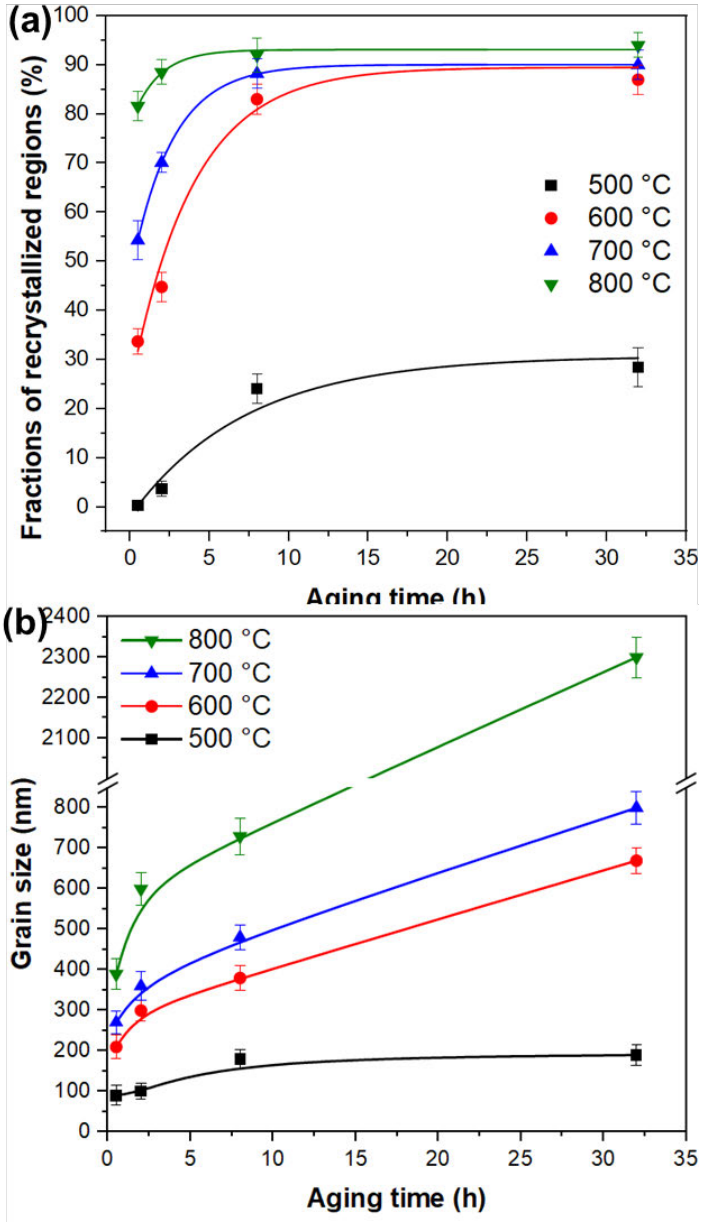

Fig. 5.5. (a) Area fractions of recrystallized regions and (b) grain sizes within these regions of the alloy under different heat-treatment conditions.

This sluggish recrystallization behavior at 500 °C stands in sharp contrast to the much higher recrystallization rate observed at 600 °C. At 600 °C, recrystallized regions are already detectable after 0.5 h of aging, and the fraction of recrystallized grains increases rapidly with aging time. Notably, after 8 h of aging at this temperature, nearly 85% of the microstructure is recrystallized. At 700 °C and 800 °C, more than 70% of the microstructure is already recrystallized after only 0.5 h of aging, indicating a pronounced acceleration of the recrystallization process. At these elevated temperatures, recrystallization is completed much more quickly, with the fraction recrystallized regions eventually exceeding 90%. It is important to note that the kinetics of recrystallization vary significantly with temperature.

At lower temperatures, such as 500 °C, the recrystallization process is sluggish and the fraction of recrystallized regions increases slowly, even after extended aging. As the temperature increases, both the nucleation and growth rates of recrystallized grains are significantly enhanced, leading to rapid completion of recrystallization at 700 °C and above. This behavior underscores the strong temperature dependence of the recrystallization process, which is governed by the increased atomic mobility and driving force for grain boundary migration at elevated temperatures.

Based on the comprehensive microstructural analysis of the alloys subjected to various heat-treatment conditions, the samples aged at 600 °C for 0.5, 2, 8, and 32 h were selected to investigate the temporal evolution of DP-formed precipitates, and corresponding high-resolution SEM images have been presented in Fig. 5.2e-h. In the 0.5-h aged condition, although the recrystallization fraction is only 33.7%, coherent nano-rod $L1_2$ precipitates with an average width of approximately 22 ± 5 nm are readily observed (Fig. 5.2e). As the aging time increases to 2 h, the precipitate size and distribution remain largely unchanged. After 8 h of aging, with a significantly increased

fraction of recrystallization regions, the nano-rod structures coarsen and are distributed throughout the grains, with their width increasing to approximately 38 ± 6 nm. Following 32 h of aging, substantial coarsening of the nano-rod precipitates along the grain boundaries is evident, with an average width reaching 48 ± 8 nm.

5.2.2. SANS measurements

SANS measurements were carried out to further investigate the effect of aging time on the size and distribution of nano-rod precipitates in the alloy. Figure 5.6 shows the scattering profiles of samples aged at 600 °C for 0.5, 2, 8, and 32 h. A distinct scattering bump is clearly visible in the profile of the sample aged for 0.5 h, indicating the formation of a high density of precipitates with relatively uniform size. This result is consistent with the SEM observation in Fig. 5.2e, which shows rapid precipitation of nano-rod structures occurs after a short aging time at 600 °C. After 2 h of aging, the scattering bump shifts to lower q values, suggesting the growth of the precipitates. As the aging time increases to 8 and 32 h, the bump moves further towards lower q, reflecting a significant increase in precipitate size. These results indicate that the coherent nano-rod $L1_2$ precipitates gradually coarsen with increasing aging time, in good agreement with the SEM microstructural analysis.

The size distribution of the nanoscale precipitates was further analyzed by fitting the scattering profiles using the cylinder model in SasView 5.0. This model incorporates a power law function, a lognormal size distribution of cylinders, and a flat background, and can be expressed by [73]:

$$I(q) = Aq^{-4} + NF^2(q,\alpha) + B \tag{5.1}$$

where A is a scale factor, N is the number density of precipitates, B is the background scattering, α is the angle between the axis of the cylinder and Q vector, and $F(q, \alpha)$ is the form factor [121]. For the cylinder model,

$$F(q) = 2(\Delta\rho)V \frac{\sin(0.5qL\cos\alpha)}{0.5qL\cos\alpha} \frac{J_1(qR\sin\alpha)}{qR\sin\alpha} \tag{5.2}$$

where V is the volume of a single precipitate, L is the length of the cylinder, R is the radius of the cylinder, $\Delta\rho$ is the scattering length density difference between matrix and precipitates, and J_1 is first order Bessel function. The grey curves in Fig. 5.6 show the fitting results for different aging conditions, while the inset illustrates the evolution of the size distribution with aging time at 600 °C. From 0.5 to 2 h, the size distribution curves shift slightly towards larger R values, but the changes in peak position and width are relatively minor, suggesting only modest growth of the precipitates during this period. As the aging time is extended to 8 and 32 h, the size distribution curves shift more substantially towards larger R values, and the distributions become significantly broader. These results indicate that with prolonged aging, the precipitates experience significant coarsening, characterized by both an increase in average size and a wider size distribution. Table 5.1 summarizes the dependence of precipitate size (radius and length) and volume fraction on aging time, as determined from the fitting results. The average radius increases from 11.6 ± 2.7 in the 0.5 h condition to 21.3 ± 4.3 nm in the 32 h condition, which is in good agreement with values observed by SEM and also consistent with our previous findings [21]. In addition, the length of the nano-rod precipitates increases from 456 ± 32 nm at 0.5 h to 670 ± 45 nm at 32 h. The volume fraction of the precipitates also increases with longer aging times.

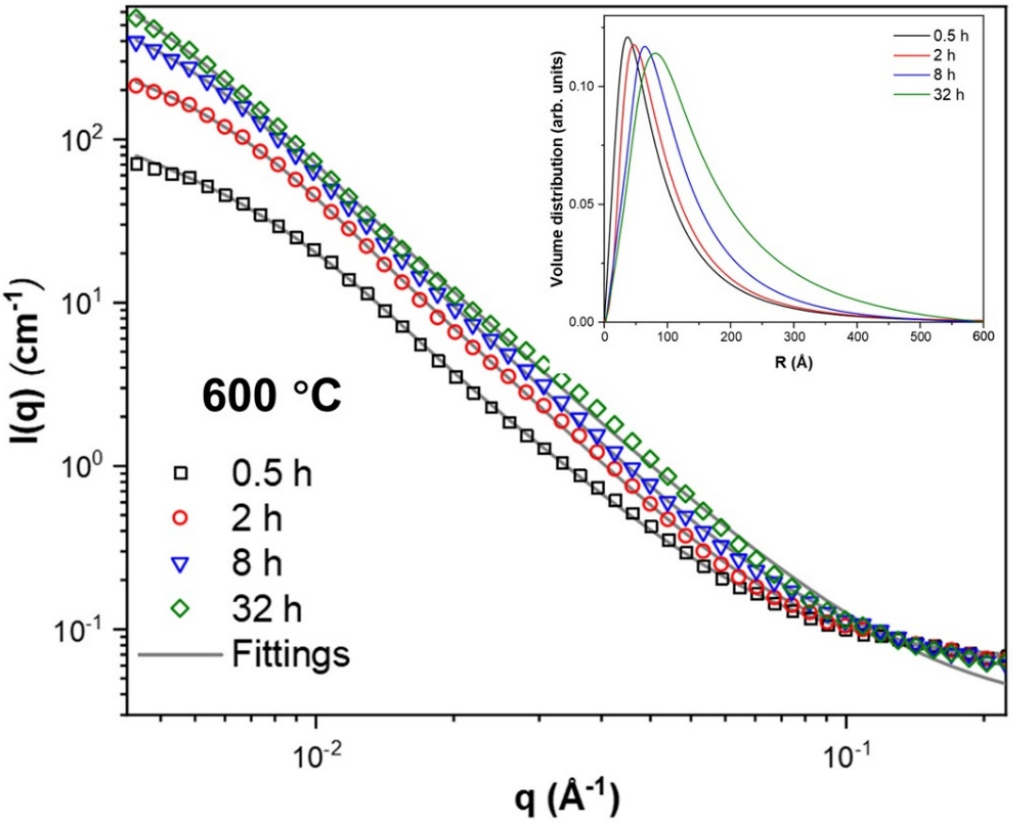

Fig. 5.6. SANS profiles and corresponding fitting curves of the samples aged at 600 °C for 0.5, 2, 8, and 32 h. The inset displays the evolution of the precipitate size distribution.

Table 5.1. Average radii (*r*), lengths (*l*), and volume fractions (*f*) of the nano precipitates in the samples under different aging times at 600 °C.

Aging time (h)	*r* (nm)	*l* (nm)	*f* (%)
0.5	11.6 ± 2.7	456 ± 32	21
2	13.5 ± 2.4	524 ± 25	34
8	16.3 ± 3.1	654 ± 49	55
32	21.3 ± 4.3	670 ± 45	58

5.2.3. Mechanical properties

Room-temperature tensile tests were performed to investigate the effect of aging treatment on the mechanical properties of the $(CoCr_{0.5}FeNi_{1.5})_{87.5}Al_{7.5}Ti_5$ alloy. Figure 5.7a shows representative engineering stress–strain curves for the samples aged for 0.5, 2, 8, and 32 h at 600 °C, with corresponding yield strength, ultimate tensile strength, total elongation, and uniform elongation summarized in Table 5.2.

The sample aged for 0.5 h fractured in a brittle manner before reaching its yield point. The 2-h aged sample exhibits a yield strength of 1890 ± 14 MPa and a total elongation of 9 ± 3%. With increased aging time to 8 h, both the yield strength and ultimate tensile strength of the samples further increase, reaching 2000 ± 11 and 2120 ± 13 MPa, respectively, while maintaining a uniform elongation of 16 ± 2% and a total elongation of 18 ± 2%. After aging for 32 h, the yield strength decreases to 1510 ± 15 MPa, while the uniform and total elongations remain comparable to those of the 8-h aged sample. Based on these tensile test results, the 8-h aging time was selected for further study, and tensile tests were performed on samples aged for 8 h at 500 °C, 700 °C, and 800 °C. As shown in Fig. 5.7b, the sample aged at 500 °C also exhibits brittle fracture before reaching its yield point. In contrast, at 700 °C and 800 °C, the yield strengths decrease by 380 and 830 MPa, respectively, compared to that at 600 °C. However, both samples demonstrate a significant improvement in work-hardening capability.

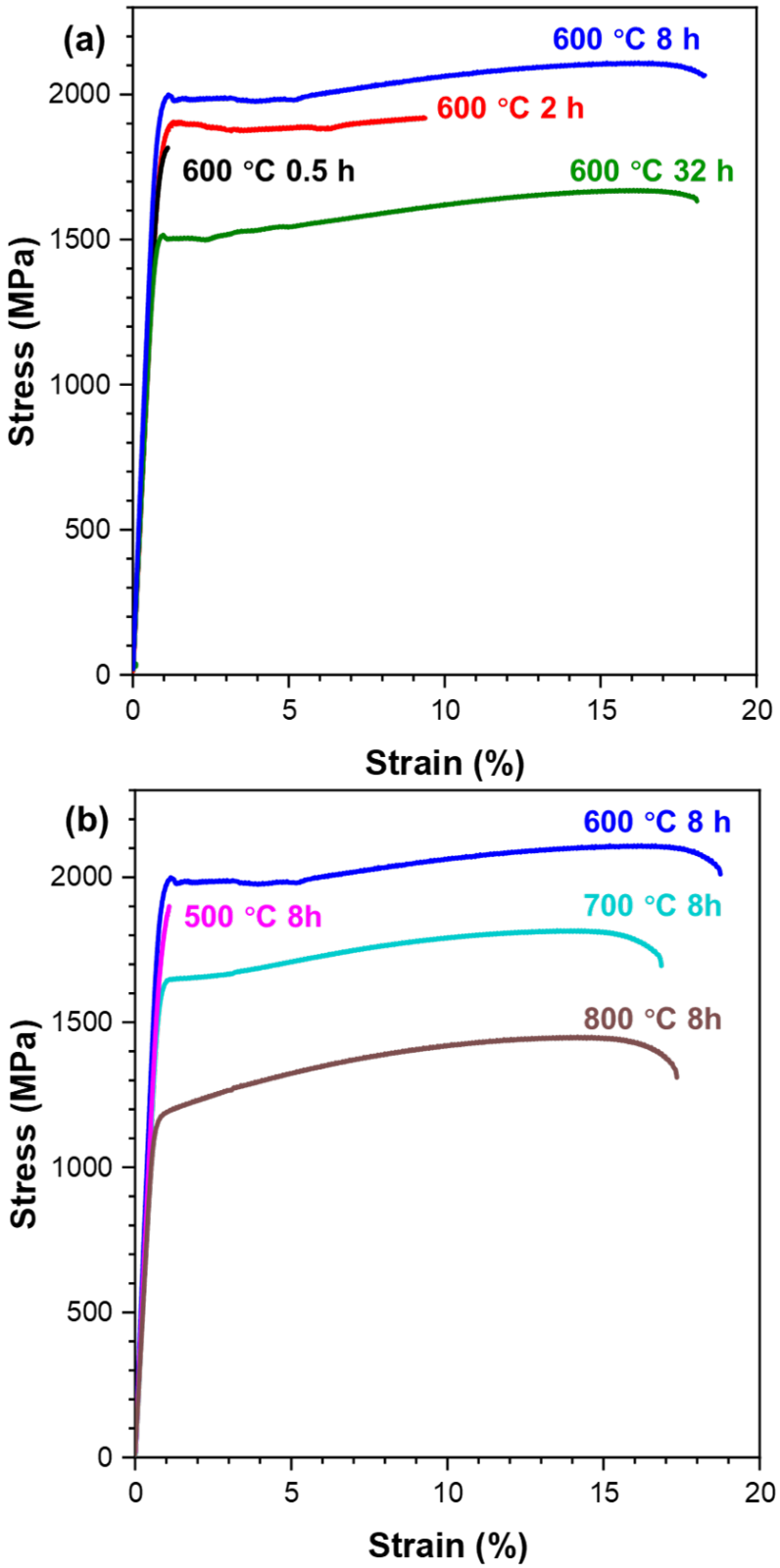

Fig. 5.7. Tensile engineering stress–strain curves of the $(CoCr_{0.5}FeNi_{1.5})_{87.5}Al_{7.5}Ti_5$ at different aging conditions: (a) aged at 600 °C for virous times, and (b) aged for 8 h at different temperatures.

Table 5.2. Yield strengths (YS), ultimate tensile strengths (UTS), elongations-to-failure (EF), and uniform elongations (UE) of the samples under different heat-treatment conditions.

Alloy	YS (MPa)	UTS (MPa)	EF (%)	UE (%)
600 °C/0.5h	1820 ± 13	1820 ± 13	1 ± 0.5	1 ± 0.5
600 °C/2 h	1890 ± 14	1920 ± 14	9 ± 3	9 ± 3
600 °C/8 h	2000 ± 11	2120 ± 13	19 ± 2	16 ± 2
600 °C/32h	1510 ± 15	1675 ± 14	19 ± 3	16 ± 3
500 °C/8 h	1900 ± 12	1900 ± 12	1 ± 0.3	1 ± 0.3
700 °C/8 h	1618 ± 13	1830 ± 16	17 ± 4	15 ± 3
800 °C/8 h	1170 ± 18	1480 ± 21	18 ± 3	15 ± 3

Based on the tensile test results described above, it is evident that the samples with coherent nano-rod precipitates exhibit excellent mechanical properties under various heat-treatment conditions. In particular, the sample aged at 600 °C for 8 h demonstrates an outstanding combination of strength and ductility, with a yield strength exceeding 2000 MPa and a total elongation approaching 20%. To further highlight these superior properties, we compare the mechanical performance of the $(CoCr_{0.5}FeNi_{1.5})_{87.5}Al_{7.5}Ti_5$ alloy with other previously reported $L1_2$-strengthened HEAs (including those strengthened by CP- and DP-formed $L1_2$ phases) and topologically close-packed (TCP) phase-strengthened HEAs [19, 22, 67, 79, 82, 86, 89, 90, 92, 119, 122-129]. Compared with conventional HEAs strengthened by spherical $L1_2$ precipitates, this alloy exhibit a 50% increase in yield strength. Furthermore, in comparison to HEAs strengthened by other rod/lamellar precipitates or intermetallic compounds, the samples in this work display a substantial improvement in total elongation, with a twofold increase relative

to previous reports (Fig. 5.8). As a result, the coherent nano-rod alloys offer an impressive combination of high yield strength and large uniform ductility, making them promising candidates for structural applications.

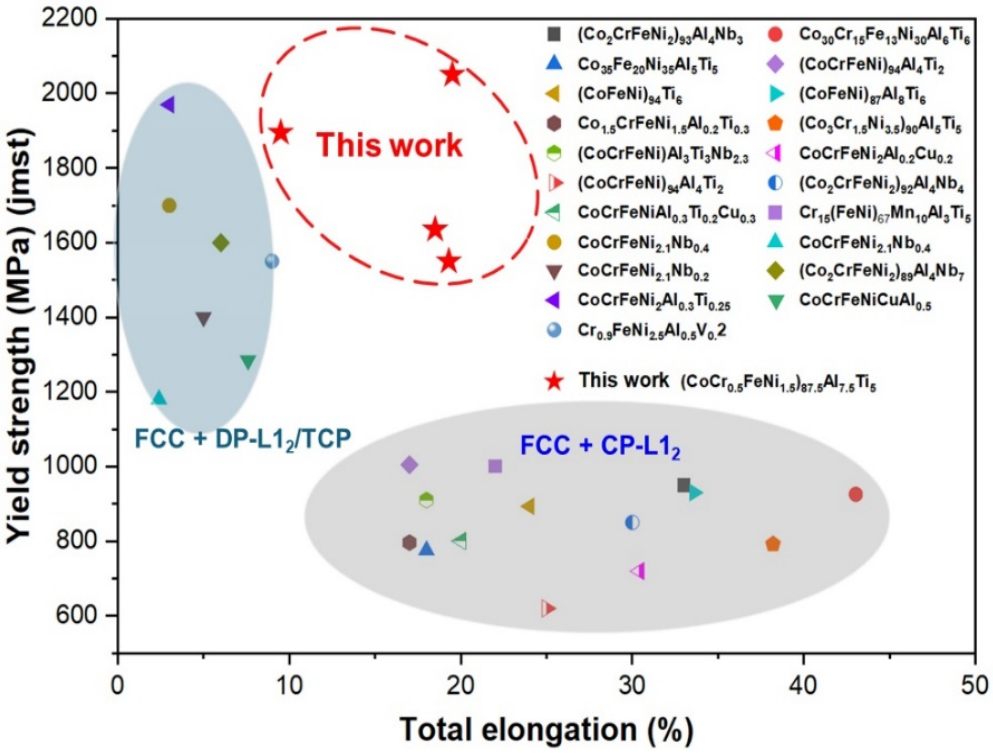

Fig. 5.8. The yield strength versus total elongation of the coherent nano-rod $L1_2$ HEAs in comparison with various types of precipitation-strengthened HEAs.

5.3 Discussion

5.3.1. Mechanisms of microstructural evolution

The microstructural evolution in the $L1_2$ nanorod-strengthened $(CoCr_{0.5}FeNi_{1.5})_{87.5}Al_{7.5}Ti_5$ HEA is governed by the intricate interplay between recrystallization and precipitation, both of which are highly temperature-dependent. Rather than occurring independently, these two processes are strongly coupled, with each influencing the kinetics and pathway of the other during thermal treatments. Upon

annealing a supersaturated single-phase solid solution in the two-phase field, supersaturation is relieved through solid-state reactions that proceed either by CP throughout the matrix or by DP at migrating grain boundaries [130]. In this alloy system, the dominant precipitation mechanism is DP, which is closely associated with grain boundary migration and recrystallization.

At 500 °C, limited atomic mobility results in sluggish recrystallization (Figs. 5.4a-d), with only a small fraction of the microstructure becomes recrystallized even after prolonged aging. Under this condition, DP preferentially initiates along the newly formed grain boundaries, which serve as fast diffusion paths and primary nucleation sites for the $L1_2$ phase. It should be noted that both recrystallization and DP proceed slowly at this temperature due to limited kinetics. As the temperature increases to 600 °C, atomic diffusion is enhanced for both precipitation and recrystallization. Notably, recrystallization and DP occur concurrently and cooperatively: the rapid migration of grain boundaries during recrystallization provides continuous nucleation sites for DP, while the growth of $L1_2$ nanorods further promotes grain boundary migration, influencing both grain morphology and kinetics of recrystallization. During recrystallization, migrating grain boundaries sweep solute atoms and create local supersaturation, facilitating the nucleation of $L1_2$ precipitates at these boundaries. As DP progresses, the concentration gradient across grain boundaries supplies the chemical driving force for the growth of the DP structure, which in turn drives further grain boundary migration and promotes recrystallization. The strong coupling between DP and recrystallization ultimately results in the formation of nanorod-shaped $L1_2$ colonies embedded within the ultrafine-grained FCC matrix. At this temperature, the microstructure evolves toward nearly complete recrystallization, characterized by ultrafine grains with a random texture. This synergistic evolution between DP and

recrystallization is crucial for the development of the uniform nano-rod structure at this temperature. At higher temperatures (700 °C and 800 °C), both recrystallization and precipitation processes are significantly accelerated. Rapid grain boundary migration and increased solute mobility promote swift formation of DP products. Meanwhile, enhanced volume diffusion and high dislocation densities allow CP to occur in some non-recrystallized regions; however, DP remains the dominant mechanism. As aging proceeds, initial CP regions within non-recrystallized grains are gradually replaced by DP as boundaries sweep through these regions. This highlights the dynamic competition and replacement between the two precipitation modes, dictated by the evolving grain structure and the movement of reaction fronts. Therefore, the microstructural and precipitation evolution in the $L1_2$-nanorod strengthened $(CoCr_{0.5}FeNi_{1.5})_{87.5}Al_{7.5}Ti_5$ alloy results from the coupled dynamics of recrystallization and DP, both of which are strongly influenced by temperature. At lower temperatures and with finer grains, DP is favored along migrating grain boundaries, whereas higher temperatures may permit transient CP in non-recrystallized regions–though these are eventually replaced by DP. Understanding this interplay is essential for tailoring the balance between CP and DP and for optimizing the microstructure and mechanical properties of $L1_2$-nanorod strengthened HEAs, as the distribution and growth of nanorods can also influence grain boundary migration and the final grain structure.

5.3.2. Kinetics of DP coarsening and recrystallization

Several classical kinetic models, such as the Turnbull and Livingston-Cahn models, have been developed to estimate the grain boundary chemical diffusion constant, $s\delta D_g$, for DP coarsening kinetics [131-133]. Here, s represents the segregation factor, δ is the

grain boundary width, and D_g denotes the interface chemical diffusion coefficient of grain boundary. Among these models, the interface migration velocity (v) and the nano-rod spacing (λ) of the precipitates are key kinetic parameters for determining the value of $s\delta D_g$. In this study, the Aaronson-Liu model [134] is employed to determine $s\delta D_g$, which is given by:

$$s\delta D_g = \frac{x_2 - x_0}{4(x_2 - x_1)} v\lambda^2 \tag{5.3}$$

where x_0 is the initial concentration of the solute element in the matrix; x_1 and x_2 are the equilibrium concentrations of the solute element in the matrix and the precipitate at a given temperature, respectively. Owing to the linear relationship between the width of DP nano-rod structures and aging time at the initial stage, the interface migration velocity at different temperatures can be determined. Accordingly, the calculated values of $s\delta D_g$ are 1.64×10^{-29}, 1.22×10^{-28}, 6.56×10^{-28}, and 6.17×10^{-27} m^3/s at 500, 600, 700, and 800 °C, respectively, indicating that coarsening becomes more pronounced with increasing temperature. The activation energy of DP coarsening can be denoted by the Arrhenius equation $s\delta D_g = (s\delta D_g)_0 \exp(-Q/RT)$, where $(s\delta D_g)_0$ is the pre-exponential factor, Q is the activation energy for coarsening, R is the gas constant, and T is the absolute temperature. The activation energy Q can be estimated from the slope of the Arrhenius plot of $ln(s\delta D_g\ T)$ versus $1/T$. As shown in Fig. 5.9, the activation energy for DP coarsening is determined to be Q_p=106 KJ/mol. This value is significantly lower than those reported for HEAs and superalloys strengthened via CP [135]. The lower activation energy can be mainly attributed to the preferential growth of DP-formed precipitates along grain boundaries, where diffusion is significantly faster compared to the long-range bulk diffusion required for the CP process. As

discussed above, the evolution of grain boundaries during aging further facilitates the DP process, resulting in more easily activated and faster coarsening of DP precipitates.

Given the critical coupling between DP and recrystallization in the $L1_2$-nanorod strengthened $(CoCr_{0.5}FeNi_{1.5})_{87.5}Al_{7.5}Ti_5$ alloy, we further investigate the kinetics of dynamic recrystallization in this system. Generally, the Johnson–Mehl–Avrami–Kolmogorov (JMAK) model is employed to quantitatively understand the kinetics of dynamic recrystallization of the studied HEAs [136]:

$$X_v = 1 - \exp(-Bt^n) \tag{5.4}$$

where X_v represents the fraction of recrystallized regions, t is the aging time, n is the Avrami exponent related to the nucleation and growth mode of recrystallization, and B is a constant. The kinetics of recrystallization can be derived from the slope of the ln t versus ln (ln $(1/(1-X_v))$) plot, and the calculated n values are 0.79, 0.43, 0.27, and 0.15 at 500, 600, 700, and 800 °C, respectively (Fig. 5.10a). Based on the fitted n and B values, the relationship between t and X_v can be constructed. As shown in Fig. 5.10b, the aging temperature has a significant effect on the recrystallization kinetics. At all temperatures, an S-shaped curve is observed, where, after an incubation period, the recrystallization rate increases gradually, reaches its maximum at around 50% recrystallized fraction, and then decreases, eventually stopping when nearly complete recrystallization is achieved. Notably, at 800 °C, the alloy reaches approximately 50% recrystallization in as short as 4 seconds, demonstrating extremely high recrystallization efficiency. Furthermore, the activation energy for recrystallization was analyzed using the Arrhenius equation $1/t_{50} = A\exp(-Q_r / RT)$, where t_{50} is the time required to reach a specific recrystallized fraction (typically 50%), T is the aging temperature, A is the pre-exponential factor, and Q_r is the activation energy for recrystallization. According to the slope of the curve in Fig. 5.10c, the activation energy for recrystallization of the

$(CoCr_{0.5}FeNi_{1.5})_{87.5}Al_{7.5}Ti_5$ alloy is calculated to be 247 kJ/mol, which is significantly lower than that of conventional NiCoCrFeAl HEAs (>500 kJ/mol) [137, 138]. The significantly lower recrystallization activation energy can be analyzed through the unique microstructural role of DP. Typically, recrystallization in deformed materials is driven by elastic stored energy, which physically propels the motion of grain boundaries, resulting in the formation and growth of new grains. Notably, in this DP nanorod-strengthened alloy, the driving force for recrystallization arises not only from the conventional, physically driven mechanism but also from DP-induced grain boundary motion. The DP process operates via concentration gradients across grain boundaries, which chemically drive their movement. Therefore, recrystallization in the DP nanorod-strengthened alloy is governed by both physically and chemically driven grain boundary motion. As a result, recrystallization can be activated at lower energies, allowing the process to occur at relatively lower temperatures than those achievable in conventional alloys.

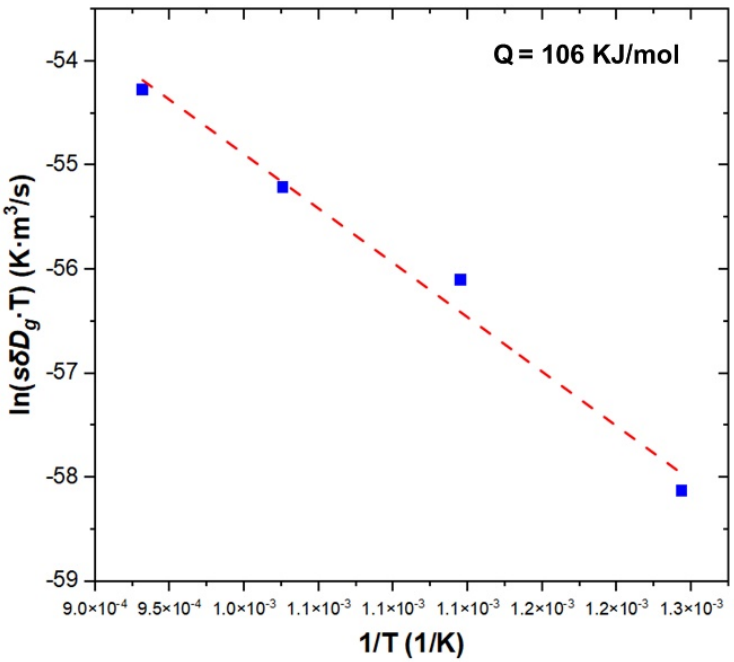

Fig. 5.9. Arrhenius plot of the grain boundary diffusion constant [$ln(s\delta D_g T)$] versus the reciprocal aging temperature ($1/T$), used to determine the activation energy (Q).

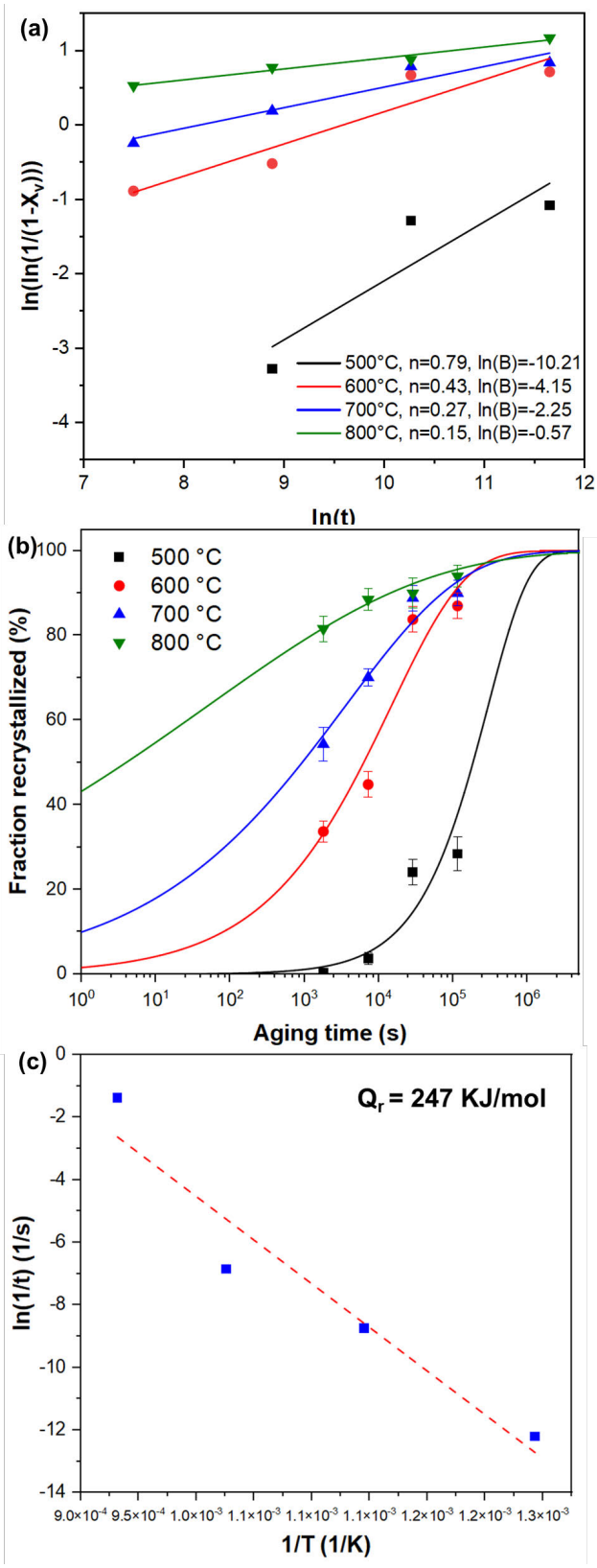

Fig. 5.10. Recrystallization kinetics of the alloy under different heat-treatment conditions: (a) JMAK plot; (b) Recrystallized fraction versus aging time plot; (c) Arrhenius plot for determining the recrystallization activation energy (Q_r).

5.3.3. Strengthening mechanism

To clarify the origins of the alloy's exceptional mechanical performance at 600 °C, we systematically analyze the quantitative relationship between microstructural characteristics and mechanical behavior at this temperature. Numerous studies have demonstrated that the combined evolution of microstructural parameters—such as grain size, dislocation density, and precipitate morphology—plays a pivotal role in determining the yield strength of the alloy. Accordingly, the yield strength (σ_y) of the alloy can be described by:

$$\sigma_y = \sigma_0 + \Delta\sigma_s + \Delta\sigma_g + \Delta\sigma_d + \Delta\sigma_p \quad (5.5)$$

where σ_0 is the friction stress of the alloy, and σ_s, σ_g, σ_d, and σ_p represent the contributions from solid solution strengthening, grain boundary strengthening, dislocation strengthening, and precipitation strengthening, respectively. Among these, grain refinement, dislocation density, and precipitates play dominant roles in determining the yield strength, and their contributions are highly sensitive to heat-treatment conditions. Therefore, the following analysis primarily focuses on these key strengthening mechanisms.

Grain boundaries act as strong barriers to dislocation motion, and the ultrafine-grained structure greatly enhances the yield strength of the alloy. According to the classic Hall–Petch relationship, the strength increment from grain boundary strengthening can be expressed by:

$$\Delta\sigma_g = k_{hp}(d^{-0.5}) \quad (5.6)$$

where k_{hp} = ~516 MPa·μm$^{0.5}$ is the Hall–Petch coefficient, derived from a similar CoCrFeNiAlTi alloy system [21], and d represents the average grain size. After aging at 600 °C for 0.5, 2, 8, and 32 h, the average grain sizes are 210, 300, 380, and 670 nm,

respectively, corresponding to grain boundary strengthening contributions of 1120, 940, 840, and 620 MPa, respectively.

During plastic deformation, mobile dislocations interact and impede the motion of each other. The resulting dislocation strengthening can be estimated using the Bailey–Hirsch equation [139]:

$$\Delta\sigma_d = M\alpha Gb\rho^{0.5} \tag{5.7}$$

where M = 3.06 is the Taylor factor [140], α = 0.2 is a constant for FCC structures, b = 0.25 nm is the Burgers vector for FCC structures [22], G = 81 GPa is the shear modulus of the matrix [103], and ρ represents the dislocation density.

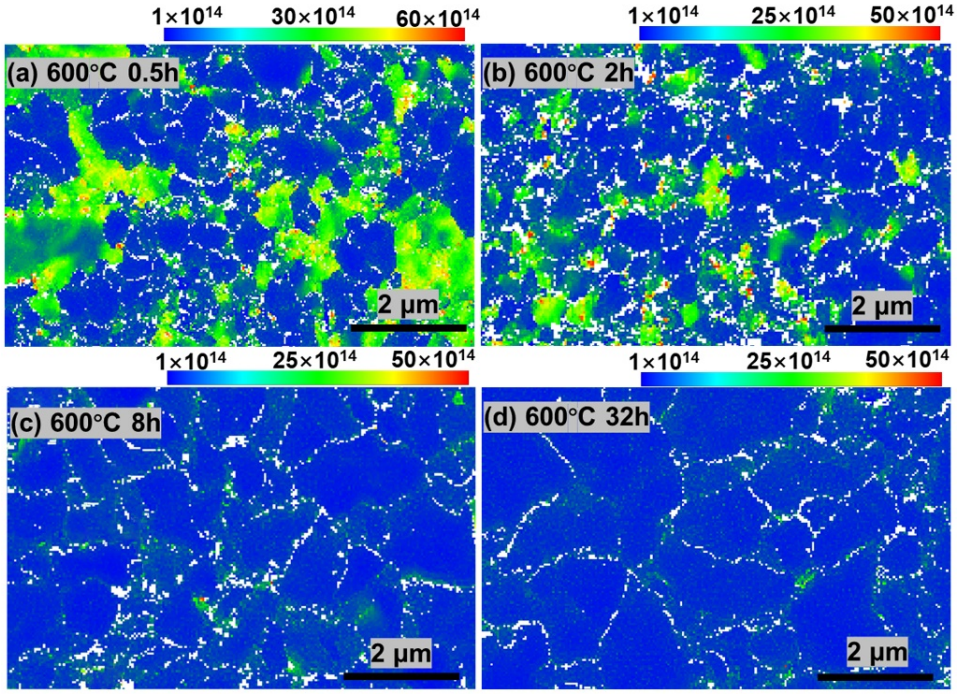

Fig. 5.11. GND density distribution maps of the samples aged at 600 °C for (a) 0.5 h, (b) 2 h, (c) 8 h, and (d) 32 h.

Figure 5.11 summarizes the geometrically necessary dislocation (GND) density distributions of all samples aged at 600 °C. Based on EBSD measurements, the average GND densities after aging at 600 °C for 0.5, 2, 8, and 32 h were estimated to be 1.1 × 10^{15}, 6.9 × 10^{14}, 4.8 × 10^{14}, and 9.1 × 10^{13} m^{-2}, respectively. Consequently, the

contributions from dislocation strengthening at these conditions were estimated to be 400, 331, 277, and 120 MPa, respectively.

In this study, the coherent $L1_2$ nanorod precipitates strengthen the alloy through the shearing mechanism. Order strengthening, which occurs during shearing, is widely recognized as the principal mechanism contributing to precipitation strengthening in such systems [100]. The equation for order strengthening is given by:

$$\Delta\sigma_p = M \cdot 0.81 \frac{\gamma_{APB}}{2b} \left(\frac{3\pi f}{8}\right)^{0.5} \tag{5.8}$$

where γ_{APB} = 0.13 J/m^{-2} is the average value of anti-phase boundary energy of the $L1_2$ phases [120], f is the volume fraction of $L1_2$ precipitates (21%, 34%, 55%, and 58% for the 0.5-h, 2-h, 8-h, and 32-h samples, respectively), as determined from the SANS results. Kelly [141] demonstrated that rod-like precipitates, due to the increased area of intersection with slip planes, can provide up to 1.75 times greater strengthening than spherical particles at the same volume fraction. Based on Kelly's model, the estimated precipitation strengthening contributions from the nanorod precipitates in this study are 559, 711, 903, and 928 MPa, respectively.

Figure 5.12 summarizes the calculated contributions of the main strengthening mechanisms discussed above and compares them with the experimental yield strengths (σ_e) obtained under the corresponding heat-treatment conditions. For the 0.5-h aged sample, the calculated yield strength (2080 MPa) exceeds the experimental value (1820 MPa), likely due to extremely poor ductility of the sample, causing fracture before reaching the yield point. This suggests that while ultrafine grain size and excessively high dislocation density can significantly increase yield strength, they inevitably compromise ductility. High densities of grain boundaries and dislocations enhance strength by impeding dislocation motion, but they also serve as sites for crack formation

and extension, limiting the ability of the alloy to sustain plastic deformation. For the 2-h and 8-h aged samples, the calculated yield strengths are in good agreement with the experimental values, with the 8-h aged sample exhibiting a slightly higher yield strength than the 2-h aged sample. This further demonstrates that optimal mechanical properties are achieved only when grain size, dislocation density, and precipitate microstructure are carefully tailored and optimized. In contrast, the yield strength of the 32-h aged sample decreases significantly, consistent with our predictions. Therefore, these results provide valuable insights into the relationship between the microstructure and mechanical properties of coherent $L1_2$ nanorod-strengthened alloy. The findings emphasize the importance of precisely tailoring microstructural parameters to achieve a desirable combination of strength and ductility in such materials.

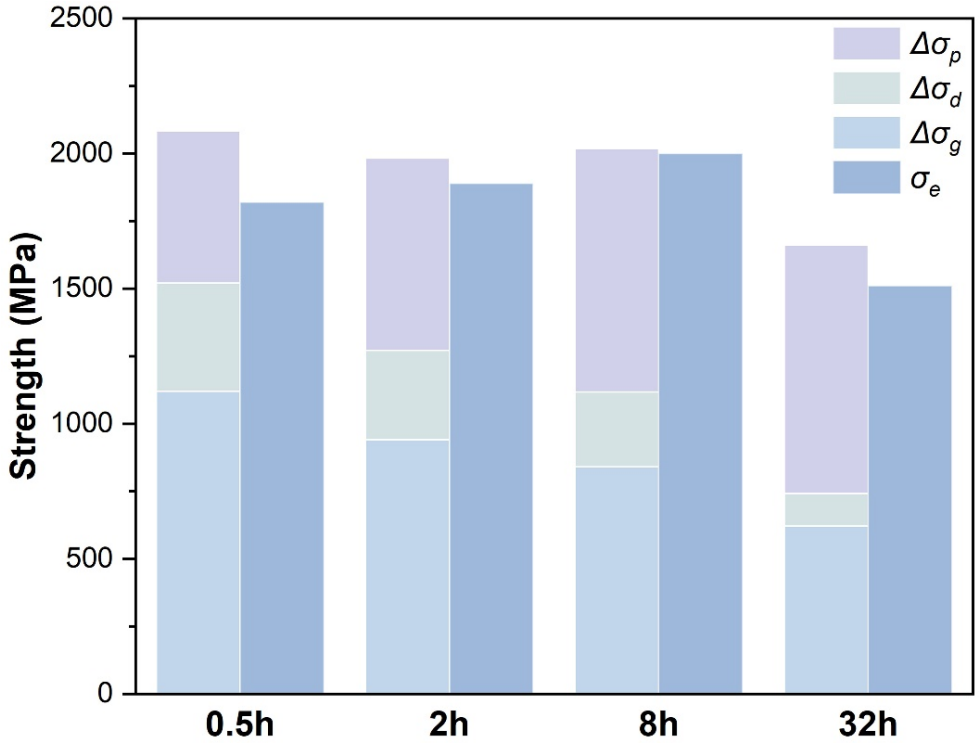

Fig. 5.12. Comparison of the contributions from grain boundary strengthening ($\Delta\sigma_g$), dislocation strengthening ($\Delta\sigma_d$), and precipitation strengthening ($\Delta\sigma_p$) to the yield strength under various aging conditions at 600 °C, along with the corresponding experimental yield strength values (σ_e).

5.4 Conclusions

In this chapter, the mechanisms of microstructural evolution and their effects on mechanical properties of the ultrafine-grained, coherent $L1_2$ nanorod-strengthened $(CoCr_{0.5}FeNi_{1.5})_{87.5}Al_{7.5}Ti_5$ alloy were systematically investigated. The main conclusions are as follows:

1. In the $(CoCr_{0.5}FeNi_{1.5})_{87.5}Al_{7.5}Ti_5$ alloy, the formation and evolution of coherent nanorod $L1_2$ precipitates are governed by a dynamic interplay between DP and recrystallization. At lower aging temperatures, DP preferentially initiates and propagates along grain boundaries, resulting in a fine and stable nanorod microstructure. Increasing aging temperatures significantly accelerate the kinetics of both recrystallization and DP, enabling rapid formation of nanorod precipitates and resulting in a fully recrystallized ultrafine-grained structure.
2. SANS analysis quantitatively reveals that, as the aging time at 600 °C increases from 0.5 to 32 h, both the radius and length of the nanorod precipitates increase significantly (from 12 nm to 21 nm and from 456 nm to 670 nm, respectively), while the volume fraction of precipitates also rises from 21% to 58%, illustrating the pronounced coarsening of the rod-like precipitates.
3. The DP nanorod-strengthened alloy exhibits accelerated kinetics in both precipitation coarsening and recrystallization, owing to the synergistic effects of these two processes. On one hand, recrystallization produces ultrafine grain structures with abundant grain boundaries and physically drives grain boundary motion, thereby promoting the formation and growth of DP

nanorods. On the other hand, the growth of DP nanorods induces grain boundary movement through chemical driving forces, which in turn accelerates grain coarsening. As a result, both recrystallization and DP processes can be activated at lower energies, enabling these transformations to occur at significantly lower temperatures than those required in conventional alloys.

4. The $(CoCr_{0.5}FeNi_{1.5})_{87.5}Al_{7.5}Ti_5$ alloy exhibits outstanding mechanical properties under optimized heat-treatment conditions. Specifically, aging at 600 °C for 8 h achieves an excellent balance between ultrahigh yield strength (exceeding 2 GPa) and total elongation (approaching 20%), demonstrating the effectiveness of the coherent nano-rod strengthening strategy.
5. Quantitative analysis of strengthening mechanisms indicates that grain boundary strengthening and precipitation strengthening are the primary contributors to the enhanced yield strength of the alloy. Achieving an optimal balance among grain size and precipitate microstructure is crucial for realizing superior strength-ductility synergy in $L1_2$ nanorod-strengthened HEAs.

Chapter 6 Synergistic precipitation strengthening via $L1_2$ nanorods and σ nanoparticles in ultrahigh-strength alloys with high work hardening

6.1 Introduction

The concept of introducing intermetallic compounds—including both coherent and incoherent precipitate phases—into HEAs to strengthen their mechanical properties has been widely explored. Through careful alloying design and industrial optimization, the introduction of coherent precipitates into FCC and BCC-based HEAs can lead to the formation of unique coherent nanostructures. These nanoscale, homogeneously distributed coherent precipitates effectively impede dislocation motion, thereby significantly enhancing alloy strength. Moreover, due to the excellent interfacial compatibility and ability to transfer stress with the matrix, they avoid the risk of serving as crack initiation sites, thus allowing the alloy to maintain excellent ductility [86, 142-145].

Among these systems, HEAs strengthened by DP-formed $L1_2$ nanorod precipitates have demonstrated remarkable potential for exhibiting ultrahigh strength. For instance, Gwalani *et al.* developed nano-rod strengthened HEAs, where a high density of uniformly distributed $L1_2$ nano-rods within refined FCC grains increased the alloy strength to above 1.7 GPa [120]. Wang *et al*. also achieved a high density of nano-lamellar $L1_2$ precipitates with a volume fraction of about 50–55% in FCC matrix after 85% cold rolling after aging at 600 °C, resulting in tensile strength up to 1.5 GPa [146]. Li *et al*. introduced a high density of nano-lamellar structures and ultrafine grains into

$CoCrFeNi_2Al_{0.3}Ti_{0.25}$ HEAs, raising the yield strength above 1.9 GPa while retaining about 16% ductility [129]. Our previously published research [21], as well as further exploration in Chapter 5, demonstrated that introducing nano-rod $L1_2$ and ultrafine grains in the $(CoCr_{0.5}FeNi_{1.5})AlTi$ system enabled a yield strength exceeding 2 GPa and 16% uniform elongation at room temperature. This exceptional combination of high strength and good ductility underscores the crucial role of DP-formed nano-rod $L1_2$ structures in achieving a favorable strength–ductility balance in ultra-strong HEAs. However, the mechanical properties of such DP-strengthened alloys commonly exhibit low work-hardening efficiency, which may be attributed to the lack of strong dislocation interactions in HEAs solely strengthened by coherent $L1_2$ precipitates after ultra-high yield strength has been reached.

In recent years, researchers have attempted to further optimize the mechanical performance of HEAs through synergistic precipitation strengthening. The benefit of synergistic precipitation strengthening arises from the incorporation of diverse precipitate types with distinct characteristics, such as the combination of coherent and incoherent phases, or the design of hierarchical precipitation architectures across different scales. The synergistic effects among these precipitates can significantly improve the overall mechanical properties of the alloy [59, 66, 68]. For instance, Niu *et al*. demonstrated that incorporating Nb into Al–Co–Cr–Fe–Ni eutectic HEAs results in the formation of $L1_2$ precipitates within the FCC matrix and facilitates the co-precipitation of α′ and Laves phases in the B2 matrix, leading to a hierarchical heterogeneous microstructure. This combination of strengthening mechanisms yields a notable balance of mechanical properties, with a yield strength of 905 MPa and an elongation of approximately 50% at 700 °C, highlighting the alloy's remarkable resistance to embrittlement at intermediate temperatures. Furthermore, our published

research [67] and Chapter 4 have shown that by tuning the ratio of Al and Nb as well as the heat-treatment conditions in Ni–Co–Fe–Cr–Al–Nb HEAs, it is possible to obtain a composite structure comprising nanoscale spherical coherent $L1_2$ and incoherent micro-scale Laves precipitates. The alloy strengthened by synergistic dual precipitation exhibited a yield strength exceeding 1.4 GPa, a tensile strength up to 1.8 GPa, excellent work-hardening ability, and a uniform elongation of 18%, thus achieving an outstanding strength-ductility balance. In summary, synergistic precipitation strengthening offers a novel strategy for tailoring the mechanical properties of HEAs.

The objective of this chapter is to build upon the ultra-high strength foundation provided by DP nano-rod $L1_2$-strengthened HEAs and further incorporate synergistic precipitation strengthening by introducing additional hard incoherent nano-precipitates, thereby providing extra sources of work hardening and overcoming the limitations of single-mode precipitation strengthening. In transition metal alloys, the incoherent σ phase is generally not regarded as a beneficial phase, as its presence typically leads to severe brittleness of mechanical performance. Wang *et al.* achieved accurate regulation of σ phase precipitation in CoCrV MEA. Their study revealed that a high density of dislocations and stacking faults introduced by cold working significantly promoted the segregation of Cr atoms and triggered the ultrafast precipitation of the σ phase, predominantly in severely deformed regions. Owing to the spatial inhomogeneity of σ phase distribution, spontaneous formation of a heterogeneous lamellar microstructure occurred during subsequent recrystallization, characterized by alternating fine dual-phase (FCC + σ) lamellae and coarse single-phase (FCC) lamellae [147]. This work highlights the crucial role of σ phase in driving the development of lamellar structures. Lu *et al.* systematically investigated the impact of σ phase on the mechanical properties of CoCrFeNiMn HEAs. The precipitation of brittle σ phase particles significantly

increased the ultimate tensile strength of the alloy (>1.2 GPa). More importantly, the presence of σ phase effectively enhanced the work-hardening capability of the alloy, enabling a remarkable uniform elongation of up to 50% [148].

Inspired by these advances, this chapter aims to couple the synergistic precipitation strengthening effect—combining $L1_2$ nano-rod with the σ phase—to achieve an advanced balance of strength, ductility, and work-hardening capacity in DP strengthened HEAs. Specifically, based on the Co–$Cr_{0.5}$–Fe–$Ni_{1.5}$ HEA matrix system developed in Chapter 5, we increased Cr content and introduced alloying elements Al and Ti to design the $(Ni_{1.75}FeCoCr_{0.75})_{86}Al_{10}Ti_4$ alloy (referred to as the 0.75Cr alloy). Through optimized heat treatment condition, we successfully obtained a dense DP-formed $L1_2$ nano-rod structure as well as hierarchical $L1_2$ lamellar architectures tunnel enriched with incoherent σ phase nanoparticles. Various state-of-the-art characterization techniques were employed to investigate the microstructure and strengthening mechanisms of this unique system based on synergistic precipitation strengthening.

6.2 Results

6.2.1. Thermodynamic calculation

Thermo-Calc software with the TTNI8 database was used to evaluate the phase diagram of the 0.75Cr alloy at different temperatures. Figure 6.1 shows the thermodynamic prediction of equilibrium phases, with the equilibrium phase mole fractions plotted as a function of temperature (°C). The results show that there is a wide temperature range where FCC, γ' ($L1_2$), and σ phases exist together. Below 600 °C, the phase constitution of the alloy becomes rather complex and is therefore not further

discussed. Notably, starting from 600 °C, a high fraction of γ' phase and a small fraction of σ phase appear, and both decrease gradually as the temperature increases, eventually leading to a single-phase FCC solid solution at approximately 1050 °C. Therefore, 600 °C was selected as the heat treatment temperature to promote the precipitation of both γ' and σ phases in the alloy. To achieve the DP-formed $L1_2$ nanorod structure, the 0.75Cr alloy was cold-rolled to a 90% reduction in thickness and subsequently aged directly at 600 °C.

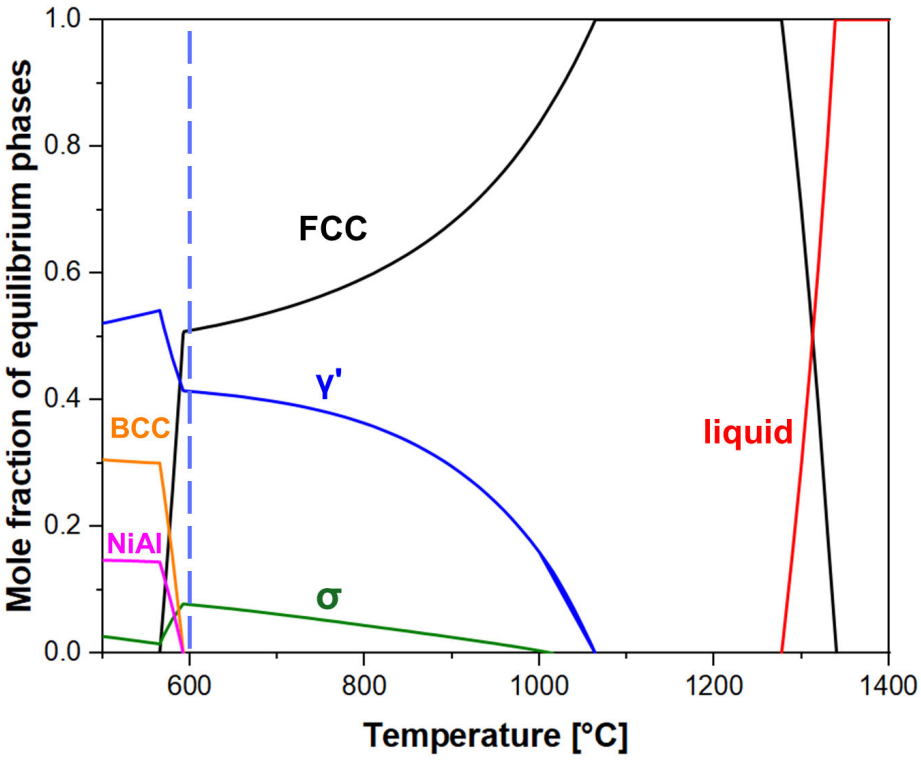

Fig. 6.1. The mole fraction of equilibrium phases as a function of temperature of 0.75Cr alloy.

6.2.2. Mechanical properties

Microhardness testing was employed to determine the optimal aging time for the 0.75Cr alloy. As shown in Fig. 6.2, the as-cold-rolled 0.75Cr alloy (without recrystallization treatment) exhibits high initial hardness due to severe work hardening

and dislocation accumulation. After 0.5 h of aging, the hardness decreases significantly as recrystallization initiates. This softening trend continues until reaching a minimum at 6 h. Subsequently, the microhardness increases progressively with extended aging time, peaking at 24 h. This indicates that 24 h represents the peak-aging condition for maximum age hardening. Room-temperature tensile tests were then conducted to further investigate the mechanical properties of the alloy under this optimized condition.

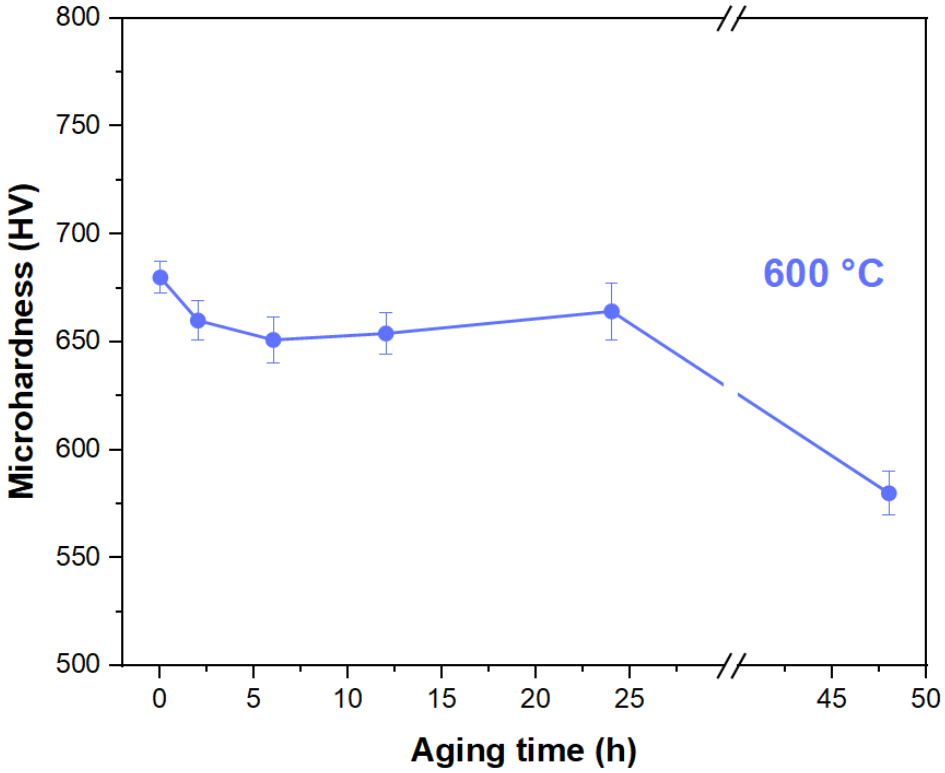

Fig. 6.2. Vickers microhardness of the 0.75Cr alloy as a function of aging time at 600°C.

To highlight the contrast, another alloy with identical composition was prepared using traditional processing (denoted as TPA). Specifically, after 90% cold rolling, the TPA alloy was first subjected to recrystallization at 1150 °C for 3 minutes, followed by aging at 600 °C for 24 hours. The representative engineering stress–strain curves of both the 0.75Cr alloy and TPA under selected conditions are presented in Fig. 6.3. All tensile properties including yield strength (YS), ultimate tensile strength (UTS),

elongation-to-failure (EL), and uniform elongation (UE) of both alloys are summarized in Table 6.1.Prominently, the 0.75Cr alloy achieves ultrahigh yield strength of 2080 ± 12 MPa. Notably, its work-hardening capacity is significantly enhanced compared to that reported by Fan *et al* [21]. After overcoming the initial Lüders banding effect during plastic deformation, sustained work hardening activates progressively, ultimately elevating the ultimate tensile strength to nearly 2300 ± 16 MPa. Although TPA exhibits superior ductility, the 0.75Cr alloy retains a total elongation of approximately 17%, comparable to the similar system described in Chapter 5.

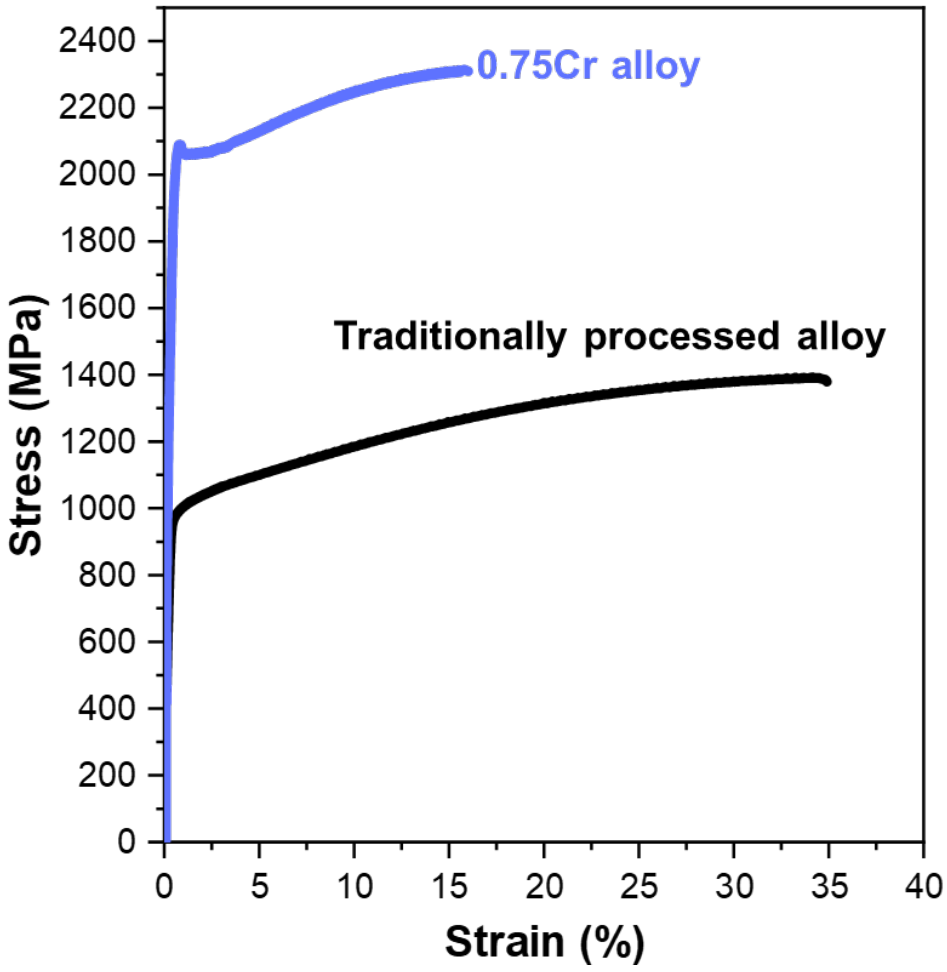

Fig. 6.3. Tensile engineering stress–strain curves of the 0.75Cr and TPA alloy aged at 600 °C for 24 h.

Table 6.1. Yield strengths (YS), ultimate tensile strengths (UTS), elongations-to-failure (EF), and uniform elongations (UE) of the 0.75 Cr and TPA alloys aged at 600 °C for 24 h.

Alloy	YS (MPa)	UTS (MPa)	EL (%)	UE (%)
0.75Cr	2080 ± 12	2300 ± 16	17 ± 3	15 ± 2
TPA	980 ± 11	1400 ± 14	35 ± 4	32 ± 3

Compared with various precipitation-strengthened HEAs in Fig. 5.8, the 0.75Cr alloy maintains an impressive combination of yield strength and ductility. More significantly, when benchmarked against the single $L1_2$ nanorod-strengthened HEA in Fig. 5.7, the 0.75Cr alloy demonstrates superior work-hardening capability. This synergy positions the alloy as a highly promising candidate for advanced structural applications.

6.2.3. Micro/nano-structural Characterization

Figure 6.4 presents the SEM morphology of the 0.75Cr alloy. After aging at 600 °C for 24 h, a nearly fully developed DP structure is achieved. The high-magnification SEM image in Fig. 6.4b confirms dense DP-formed $L1_2$ nanorods with an average radius of ~15 nm. Significantly, distinct precipitate clusters exhibiting irregular ellipsoidal morphology are observed within the DP colonies (highlighted by orange boxes in Fig. 6.4a). Located at the interstices of the DP colonies, these clusters contain high-density hierarchical lamellar networks upon higher magnification (Fig. 6.4b)–a morphology strikingly distinct from the surrounding nano-rod architecture. These elliptical-shaped clusters occupy approximately 9% of the microstructure.

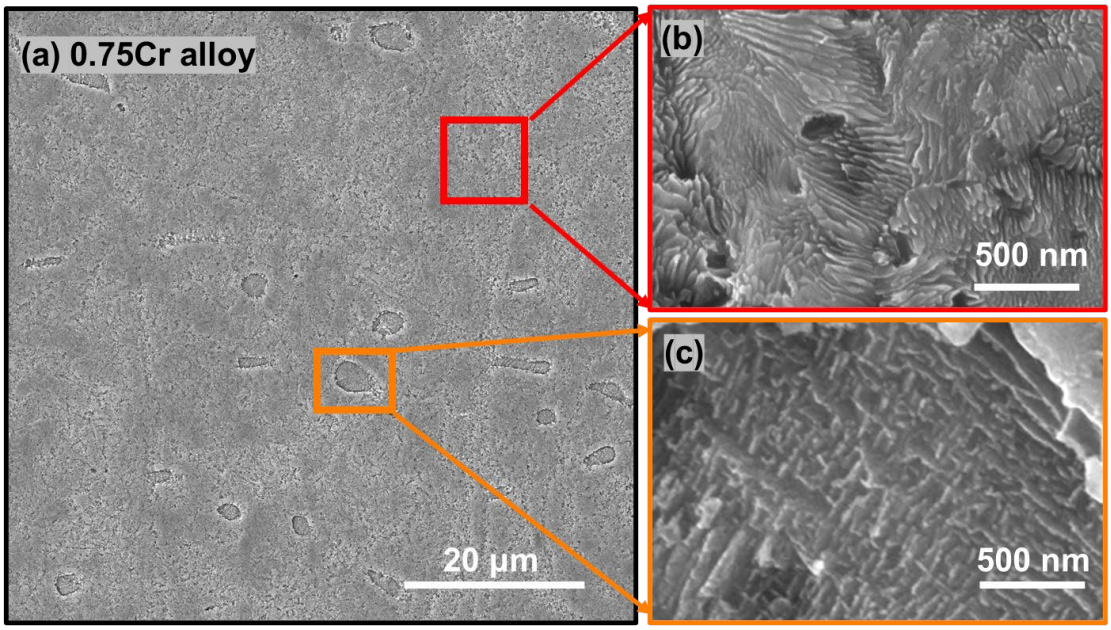

Fig. 6.4. SEM images of the 0.75Cr alloy aged at 600 °C for 24h: (a) Low-magnification overview of the microstructure; (b) High-magnification image showing a region with dense precipitates; (c) High-magnification image showing the elliptical-shaped precipitate clusters.

Figure 6.5a displays a representative XRD pattern of the 0.75Cr alloy. Distinct diffraction peaks at 43° and 51° correspond to the (111) and (200) crystallographic planes of the FCC/$L1_2$ dual-phase matrix. Peak deconvolution analysis of the (311) reflection (Fig. 6.5b) quantifies the lattice misfit between these phases as approximately 0.25%. Notably, two minor peaks at 42° and 46° are indexed to the (410) and (420) planes of the σ phase. These collective XRD signatures confirm a multiphase architecture comprising FCC, $L1_2$, and σ phases.

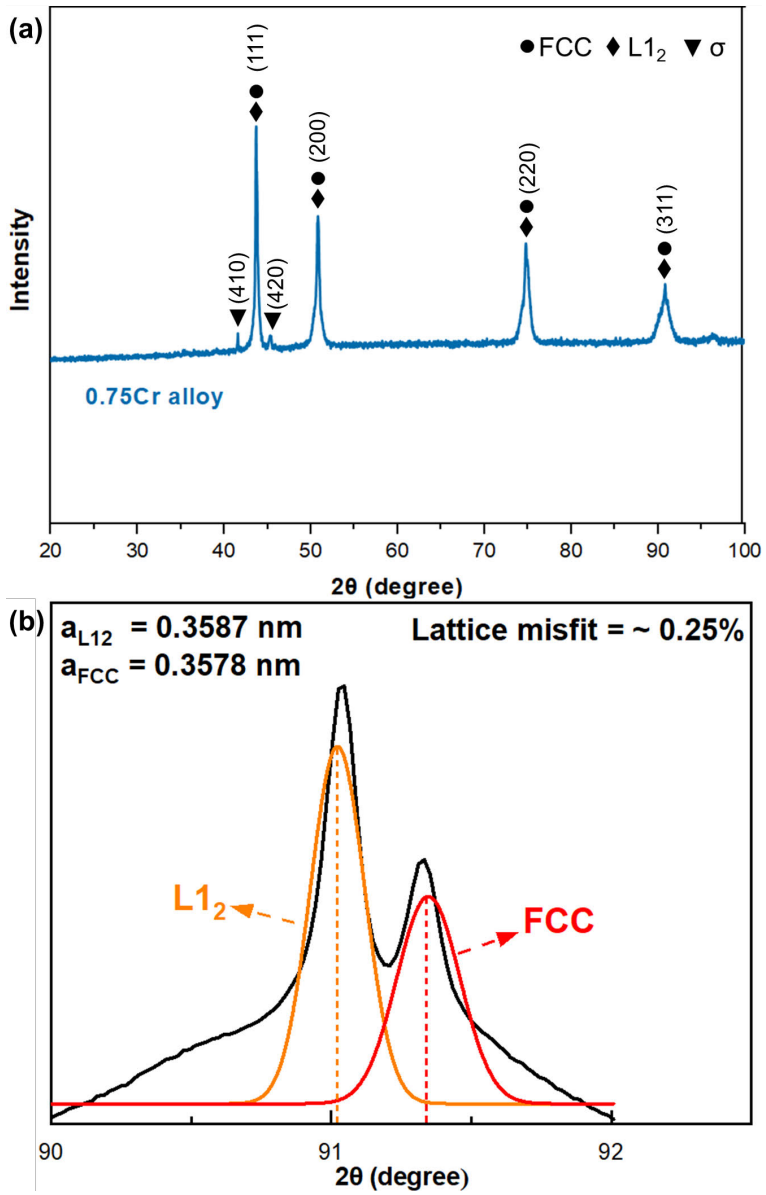

Fig. 6.5. (a) XRD patterns of the 0.75Cr alloy aged at 600 °C for 24h; (b) the deconvolution of the (311) diffraction.

To elucidate the composition of elliptical-shaped clusters, the 0.75Cr alloy was characterized via 3D-APT. Iso-concentration surfaces at 40 at.% Ni and 25 at.% Cr were employed to delineate hierarchical lamellar channels and ultrafine nanoparticles (Figs. 6.6a and c). Proximity histogram profiles of these features are presented in Figs. 6.6b and d, with compositions of precipitates and matrix derived from plateau regions summarized in Table 6.2.

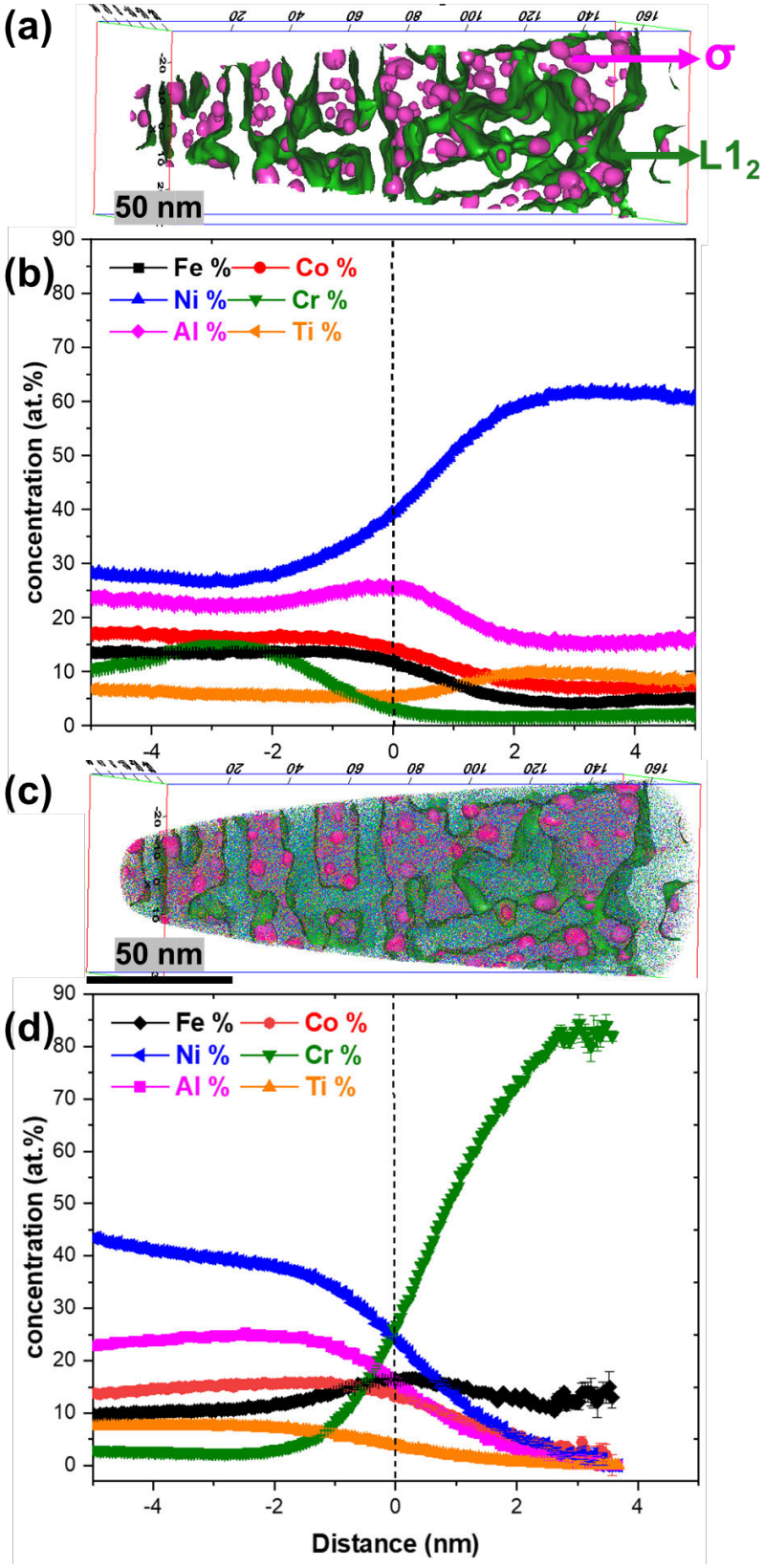

Fig. 6.6. 3D-APT characterization of the 0.75Cr alloy aged at 600 °C for 24 h: (a, c) The enlarged view of elliptical-shaped clusters and atom maps, respectively; (b, d) Proximity histograms of the $L1_2$ and σ phases, respectively.

The clusters exhibit densely packed hierarchical lamellar channels interspersed with ultrafine nanoparticles (Fig. 6.6a). Compositional analysis of lamellar channels (green mark, Fig. 6.6a) reveals: 60.5 ± 0.4 at.% Ni, 9.8 ± 0.2 at.% Co, 16.1 ± 0.1 at.% Al, 7.3 ± 0.2 at.% Ti, 3.8 ± 0.6 at.% Fe, and 2.5 ± 0.3 at.% Cr. The (Ni + Co):(Al + Ti) atomic ratio ≈ 3:1 confirms $(Ni,Co)_3(Al,Ti)$-type $L1_2$ nanostructures. In addition, ultrafine nanoparticles contain 78.3 ± 0.3 at.% Cr, 16.1 ± 0.5 at.% Fe, together with a small amount of Co (2.4 ± 0.2 at.%), Ni (1.8 ± 0.4at.%), Al (1.1 ± 0.1 at.%) and Ti (0.3 ± 0.1 at.%), consistent with Cr-enriched σ-phase. The matrix composition is quantified as 9.9Fe-13.8Co-42.6Ni-2.9Cr-23.2Al-7.6Ti (at.%). The volume fractions of $L1_2$ and σ phases were determined as 40% and 30%, respectively, using the lever rule. Collectively, these results demonstrate a synergistic precipitation architecture dominated by dense DP-$L1_2$ nanorods, complemented by $L1_2$-lamellar clusters enriched with σ-phase nanoparticles.

Table 6.2. Matrix and precipitates compositions (at.%) of the 0.75 Cr alloy aged at 600 °C for 24 h.

	Fe	Co	Ni	Cr	Al	Ti
Matrix	9.9 ± 1.1	13.8 ± 0.8	42.6 ± 0.3	2.9 ± 0.2	23.2 ± 0.1	7.6 ± 0.2
$L1_2$	3.8 ± 0.6	9.8 ± 0.5	60.5 ± 1.0	2.5 ± 0.3	16.1 ± 0.9	7.3 ± 0.4
σ	16.1 ± 0.5	2.4 ± 0.2	1.8 ± 0.4	78.3 ± 0.3	1.1 ± 0.1	0.3 ± 0.1

6.3 Discussion

6.3.1. Formation of synergistic precipitation

Comprehensive microstructural and nanoscale characterization definitively establishes the successful development of a multiphase synergistic precipitation architecture within the 0.75Cr alloy. This sophisticated structure comprises three key constituents: an FCC matrix serving as the continuous phase, a high-density array of $L1_2$ nanorods, and distinctive $L1_2$-based clusters enriched with σ-phase nanoparticles. This unique architecture significantly enhances the alloy's mechanical properties, including both yield strength and work-hardening capability, elevating them to a new level. The evolution of this microstructure is governed by temperature-dependent atomic diffusion kinetics. At the optimized aging temperature of 600°C, significantly enhanced diffusion rates simultaneously accelerate recrystallization and DP processes. Following 24 hours of aging, microstructural analysis confirms two critical achievements: complete recrystallization and full propagation of DP structures saturating the grain interiors. This saturated state manifests as pervasive $L1_2$ nanorod colonies occupying over 90% of the microstructure, as unequivocally demonstrated in Fig. 6.4a. The microstructural evolution arises from dynamically coupled mechanisms between DP and recrystallization. During heat-treatment processing, migrating grain boundaries actively sweep solute atoms, generating localized supersaturation regions adjacent to boundary interfaces. This chemical heterogeneity provides the thermodynamic driving force for preferential nucleation of $L1_2$ precipitates along these mobile boundaries. Simultaneously, steep concentration gradients develop across advancing interfaces, propelling the growth of DP structures perpendicular to the

migration direction. Crucially, the progressive development of DP domains generates additional interfacial energy that accelerates further boundary migration—establishing a self-reinforcing cycle. The robust coupling between DP and recrystallization ultimately leads to the widespread formation and penetration of nanorod-shaped $L1_2$ colonies within the ultrafine-grained FCC matrix, resulting in a highly uniform and refined microstructure after aging at 600 °C for 24 hours.

Focusing on the $L1_2$-based clusters enriched with σ-phase nanoparticles (occupying ~9 vol.%), we observe that DP-generated $L1_2$ lamellae dominate these regions, adopting an interlaced lamellar morphology rather than the typical rod configuration. Crucially, the interlamellar channels serve as diffusion pathways and precipitation sites for ultrafine σ particles (~15 ± 3 nm diameter). These distinctive structures nucleate at grain boundaries and propagate into the FCC/DP-$L1_2$ nanorod matrix. The interlaced $L1_2$ lamellae create confined diffusion channels (Fig. 6.6a, green arrow), where Cr/Fe rejection during $L1_2$ growth elevates local supersaturation (Table 6.2). This, combined with accelerated pipe diffusion along lamellar interfaces, enables σ precipitation at channel intersections. The σ particles further stabilize the lamellar architecture by Zener pinning of $L1_2$ lamellar interfaces, establishing a self-sustaining growth front [149]. These clusters fundamentally transform the work-hardening behavior. While conventional DP-nanorod HEAs exhibit limited strain hardening due to the uniform shearing of coherent precipitates, the introduction of σ-enriched clusters creates heterogeneous deformation barriers, providing additional potential sites for work hardening in the alloy.

Figure. 6.7 presents schematic diagrams of the microstructures of both the TPA alloy and the 0.75Cr alloy. The alloy subjected to conventional heat treatment exhibits large-scale equiaxed grains and spherical $L1_2$ precipitates formed by CP. In contrast,

the 0.75Cr alloy not only possesses an ultrafine-grained structure with a high density of DP nanorods within the grains, but also features grain boundaries decorated with $L1_2$-based clusters enriched with σ-phase nanoparticles. These combined structural characteristics endow the 0.75Cr alloy with superior mechanical properties.

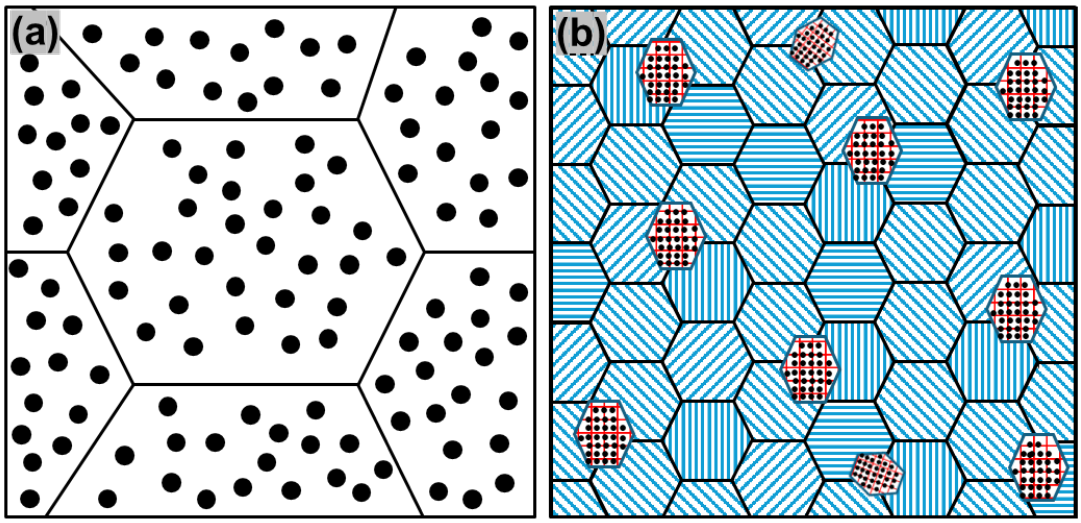

Fig. 6.7. Schematics of the microstructures: (a) TPA alloy; (b) 0.75Cr alloy.

6.3.2. Strengthening mechanisms

A classical strengthening model was utilized to quantitatively evaluate the individual contributions to the yield strength of the 0.75Cr alloy. Typically, the yield strength (σ_y) of an alloy is considered to arise from several sources, including lattice friction stress (σ_0), grain boundary strengthening ($\Delta\sigma_g$), solid solution strengthening ($\Delta\sigma_s$), dislocation strengthening ($\Delta\sigma_d$), and precipitation strengthening ($\Delta\sigma_p$), as described in following equation:

$$\sigma_y = \sigma_0 + \Delta\sigma_s + \Delta\sigma_g + \Delta\sigma_d + \Delta\sigma_p \quad (6.1)$$

where the lattice friction stress (σ_0) was taken to be approximately 156 MPa, based on the previous work by Yoshida *et al*. on CoCrFeNi HEA systems [150]. However, due

to the absence of a clear distinction between solvent and solute atoms in HEAs, it is difficult to directly estimate the solid solution strengthening contribution. To overcome this challenge, we adopted a widely accepted method: the overall composition excluding Ti was treated as the composite solvent, while Ti atoms were considered as the effective solute [22, 96, 97]. This approach enables the application of the conventional solid solution strengthening model, which can be expressed as follows:

$$\Delta\sigma_s = M \cdot \frac{G \cdot \varepsilon_s^{3/2} \cdot c^{1/2}}{700} \tag{6.2}$$

where M = 3.06 is the Taylor factor, G_m is the shear modulus of the matrix (G = 81 GPa), ε_s represents the atomic size mismatch, and c is the atomic fraction of Ti in the FCC matrix, which is 7.6 at.% (Table 6.2). The strength increment introduced by the solid solution strengthening of Nb was calculated to be approximately 49 MPa.

As strong barriers to dislocation glide, grain boundaries critically contribute to the enhanced yield strength of the ultrafine-grained 0.75Cr alloy. This grain refinement strengthening effect is quantitatively described by the classical Hall–Petch relationship:

$$\Delta\sigma_g = k_{hp}(d^{-0.5}) \tag{6.3}$$

where k_{hp} = ~516 MPa·μm$^{0.5}$ is the Hall–Petch coefficient, derived from a similar CoCrFeNiAlTi alloy system [21], and d represents the average grain size. The corresponding grain boundary strengthening effect is calculated to be 660 MPa.

After 24 hours of aging, the 0.75Cr alloy essentially displays a fully recrystallized microstructure, without any partially recrystallized regions. Previous studies by Dasari *et al*. on similar systems and microstructures have suggested that the dislocation density in fully recrystallized alloys can be considered negligible [119]. Consistent with these findings, our results presented in Chapter 5 also indicate that the dislocation density is

very low after prolonged aging. Therefore, a value of 100 MPa is adopted here as a rough estimate for the dislocation strengthening contribution to the overall yield strength.

This study features two distinct intermetallic phases contributing to precipitation strengthening: dense $L1_2$ nanorods and $L1_2$-based clusters enriched with σ-phase nanoparticles. Critically, within the σ-enriched clusters, the $L1_2$ lamellar frameworks maintaining coherent interfaces with the matrix originate from DP—identical to the primary nanorod structures. Consequently, when quantifying precipitation strengthening, the $L1_2$ phase within clusters is not differentiated from the dominant nanorod population. Regarding deformation mechanisms, while non-coherent precipitates typically induce Orowan bypassing, the ultrafine σ particles (~10 nm) in these clusters fall below the critical Orowan size, which enables a precipitate shearing mechanism to operate for both coherent and incoherent precipitates in this system. Order strengthening is widely regarded as the dominant mechanism of precipitation strengthening in such systems, this contribution has been estimated using the following equation [100, 151-153]:

$$\Delta\sigma_p = M \cdot 0.81 \frac{\gamma_{APB}}{2b} \left(\frac{3\pi f}{8}\right)^{0.5} \tag{6.4}$$

where γ_{APB} is the average value of anti-phase boundary energy, b is the Burgers vector for FCC structures [22], and f is the volume fraction of precipitates, which is determined from the APT results. For the $L1_2$ nanorods, previous studies have shown that due to the increased area intersecting with the slip plane, rod-shaped precipitates can provide up to 1.75 times higher strengthening compared to spherical particles at the same volume fraction [120, 141]. Therefore, the strength increment contributed by the $L1_2$ nanorods is approximately 770 MPa (440 MPa × 1.75). Regarding the σ nanoparticles,

data from Table 6.2 indicate that their volume fraction within the characteristic clusters is about 30%, and these clusters account for approximately 9% of the overall microstructure. Thus, the estimated total volume fraction of σ nanoparticles is around 3%, corresponding to a strength contribution of about 173 MPa. Therefore, the total strengthening increment contributed by the various precipitates is approximately 943 MPa.

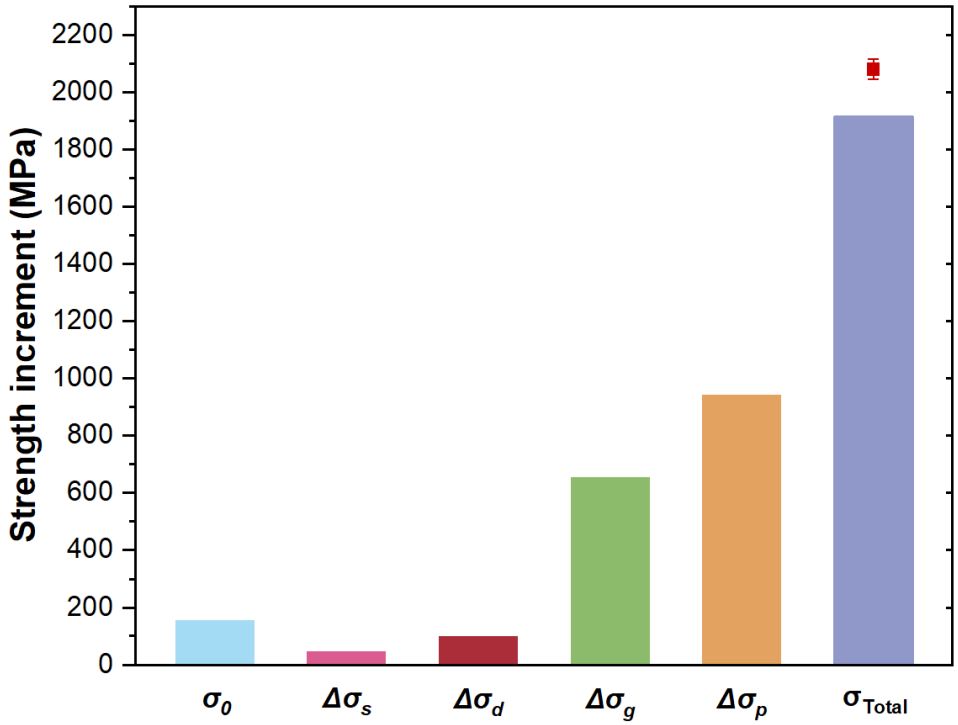

Fig. 6.8. Calculated contributions of solid solution strengthening ($\Delta\sigma_s$), dislocation strengthening ($\Delta\sigma_d$), grain boundary strengthening ($\Delta\sigma_g$), precipitation strengthening ($\Delta\sigma_p$), and total yield strength (σ_{Total}) of the 0.75Cr alloy aged at 600 °C for 24 h. The red dot represents the experimental yield strength.

Figure 6.8 summarizes the results of all the aforementioned strengthening contributions. The calculated theoretical yield strength of the 0.75Cr alloy is approximately 1910 MPa, which is in good agreement with the experimentally measured value of 2080 ± 12 MPa. This consistency demonstrates the validity of the

strengthening mechanism models used in this study. Therefore, by coupling the synergistic precipitation strengthening effect, this alloy achieves a composite precipitate structure that collectively enhances the strength of the DP HEA. As a result, it represents a new type of alloy with significant potential for advanced engineering applications.

6.4 Conclusions

In this chapter, a novel synergistic precipitation strategy coupling DP-formed $L1_2$ nanorods and σ-phase nanoparticles was implemented in the $(Ni_{1.75}FeCoCr_{0.75})_{86}Al_{10}Ti_4$ HEA to overcome the work-hardening limitations of single-phase precipitation strengthening. The key conclusions are as follows:

1. Through 90% cold rolling followed by direct aging at 600°C for 24 h, a dual-phase synergistic structure was achieved, comprising dense DP- $L1_2$ nanorods (40 vol.%) and $L1_2$-based clusters enriched with ultrafine σ nanoparticles (3 vol.%). The σ phase nucleated at $L1_2$ lamellar interfaces via Cr/Fe rejection and pipe diffusion.
2. The 0.75Cr alloy exhibited exceptional yield strength (2080 ± 12 MPa) and ultimate tensile strength (2300 ± 16 MPa), while maintaining 17% total elongation. This represents a 112% increase in yield strength compared to the traditionally processed alloy.
3. The σ-enriched clusters introduced heterogeneous deformation barriers, activating sustained work hardening after yielding. This synergy significantly improved work-hardening efficiency compared to single $L1_2$-nanorod-strengthened HEAs.

4. Precipitation strengthening contributed dominantly (943 MPa), with $L1_2$ nanorods (770 MPa), σ nanoparticles (173 MPa), and Grain boundary refinement (660 MPa) acting synergistically. The calculated yield strength (1910 MPa) aligned closely with experimental data.

Chapter 7 Conclusions and future work

7.1 Conclusions

In this thesis, an in-depth investigation was conducted on the precipitation behavior, microstructural evolution, and mechanical properties of advanced intermetallic-strengthened HEAs. This was achieved through a combination of CALPHAD-guided alloy design, tailored thermomechanical treatments, and comprehensive multi-scale characterization techniques—including XRD, SEM, EBSD, APT, TEM, and SANS. The principal findings are summarized as follows:

1. The development of dual-precipitation strengthened $(Ni_2Co_2FeCr)_{86-x}Al_4Nb_x$ HEAs demonstrated that synergistic precipitation of $L1_2$ nanoparticles and Laves phases effectively overcomes the strength-ductility trade-off. Specifically, the 5Nb alloy achieved an ultrahigh yield strength of 1401 MPa and uniform elongation of 18% through optimized Nb content. Crucially, hierarchical stacking fault networks and Lomer-Cottrell locks activated during deformation provided exceptional work-hardening capability, while quantitative strengthening modeling confirmed precipitation strengthening (dominated by $L1_2$ shearing) contributed ~690 MPa to the yield strength. This work established a paradigm for leveraging complementary precipitate types to achieve balanced properties.
2. This study also elucidated the dynamic interplay between DP and recrystallization in $(CoCr_{0.5}FeNi_{1.5})_{87.5}Al_{7.5}Ti_5$ HEAs. The DP-formed $L1_2$ nanorods nucleate preferentially at migrating grain boundaries, with coarsening kinetics governed by accelerated grain boundary diffusion

(activation energy Q_p = 106 kJ/mol – 40% lower than conventional CP systems). SANS quantification revealed rod dimensions evolved from 12nm × 456nm (0.5 h) to 21 nm× 670 nm (32 h) at 600 °C, while coupled recrystallization kinetics (Q_r = 247 kJ/mol) enabled ultrafine grains (380 nm). The 8h-aged alloy achieved a record yield strength >2000 MPa with 20% elongation, where Hall-Petch strengthening (840 MPa) and order strengthening (903 MPa) synergistically dominated. This highlights DP's dual role as both a precipitation pathway and grain refinement mechanism.

3. A novel σ-nanoparticle enhanced synergistic architecture in $(Ni_{1.75}FeCoCr_{0.75})_{86}Al_{10}Ti_4$ addresses work hardening limitations. Hierarchical microstructures featuring DP- $L1_2$ nanorods (40 vol.%) and σ-enriched $L1_2$ lamellar clusters (3 vol.% σ nanoparticles) are achieved through thermomechanical processing. The σ nanoparticles nucleate via Cr/Fe rejection in $L1_2$ interlamellar channels, delivering unprecedented yield strength (2080 MPa) and tensile strength (2300 MPa) while retaining 17% elongation. Precipitation strengthening contributes 943 MPa to the yield strength, with σ clusters introducing heterogeneous barriers that activate sustained work hardening.

7.2 Suggestions for future work

Although significant progress has been achieved in this thesis, there remain many intriguing directions for future research:

1. Multi-component nanoprecipitate engineering and their impact on comprehensive mechanical properties: The complex characteristics of multi-

component nanoprecipitates—such as elemental distribution, interfacial segregation, and phase transitions during growth and coarsening—pose significant challenges in establishing quantitative relationships between their intrinsic properties and mechanical performance. Currently, a comprehensive understanding and precise control theory for tailoring the microstructure and properties of nanoprecipitate-strengthened high-entropy alloys remain underdeveloped. Therefore, future research should aim to systematically elucidate the fundamental mechanisms governing multi-component nanoprecipitates, enabling fine-tuned microstructural design and optimization of mechanical properties.

2. In-situ deformation mechanisms and dislocation–precipitate interactions: While preliminary ex-situ studies on deformation mechanisms have been conducted in this thesis, a deeper understanding of the dynamic interactions between dislocations and precipitates during plastic deformation is still lacking. Future work should employ advanced in-situ deformation techniques—such as in-situ TEM or synchrotron X-ray diffraction—to directly observe and analyze the real-time evolution of dislocation structures, stacking faults, and precipitate shearing/bypassing behaviors. Such insights are crucial for unraveling the underlying mechanisms of work hardening and damage initiation in ultrahigh-strength HEAs.
3. High-temperature performance, deformation mechanisms, and long-term stability: Although precipitation-strengthened HEAs exhibit outstanding room-temperature properties, their performance under high-temperature conditions—including microstructural stability, deformation mechanisms, and long-term service behavior—remains insufficiently explored. Future studies

should focus on the evolution of nanoscale precipitates (especially DP-formed $L1_2$ rods) and matrix–precipitate interfaces at temperatures above 700 °C, as well as the transition in deformation mechanisms with temperature. These investigations are essential for advancing the application of HEAs in high-temperature structural components such as turbine blades and advanced power systems.

References

[1] Y. Wei, Y. Li, L. Zhu, Y. Liu, X. Lei, G. Wang, Y. Wu, Z. Mi, J. Liu, H. Wang, Evading the strength–ductility trade-off dilemma in steel through gradient hierarchical nanotwins, *Nature communications* 5(1) (2014) 1-8.

[2] R.O. Ritchie, The conflicts between strength and toughness, *Nature materials* 10(11) (2011) 817-822.

[3] B. Gludovatz, A. Hohenwarter, D. Catoor, E.H. Chang, E.P. George, R.O. Ritchie, A fracture-resistant high-entropy alloy for cryogenic applications, *Science* 345(6201) (2014) 1153-1158.

[4] J.W. Yeh, S.K. Chen, S.J. Lin, J.Y. Gan, T.S. Chin, T.T. Shun, C.H. Tsau, S.Y. Chang, Nanostructured high-entropy alloys with multiple principal elements: novel alloy design concepts and outcomes, *Advanced engineering materials* 6(5) (2004) 299-303.

[5] O. Senkov, S. Senkova, C. Woodward, Effect of aluminum on the microstructure and properties of two refractory high-entropy alloys, *Acta Materialia* 68 (2014) 214-228.

[6] O.N. Senkov, G. Wilks, J. Scott, D.B. Miracle, Mechanical properties of Nb25Mo25Ta25W25 and V20Nb20Mo20Ta20W20 refractory high entropy alloys, *Intermetallics* 19(5) (2011) 698-706.

[7] W. Kai, C. Li, F. Cheng, K. Chu, R. Huang, L. Tsay, J. Kai, Air-oxidation of FeCoNiCr-based quinary high-entropy alloys at 700–900 C, *Corrosion Science* 121 (2017) 116-125.

[8] M.-H. Tsai, J.-W. Yeh, High-entropy alloys: a critical review, *Materials Research Letters* 2(3) (2014) 107-123.

[9] R.K. Nutor, Q. Cao, R. Wei, Q. Su, G. Du, X. Wang, F. Li, D. Zhang, J.-Z. Jiang, A dual-phase alloy with ultrahigh strength-ductility synergy over a wide temperature range, *Science advances* 7(34) (2021) eabi4404.

[10] Y. Zhang, T.T. Zuo, Z. Tang, M.C. Gao, K.A. Dahmen, P.K. Liaw, Z.P. Lu, Microstructures and properties of high-entropy alloys, *Progress in materials science* 61 (2014) 1-93.

[11] M.C. Gao, J.-W. Yeh, P.K. Liaw, Y. Zhang, High-entropy alloys.

[12] S. Son, P. Asghari-Rad, A. Zargaran, W. Chen, H.S. Kim, Superlative room temperature and cryogenic tensile properties of nanostructured CoCrFeNi medium-entropy alloy fabricated by powder high-pressure torsion, *Scripta Materialia* 213 (2022) 114631.

[13] X. Wu, D. Mayweg, D. Ponge, Z. Li, Microstructure and deformation behavior of two TWIP/TRIP high entropy alloys upon grain refinement, *Materials Science and Engineering: A* 802 (2021) 140661.

[14] D. Wei, X. Li, W. Heng, Y. Koizumi, F. He, W.-M. Choi, B.-J. Lee, H.S. Kim, H. Kato, A. Chiba, Novel Co-rich high entropy alloys with superior tensile properties, *Materials Research Letters* 7(2) (2019) 82-88.

[15] E.P. George, D. Raabe, R.O. Ritchie, High-entropy alloys, *Nature reviews materials* 4(8) (2019) 515-534.

[16] W. Liu, Z. Lu, J. He, J. Luan, Z. Wang, B. Liu, Y. Liu, M. Chen, C. Liu, Ductile CoCrFeNiMox high entropy alloys strengthened by hard intermetallic phases, *Acta Materialia* 116 (2016) 332-342.

[17] L. Zhang, Y. Zhou, X. Jin, X. Du, B. Li, The microstructure and high-temperature properties of novel nano precipitation-hardened face centered cubic high-entropy superalloys, *Scripta Materialia* 146 (2018) 226-230.

[18] W. Liu, T. Yang, C. Liu, Precipitation hardening in CoCrFeNi-based high entropy alloys, *Materials Chemistry and Physics* 210 (2018) 2-11.

[19] T. Yang, Y. Zhao, Y. Tong, Z. Jiao, J. Wei, J. Cai, X. Han, D. Chen, A. Hu, J. Kai, Multicomponent intermetallic nanoparticles and superb mechanical behaviors of complex alloys, *Science* 362(6417) (2018) 933-937.

[20] Y. Zhao, T. Yang, Y. Tong, J. Wang, J. Luan, Z. Jiao, D. Chen, Y. Yang, A. Hu, C. Liu, Heterogeneous precipitation behavior and stacking-fault-mediated deformation in a CoCrNi-based medium-entropy alloy, *Acta Materialia* 138 (2017) 72-82.

[21] L. Fan, T. Yang, Y. Zhao, J. Luan, G. Zhou, H. Wang, Z. Jiao, C.-T. Liu, Ultrahigh strength and ductility in newly developed materials with coherent nanolamellar architectures, *Nature communications* 11(1) (2020) 1-8.

[22] J. He, H. Wang, H. Huang, X. Xu, M. Chen, Y. Wu, X. Liu, T. Nieh, K. An, Z. Lu, A precipitation-hardened high-entropy alloy with outstanding tensile properties, *Acta Materialia* 102 (2016) 187-196.

[23] M. Perez, M. Dumont, D. Acevedo-Reyes, Implementation of classical nucleation and growth theories for precipitation, *Acta materialia* 56(9) (2008) 2119-2132.

[24] K. Russell, H. Aaronson, Sequences of precipitate nucleation, *Journal of materials science* 10(11) (1975) 1991-1999.

[25] I. Manna, S. Pabi, W. Gust, Discontinuous reactions in solids, *International Materials Reviews* 46(2) (2001) 53-91.

[26] D.B. Williams, E. Butler, Grain boundary discontinuous precipitation reactions, *International Metals Reviews* 26(1) (1981) 153-183.

[27] J. Robson, Modeling competitive continuous and discontinuous precipitation, *Acta Materialia* 61(20) (2013) 7781-7790.

[28] R.E. Hummel, Understanding materials science: history, properties, applications, Springer1998.

[29] B. Cantor, K. Kim, P.J. Warren, Novel multicomponent amorphous alloys, Journal of Metastable and Nanocrystalline Materials, Trans Tech Publ, 2002, pp. 27-32.

[30] Y. Jien-Wei, Recent progress in high entropy alloys, *Ann. Chim. Sci. Mat* 31(6) (2006) 633-648.

[31] B. Cantor, I. Chang, P. Knight, A. Vincent, Microstructural development in equiatomic multicomponent alloys, *Materials Science and Engineering: A* 375 (2004) 213-218.

[32] B. Cantor, Multicomponent and high entropy alloys, *entropy* 16(9) (2014) 4749-4768.

[33] H. Bhadeshia, High entropy alloys, Taylor & Francis, 2015, pp. 1139-1141.

[34] S. Guo, Phase selection rules for cast high entropy alloys: an overview, *Materials Science and Technology* 31(10) (2015) 1223-1230.

[35] R. Kozak, A. Sologubenko, W. Steurer, Single-phase high-entropy alloys–an overview, *Zeitschrift für Kristallographie-Crystalline Materials* 230(1) (2015) 55-68.

[36] J.-W. Yeh, Alloy design strategies and future trends in high-entropy alloys, *Jom* 65 (2013) 1759-1771.

[37] Z. Lu, H. Wang, M. Chen, I. Baker, J. Yeh, C. Liu, T. Nieh, An assessment on the future development of high-entropy alloys: Summary from a recent workshop, *Intermetallics* 66 (2015) 67-76.

[38] Y. Ye, Q. Wang, J. Lu, C. Liu, Y. Yang, High-entropy alloy: challenges and prospects, *Materials Today* 19(6) (2016) 349-362.

[39] J.E. Saal, S. Kirklin, M. Aykol, B. Meredig, C. Wolverton, Materials design and discovery with high-throughput density functional theory: the open quantum materials database (OQMD), *Jom* 65(11) (2013) 1501-1509.

[40] D.B. Miracle, J.D. Miller, O.N. Senkov, C. Woodward, M.D. Uchic, J. Tiley, Exploration and development of high entropy alloys for structural applications, *Entropy* 16(1) (2014) 494-525.

[41] X. Yang, Y. Zhang, Prediction of high-entropy stabilized solid-solution in multi-component alloys, *Materials Chemistry and Physics* 132(2-3) (2012) 233-238.

[42] Y. Zhang, Y.J. Zhou, J.P. Lin, G.L. Chen, P.K. Liaw, Solid-solution phase formation rules for multi-component alloys, *Advanced engineering materials* 10(6) (2008) 534-538.

[43] M. Lucas, G. Wilks, L. Mauger, J.A. Munoz, O.N. Senkov, E. Michel, J. Horwath, S. Semiatin, M.B. Stone, D.L. Abernathy, Absence of long-range chemical ordering in equimolar FeCoCrNi, *Applied Physics Letters* 100(25) (2012) 251907.

[44] C.-J. Tong, Y.-L. Chen, J.-W. Yeh, S.-J. Lin, S.-K. Chen, T.-T. Shun, C.-H. Tsau, S.-Y. Chang, Microstructure characterization of Al x CoCrCuFeNi high-entropy alloy system with multiprincipal elements, *Metallurgical and Materials Transactions A* 36(4) (2005) 881-893.

[45] J.-W. Yeh, S.-Y. Chang, Y.-D. Hong, S.-K. Chen, S.-J. Lin, Anomalous decrease in X-ray diffraction intensities of Cu–Ni–Al–Co–Cr–Fe–Si alloy systems with multi-principal elements, *Materials chemistry and physics* 103(1) (2007) 41-46.

[46] L.R. Owen, N.G. Jones, Lattice distortions in high-entropy alloys, *Journal of Materials Research* 33(19) (2018) 2954-2969.

[47] D. Miracle, G. Wilks, A. Dahlman, J. Dahlman, The strength of chemical bonds in solids and liquids, *Acta materialia* 59(20) (2011) 7840-7854.

[48] Q. Guo, O.J. Kleppa, The standard enthalpies of formation of the compounds of early transition metals with late transition metals and with noble metals as determined by Kleppa and co-workers at the University of Chicago—A review, *Journal of alloys and compounds* 321(2) (2001) 169-182.

[49] K.-Y. Tsai, M.-H. Tsai, J.-W. Yeh, Sluggish diffusion in Co–Cr–Fe–Mn–Ni high-entropy alloys, *Acta Materialia* 61(13) (2013) 4887-4897.

[50] R. Hultgren, P.D. Desai, D.T. Hawkins, M. Gleiser, K.K. Kelley, Selected values of the thermodynamic properties of binary alloys, National Standard Reference Data System, 1973.

[51] B. Cao, C. Wang, T. Yang, C. Liu, Cocktail effects in understanding the stability and properties of face-centered-cubic high-entropy alloys at ambient and cryogenic temperatures, *Scripta materialia* 187 (2020) 250-255.

[52] F.R. De Boer, W. Mattens, R. Boom, A. Miedema, A. Niessen, Cohesion in metals. Transition metal alloys, (1988).

[53] Z. Wu, H. Bei, F. Otto, G.M. Pharr, E.P. George, Recovery, recrystallization, grain growth and phase stability of a family of FCC-structured multi-component equiatomic solid solution alloys, *Intermetallics* 46 (2014) 131-140.

[54] Z. Jiao, J. Luan, M. Miller, Y. Chung, C. Liu, Co-precipitation of nanoscale particles in steels with ultra-high strength for a new era, *Materials Today* 20(3) (2017) 142-154.

[55] K. Ming, X. Bi, J. Wang, Precipitation strengthening of ductile Cr15Fe20Co35Ni20Mo10 alloys, *Scripta Materialia* 137 (2017) 88-93.

[56] H. Daoud, A. Manzoni, N. Wanderka, U. Glatzel, High-temperature tensile strength of Al10Co25Cr8Fe15Ni36Ti6 compositionally complex alloy (high-entropy alloy), *Jom* 67(10) (2015) 2271-2277.

[57] S. Antonov, M. Detrois, S. Tin, Design of novel precipitate-strengthened Al-Co-Cr-Fe-Nb-Ni high-entropy superalloys, *Metallurgical and Materials Transactions A* 49 (2018) 305-320.

[58] H. Daoud, A. Manzoni, N. Wanderka, U. Glatzel, High-temperature tensile strength of Al 10 Co 25 Cr 8 Fe 15 Ni 36 Ti 6 compositionally complex alloy (high-entropy alloy), *Jom* 67 (2015) 2271-2277.

[59] F. He, Z. Wang, P. Cheng, Q. Wang, J. Li, Y. Dang, J. Wang, C. Liu, Designing eutectic high entropy alloys of CoCrFeNiNbx, *Journal of Alloys and Compounds* 656 (2016) 284-289.

[60] T.-T. Shun, L.-Y. Chang, M.-H. Shiu, Age-hardening of the CoCrFeNiMo0. 85 high-entropy alloy, *Materials Characterization* 81 (2013) 92-96.

[61] W. Liu, J. He, H. Huang, H. Wang, Z. Lu, C. Liu, Effects of Nb additions on the microstructure and mechanical property of CoCrFeNi high-entropy alloys, *Intermetallics* 60 (2015) 1-8.

[62] Z. Li, K.G. Pradeep, Y. Deng, D. Raabe, C.C. Tasan, Metastable high-entropy dual-phase alloys overcome the strength–ductility trade-off, *Nature* 534(7606) (2016) 227-230.

[63] T.-T. Shun, C.-H. Hung, C.-F. Lee, The effects of secondary elemental Mo or Ti addition in Al0. 3CoCrFeNi high-entropy alloy on age hardening at 700 C, *Journal of Alloys and Compounds* 495(1) (2010) 55-58.

[64] R. Hultgren, Selected values of thermodynamic properties of metals and alloys, Wiley1963.

[65] J. He, H. Wang, Y. Wu, X. Liu, H. Mao, T. Nieh, Z. Lu, Precipitation behavior and its effects on tensile properties of FeCoNiCr high-entropy alloys, *Intermetallics* 79 (2016) 41-52.

[66] T. Xiong, S. Zheng, J. Pang, X. Ma, High-strength and high-ductility AlCoCrFeNi2. 1 eutectic high-entropy alloy achieved via precipitation strengthening in a heterogeneous structure, *Scripta Materialia* 186 (2020) 336-340.

[67] J. Guo, B. Zhou, S. Qiu, H. Kong, M. Niu, J. Luan, T. Zhang, H. Wu, Z. Jiao, Achieving ultrahigh strength and ductility in high-entropy alloys via dual precipitation, *Journal of Materials Science & Technology* 166 (2023) 67-77.

[68] W. Li, W. Wang, M. Niu, K. Yang, J. Luan, H. Zhang, Z. Jiao, Unraveling the two-stage precipitation mechanism in a hierarchical-structured fcc/L21 high-entropy alloy: Experiments and analytical modeling, *Acta Materialia* 262 (2024) 119426.

[69] T. Li, T. Liu, S. Zhao, Y. Chen, J. Luan, Z. Jiao, R.O. Ritchie, L. Dai, Ultra-strong tungsten refractory high-entropy alloy via stepwise controllable coherent nanoprecipitations, *Nature communications* 14(1) (2023) 3006.

[70] P. Zięba, Recent developments on discontinuous precipitation, *Archives of Metallurgy and Materials* 62 (2017).

[71] J. Fang, W. Liu, J. Luan, T. Yang, Y. Wu, M. Fu, Z. Jiao, Competition between continuous and discontinuous precipitation in L12-strengthened high-entropy alloys, *Intermetallics* 149 (2022) 107655.

[72] X. Wu, B. Wang, C. Rehm, H. He, M. Naeem, S. Lan, Z. Wu, X.-L. Wang, Ultra-small-angle neutron scattering study on temperature-dependent precipitate evolution in CoCrFeNiMo0. 3 high entropy alloy, *Acta Materialia* 222 (2022) 117446.

[73] G. Bokuchava, Y. Gorshkova, R. Fernandez, G. González-Doncel, G. Bruno, Characterization of precipitation in 2000 series aluminium alloys using neutron diffraction, sans and sem methods, *Romanian Reports in Physics* 71(1) (2019) 1-12.

[74] G. Kresse, J. Furthmüller, Efficient iterative schemes for ab initio total-energy calculations using a plane-wave basis set, *Physical review B* 54(16) (1996) 11169.

[75] G. Kresse, J. Furthmüller, Efficiency of ab-initio total energy calculations for metals and semiconductors using a plane-wave basis set, *Computational materials science* 6(1) (1996) 15-50.

[76] G. Kresse, D. Joubert, From ultrasoft pseudopotentials to the projector augmented-wave method, *Physical review b* 59(3) (1999) 1758.

[77] J.P. Perdew, K. Burke, M. Ernzerhof, Generalized gradient approximation made simple, *Physical review letters* 77(18) (1996) 3865.

[78] P.E. Blöchl, Projector augmented-wave method, *Physical review B* 50(24) (1994) 17953.

[79] L. Fan, T. Yang, J. Luan, Z. Jiao, Control of discontinuous and continuous precipitation of γ′-strengthened high-entropy alloys through nanoscale Nb

segregation and partitioning, *Journal of Alloys and Compounds* 832 (2020) 154903.

[80] L. Yang, D. Liang, Z. Cheng, R. Duan, C. Zhong, J. Luan, Z. Jiao, F. Ren, Simultaneous enhancement of strength and ductility via microband formation and nanotwinning in an L12-strengthened alloy, *Fundamental Research* (2022).

[81] Y.-J. Liang, L. Wang, Y. Wen, B. Cheng, Q. Wu, T. Cao, Q. Xiao, Y. Xue, G. Sha, Y. Wang, High-content ductile coherent nanoprecipitates achieve ultrastrong high-entropy alloys, *Nature communications* 9(1) (2018) 4063.

[82] U. Sunkari, S. Reddy, B. Rathod, D. Kumar, R. Saha, S. Chatterjee, P. Bhattacharjee, Tuning nanostructure using thermo-mechanical processing for enhancing mechanical properties of complex intermetallic containing CoCrFeNi2. 1Nbx high entropy alloys, *Materials Science and Engineering: A* 769 (2020) 138489.

[83] U. Sunkari, S. Reddy, S. Chatterjee, P.P. Bhattacharjee, Effect of prolonged aging on phase evolution and mechanical properties of intermetallic strengthened CoCrFeNi2. 1Nbx high entropy alloys, *Materials Letters* 248 (2019) 119-122.

[84] H. Jiang, L. Jiang, D. Qiao, Y. Lu, T. Wang, Z. Cao, T. Li, Effect of niobium on microstructure and properties of the CoCrFeNbxNi high entropy alloys, *Journal of materials science & technology* 33(7) (2017) 712-717.

[85] G. Qin, Z. Li, R. Chen, H. Zheng, C. Fan, L. Wang, Y. Su, H. Ding, J. Guo, H. Fu, CoCrFeMnNi high-entropy alloys reinforced with Laves phase by adding Nb and Ti elements, *Journal of Materials Research* 34(6) (2019) 1011-1020.

[86] T. Yang, Y. Zhao, J. Luan, B. Han, J. Wei, J. Kai, C. Liu, Nanoparticles-strengthened high-entropy alloys for cryogenic applications showing an exceptional strength-ductility synergy, *Scripta Materialia* 164 (2019) 30-35.

[87] P.M. Mignanelli, N. Jones, E. Pickering, O. Messé, C. Rae, M. Hardy, H. Stone, Gamma-gamma prime-gamma double prime dual-superlattice superalloys, *Scripta Materialia* 136 (2017) 136-140.

[88] F. Stein, A. Leineweber, Laves phases: a review of their functional and structural applications and an improved fundamental understanding of stability and properties, *Journal of Materials Science* 56(9) (2021) 5321-5427.

[89] Y. Zhao, T. Yang, Y. Li, L. Fan, B. Han, Z. Jiao, D. Chen, C. Liu, J. Kai, Superior high-temperature properties and deformation-induced planar faults in a novel L12-strengthened high-entropy alloy, *Acta Materialia* 188 (2020) 517-527.

[90] U. Sunkari, S. Reddy, B. Rathod, S. Kumar, R. Saha, S. Chatterjee, P. Bhattacharjee, Heterogeneous precipitation mediated heterogeneous nanostructure enhances strength-ductility synergy in severely cryo-rolled and annealed CoCrFeNi2. 1Nb0. 2 high entropy alloy, *Scientific reports* 10(1) (2020) 1-9.

[91] C.-W. Tsai, M.-H. Tsai, J.-W. Yeh, C.-C. Yang, Effect of temperature on mechanical properties of Al0. 5CoCrCuFeNi wrought alloy, *Journal of Alloys and Compounds* 490(1-2) (2010) 160-165.

[92] Y. Zhao, T. Yang, J. Zhu, D. Chen, Y. Yang, A. Hu, C. Liu, J.-J. Kai, Development of high-strength Co-free high-entropy alloys hardened by nanosized precipitates, *Scripta Materialia* 148 (2018) 51-55.

[93] Z. Ding, B. Cao, J. Luan, Z. Jiao, Synergistic effects of Al and Ti on the oxidation behaviour and mechanical properties of L12-strengthened FeCoCrNi high-entropy alloys, *Corrosion Science* 184 (2021) 109365.

[94] T. Yang, Y. Zhao, W. Liu, J. Zhu, J. Kai, C. Liu, Ductilizing brittle high-entropy alloys via tailoring valence electron concentrations of precipitates by controlled elemental partitioning, *Materials Research Letters* 6(10) (2018) 600-606.

[95] A. Zaddach, R. Scattergood, C. Koch, Tensile properties of low-stacking fault energy high-entropy alloys, *Materials Science and Engineering: A* 636 (2015) 373-378.

[96] J. He, W. Liu, H. Wang, Y. Wu, X. Liu, T. Nieh, Z. Lu, Effects of Al addition on structural evolution and tensile properties of the FeCoNiCrMn high-entropy alloy system, *Acta Materialia* 62 (2014) 105-113.

[97] C. Schuh, T. Nieh, H. Iwasaki, The effect of solid solution W additions on the mechanical properties of nanocrystalline Ni, *Acta Materialia* 51(2) (2003) 431-443.

[98] W. Liu, Y. Wu, J. He, T. Nieh, Z. Lu, Grain growth and the Hall–Petch relationship in a high-entropy FeCrNiCoMn alloy, *Scripta Materialia* 68(7) (2013) 526-529.

[99] T. Gladman, Precipitation hardening in metals, *Materials science and technology* 15(1) (1999) 30-36.

[100] A.J. Ardell, Precipitation hardening, *Metallurgical Transactions A* 16(12) (1985) 2131-2165.

[101] L. Zhang, Z. Jiang, M. Zhang, J. Fan, D. Liu, P. Yu, G. Li, R. Liu, Effect of solid carburization on the surface microstructure and mechanical properties of the equiatomic CoCrFeNi high-entropy alloy, *Journal of Alloys and Compounds* 769 (2018) 27-36.

[102] C. Booth-Morrison, D.C. Dunand, D.N. Seidman, Coarsening resistance at 400 C of precipitation-strengthened Al–Zr–Sc–Er alloys, *Acta Materialia* 59(18) (2011) 7029-7042.

[103] T. Pollock, A. Argon, Creep resistance of CMSX-3 nickel base superalloy single crystals, *Acta Metallurgica et Materialia* 40(1) (1992) 1-30.

[104] R. Kozar, A. Suzuki, W. Milligan, J. Schirra, M. Savage, T. Pollock, Strengthening mechanisms in polycrystalline multimodal nickel-base superalloys, *Metallurgical and materials transactions A* 40(7) (2009) 1588-1603.

[105] M. Vittori, A. Mignone, On the antiphase boundary energy of Ni3 (Al, Ti) particles, *Materials Science and Engineering* 74(1) (1985) 29-37.

[106] J. Embury, A. Kelly, R. Nicholson, Strengthening methods in crystals, *RB Nicholson and A. Kelly* (1971).

[107] D.N. Seidman, E.A. Marquis, D.C. Dunand, Precipitation strengthening at ambient and elevated temperatures of heat-treatable Al (Sc) alloys, *Acta Materialia* 50(16) (2002) 4021-4035.

[108] B. Xiao, L. Xu, Z. Tang, L. Zhao, H. Jing, Y. Han, H. Li, A physical-based yield strength model for the microstructural degradation of G115 steel during long-term creep, *Materials Science and Engineering: A* 747 (2019) 161-176.

[109] Y. Zhao, T. Nieh, Correlation between lattice distortion and friction stress in Ni-based equiatomic alloys, *Intermetallics* 86 (2017) 45-50.

[110] M.R. Ahmadi, E. Povoden-Karadeniz, K. Öksüz, A. Falahati, E. Kozeschnik, A model for precipitation strengthening in multi-particle systems, *Computational materials science* 91 (2014) 173-186.

[111] D. Qi, B. Fu, K. Du, T. Yao, C. Cui, J. Zhang, H. Ye, Temperature effects on the transition from Lomer-Cottrell locks to deformation twinning in a Ni-Co-based superalloy, *Scripta Materialia* 125 (2016) 24-28.

[112] S. Zhao, G.M. Stocks, Y. Zhang, Stacking fault energies of face-centered cubic concentrated solid solution alloys, *Acta Materialia* 134 (2017) 334-345.

[113] X. Xie, G. Chen, P. McHugh, J. Tien, Including stacking fault energy into the resisting stress model for creep of particle strengthened alloys, *Scripta Metallurgica* 16(5) (1982) 483-488.

[114] G. Laplanche, A. Kostka, O. Horst, G. Eggeler, E. George, Microstructure evolution and critical stress for twinning in the CrMnFeCoNi high-entropy alloy, *Acta Materialia* 118 (2016) 152-163.

[115] X. Sun, S. Lu, R. Xie, X. An, W. Li, T. Zhang, C. Liang, X. Ding, Y. Wang, H. Zhang, Can experiment determine the stacking fault energy of metastable alloys?, *Materials & design* 199 (2021) 109396.

[116] X. Wu, Y. Zhu, Y. Wei, Q. Wei, Strong strain hardening in nanocrystalline nickel, *Physical review letters* 103(20) (2009) 205504.

[117] J. Fang, W. Liu, J. Luan, T. Yang, M. Fu, Z. Jiao, Dual effects of pre-strain on continuous and discontinuous precipitation of L12-strengthened high-entropy alloys, *Journal of Alloys and Compounds* 925 (2022) 166730.

[118] Y. Xie, T. Lu, B. Sun, N. Yao, X. Chen, X. Yang, B. Wan, X.-C. Zhang, S.-T. Tu, Discontinuous precipitation enables an exceptional cryogenic strength-strain hardening synergy in a heterostructured medium entropy alloy, *Acta Materialia* 290 (2025) 120955.

[119] S. Dasari, Y.-J. Chang, A. Jagetia, V. Soni, A. Sharma, B. Gwalani, S. Gorsse, A.-C. Yeh, R. Banerjee, Discontinuous precipitation leading to nano-rod intermetallic precipitates in an Al0. 2Ti0. 3Co1. 5CrFeNi1. 5 high entropy alloy results in an excellent strength-ductility combination, *Materials Science and Engineering: A* 805 (2021) 140551.

[120] B. Gwalani, S. Dasari, A. Sharma, V. Soni, S. Shukla, A. Jagetia, P. Agrawal, R.S. Mishra, R. Banerjee, High density of strong yet deformable intermetallic nanorods leads to an excellent room temperature strength-ductility combination in a high entropy alloy, *Acta Materialia* 219 (2021) 117234.

[121] A. Deschamps, F. De Geuser, On the validity of simple precipitate size measurements by small-angle scattering in metallic systems, *Applied Crystallography* 44(2) (2011) 343-352.

[122] K. Górecki, P. Bała, W. Bednarczyk, J. Kawałko, Cryogenic behaviour of the Al5Ti5Co35Ni35Fe20 multi-principal component alloy, *Materials Science and Engineering: A* 745 (2019) 346-352.

[123] M.A. Hemphill, T. Yuan, G. Wang, J. Yeh, C. Tsai, A. Chuang, P. Liaw, Fatigue behavior of Al0. 5CoCrCuFeNi high entropy alloys, *Acta Materialia* 60(16) (2012) 5723-5734.

[124] Y. Chen, H. Deng, Z. Xie, M. Wang, J. Yang, T. Zhang, Y. Xiong, R. Liu, X. Wang, Q. Fang, Tailoring microstructures and tensile properties of a precipitation-strengthened (FeCoNi) 94Ti6 medium-entropy alloy, *Journal of Alloys and Compounds* 828 (2020) 154457.

[125] X. Huang, L. Huang, H. Peng, Y. Liu, B. Liu, S. Li, Enhancing strength-ductility synergy in a casting non-equiatomic NiCoCr-based high-entropy alloy by Al and Ti combination addition, *Scripta Materialia* 200 (2021) 113898.

[126] L. Wang, L. Wang, S. Zhou, Q. Xiao, Y. Xiao, X. Wang, T. Cao, Y. Ren, Y.-J. Liang, L. Wang, Precipitation and micromechanical behavior of the coherent ordered nanoprecipitation strengthened Al-Cr-Fe-Ni-V high entropy alloy, *Acta Materialia* 216 (2021) 117121.

[127] Z. Wang, W. Zhou, L. Fu, J. Wang, R. Luo, X. Han, B. Chen, X. Wang, Effect of coherent L12 nanoprecipitates on the tensile behavior of a fcc-based high-entropy alloy, *Materials Science and Engineering: A* 696 (2017) 503-510.

[128] B. Gwalani, S. Gorsse, V. Soni, M. Carl, N. Ley, J. Smith, A.V. Ayyagari, Y. Zheng, M. Young, R.S. Mishra, Role of copper on L12 precipitation strengthened fcc based high entropy alloy, *Materialia* 6 (2019) 100282.

[129] A. Li, P. Yu, Y. Gao, M. Dove, G. Li, Ultra-high strength and excellent ductility high entropy alloy induced by nano-lamellar precipitates and ultrafine grain structure, *Materials Science and Engineering: A* 862 (2023) 144286.

[130] D.A. Porter, K.E. Easterling, Phase transformations in metals and alloys (revised reprint), CRC press2009.

[131] D. Turnbull, H. Treaftis, Kinetics of precipitation of tin from lead-tin solid solutions, *Acta Metallurgica* 3(1) (1955) 43-54.

[132] J.W. Cahn, The kinetics of cellular segregation reactions, *Acta Metallurgica* 7(1) (1959) 18-28.

[133] J. Livingston, J. Cahn, Discontinuous coarsening of aligned eutectoids, *Acta Metallurgica* 22(4) (1974) 495-503.

[134] H. Aaronson, Y. Liu, On the Turnbull and the Cahn theories of the cellular reaction, *Scripta Metallurgica* 2(1) (1968) 1-7.

[135] T. Yang, Y. Zhao, L. Fan, J. Wei, J. Luan, W. Liu, C. Wang, Z. Jiao, J. Kai, C. Liu, Control of nanoscale precipitation and elimination of intermediate-temperature embrittlement in multicomponent high-entropy alloys, *Acta Materialia* 189 (2020) 47-59.

[136]F.J. Humphreys, M. Hatherly, Recrystallization and related annealing phenomena, elsevier2012.

[137] M. Annasamy, N. Haghdadi, A. Taylor, P. Hodgson, D. Fabijanic, Static recrystallization and grain growth behaviour of Al0. 3CoCrFeNi high entropy alloy, *Materials Science and Engineering: A* 754 (2019) 282-294.

[138] M. Annasamy, N. Haghdadi, A. Taylor, P. Hodgson, D. Fabijanic, Dynamic recrystallization behaviour of AlxCoCrFeNi high entropy alloys during high-temperature plane strain compression, *Materials Science and Engineering: A* 745 (2019) 90-106.

[139] T.H. Courtney, Mechanical behavior of materials, Waveland Press2005.

[140] M.A. Meyers, K.K. Chawla, Mechanical behavior of materials, Cambridge university press2008.

[141] P. Kelly, The effect of particle shape on dispersion hardening, *Scripta Metallurgica* 6(8) (1972) 647-656.

[142] S. Antonov, M. Detrois, S. Tin, Design of novel precipitate-strengthened Al-Co-Cr-Fe-Nb-Ni high-entropy superalloys, *Metallurgical and Materials Transactions A* 49(1) (2018) 305-320.

[143] Y.-J. Chang, A.-C. Yeh, The formation of cellular precipitate and its effect on the tensile properties of a precipitation strengthened high entropy alloy, *Materials Chemistry and Physics* 210 (2018) 111-119.

[144] D. Jin, Z. Wang, J. Yuan, B. Jiang, F. Yu, J. Li, Q. Wang, High-strength and energetic Al2Ti6Zr2Nb3Ta3 high entropy alloy containing a cuboidal BCC/B2 coherent microstructure, *Journal of Alloys and Compounds* 931 (2023) 167546.

[145] J. Hou, S. Liu, B. Cao, J. Luan, Y. Zhao, Z. Chen, Q. Zhang, X. Liu, C. Liu, J. Kai, Designing nanoparticles-strengthened high-entropy alloys with simultaneously enhanced strength-ductility synergy at both room and elevated temperatures, *Acta Materialia* 238 (2022) 118216.

[146] S. Wang, J. Wang, Y. Sun, Z. Yang, G. Sha, Z. Jiao, H. Chen, Ultrastrong and ductile metastable Fe-rich medium-entropy alloy with high-density nanolamellar L12 precipitates, *Scr. Mater* 247 (2024) 116100.

[147] L. Wang, H.-L. Yan, Y. Zhang, B. Beausir, W. Gan, P. Laurent, N. Siredey-Schwaller, C. Esling, X. Zhao, L. Zuo, Dislocation dissociation assisted formation mechanism of sigma phase and its impact on producing heterogeneous lamellar microstructure in CoCrV medium-entropy alloy, *International Journal of Plasticity* 186 (2025) 104260.

[148] W. Lu, W. Guo, Z. Wang, J. Li, F. An, G. Dehm, D. Raabe, C.H. Liebscher, Z. Li, Advancing strength and counteracting embrittlement by displacive transformation in heterogeneous high-entropy alloys containing sigma phase, *Acta Materialia* 246 (2023) 118717.

[149] G. Hu, L. Zeng, H. Du, Q. Wang, Z. Fan, X. Liu, Combined effects of solute drag and Zener pinning on grain growth of a NiCoCr medium-entropy alloy, *Intermetallics* 136 (2021) 107271.

[150] S. Yoshida, T. Bhattacharjee, Y. Bai, N. Tsuji, Friction stress and Hall-Petch relationship in CoCrNi equi-atomic medium entropy alloy processed by severe plastic deformation and subsequent annealing, *Scripta Materialia* 134 (2017) 33-36.

[151] K. Ma, H. Wen, T. Hu, T.D. Topping, D. Isheim, D.N. Seidman, E.J. Lavernia, J.M. Schoenung, Mechanical behavior and strengthening mechanisms in ultrafine grain precipitation-strengthened aluminum alloy, *Acta Materialia* 62 (2014) 141-155.

[152] Y. Tong, H. Zhang, H. Huang, L. Yang, Y. Hu, X. Liang, M. Hua, J. Zhang, Strengthening mechanism of CoCrNiMox high entropy alloys by high-throughput nanoindentation mapping technique, *Intermetallics* 135 (2021) 107209.

[153] Z. Zhu, Q. Nguyen, F. Ng, X. An, X. Liao, P. Liaw, S. Nai, J. Wei, Hierarchical microstructure and strengthening mechanisms of a CoCrFeNiMn high entropy

alloy additively manufactured by selective laser melting, *Scripta Materialia* 154 (2018) 20-24.